Advances in Single Point Imaging

for Electron Paramagnetic and Magnetic Resonance Imaging

By
Hyungseok Jang

A dissertation submitted in partial fulfillment of

the requirements for the degree of

Doctor of Philosophy

(Electrical and Computer Engineering)

at the

UNIVERSITY OF WISCONSIN-MADISON

2017

Date of final oral examination: 1/11/2017

The dissertation is approved by the following members of the Final Oral Committee:

Alan B. McMillan. Associate Scientist, Radiology
Yu Hen Hu. Professor, Electrical and Computer Engineering
Nader Behdad. Associate Professor, Electrical and Computer Engineering
Oliver Wieben. Associate Professor, Radiology
Walter F. Block. Professor, Medical Physics

Abstract

Electron paramagnetic resonance imaging (EPRI) and magnetic resonance imaging (MRI) are non-invasive imaging modalities based on similar physical phenomenon. MRI provides rich anatomical information based on proton imaging, while EPRI offers unique, quantitative information using spin probes such as tissue oxygenation, acidity, and redox status. In EPR-oximetry due to extremely short EPR signal lifetime (< 1μs) of spin probe (e.g., Oxo-63) and hardware constraints (e.g., gradient slewrate and RF deadtime), common imaging schemes utilized in MRI are generally not applicable. Therefore, specialized imaging schemes must be utilized to allow encoding of the rapidly decaying signal in EPRI. In MRI, single point imaging (SPI) has been developed for imaging object with short T2* in 1985, and has recently been revisited as a hybrid technique to improve the imaging of short T2* species. In EPRI, SPI has shown utility for in vivo characterization of tissue oxygenation.

This thesis explores novel uses of SPI in EPR-oximetry and MRI. In EPR studies, a new method for image acquisition and reconstruction is studied, which enables accurate T2* estimation with high spatio-temporal resolution for oxygen imaging. Moreover, a method utilizing a model-based compressed sensing technique is explored to further accelerate image acquisition (up to 30x). In MR studies, a novel technique to measure a gradient waveform using dynamic SPI is developed, where a gradient impulse response function based on LTI concept is also studied. For improved imaging of short T2* species in MRI, a new imaging scheme using SPI is developed, termed ramped hybrid encoding (RHE), where encoding time is minimized to reduce blurriness in object with short T2*. Two applications based on RHE are studied in depth:

a rapid RHE-based attenuation correction for PET/MR and a highly efficient bi-component T2* estimation in human knee using RHE.

Acknowledgements

I would like to express my sincere gratitude to all those who have made this thesis possible.

First of all, I would like to thank my mentor Dr. Alan McMillan for the immeasurable amount of support and guidance he has provided throughout my research. As a research advisor, he always guided me in right direction whenever I was lost in difficult problems to solve. He always trusted me, being patient when I didn't make progress in my research. He taught me many things about research such as academic writing, presentation, and logical thinking. Owing to this support and advice, I was able to make fruitful academic results in my Ph.D. research. Moreover, he gave me invaluable advices about life in Madison.

I would like to thank Professor Yu Hen Hu, my academic advisor in Electrical and Computer Engineering. Whenever I had any concerns and troubles in the course of my Ph.D. program, the door to his office was always wide open for discussion and consultation. I would like to also thank all my committee members for giving me precious advices and guidance.

I would like to also thank researchers in National Institute of Cancer. Dr. Murali Cherukuri and Dr. Sankaran Subramanian gave me unconditional supports and advices in EPR studies. Nallathamby Devasahayam and Chandramouli Gadisetti helped me on EPR experiments in many ways. Without their passionate participation and help, the EPR studies could not have been conducted successfully.

Many thanks to coworkers and researchers in Radiology in University of Wisconsin Madison for helping me in many studies and giving me insights with their deep knowledges.

Professor Kevin Johnson, Dr. Curtis Wiens, and Dr. Fang Liu helped me a lot in studies about UTE imaging. Professor Diego Hernando and Dr. Samir Sharma helped me with studies related with fat and water separation. Dr. Tyler Bradshaw gave me precious advices in PET/MR studies. Sara John, Jenelle Fuller, and Kelli Hellenbrand helped me in many MR imaging experiments for my study. I would like to also thank Professor Tom Grist and Professor Frank Korosec for supporting me to continue to conduct researches in MRI group.

I would like to thank my family, my wife Sukyeong Bae and my daughter Hanna Jang, for their unconditional love and support. Many thanks to my parents, brother, and friends in Korea.

TABLE OF CONTENTS

List of Figures

List of Tables

Chapter 1. Introduction

Electron paramagnetic resonance imaging (EPRI) and magnetic resonance imaging (MRI) are non-invasive imaging modalities based on similar physical phenomenon: electron paramagnetic resonance (EPR) discovered by Zavoisky in 1945 and nuclear magnetic resonance (NMR) discovered by Bloch and Purcell in 1944. In MRI, proton is commonly imaged for clinical use since water is abundant in human body, which allows high SNR (signal to noise ratio) and rich soft tissue contrast. EPRI images electrons using exogenous spin probes, which offers unique, quantitative information such as tissue oxygenation, acidity, and redox status.

Although the discovery of EPR was only one year later than the discovery of NMR, EPRI is still in primitive stage, while MRI has made noticeable advancement in development of imaging systems with myriads of methodologies to image different body parts and functions (e.g., imaging of anatomy, tissue micro structure, blood flow, oxygenation, and cardiac motion), which has been already commercialized and used for clinical diagnosis. A challenge in EPRI is low SNR due to natural scarcity of unpaired electrons and low external magnetic field strength, B0, (~10mT) due to high gyromagnetic ratio of electron (660 times higher than proton in MRI)[1]. Moreover, high resonance frequency (~300MHz to 1GHz) in EPRI makes it difficult to image a large subject due to limited RF penetration.

In EPRI, paramagnetic species such as transition metal ions (Fe, Cu, Mn, Co, Mo, Ni) or free radicals (typically carbon, nitrogen or oxygen containing compounds) are imaged using an exogenous spin probe since there is insufficient populations of free radicals to measure in natural status. With recent development of a non-toxic spin probe, Oxo-63, EPRI has become capable of

quantitative in vivo oxygen imaging[2], which enables in vivo oncological study of cycling hypoxia. However, due to the extremely short EPR signal lifetime (< 1μs in 10mT) of Oxo-63 and hardware constraints (e.g., gradient slewrate and RF deadtime), common imaging schemes utilized in MRI are generally not applicable. Therefore, specialized imaging schemes must be utilized to allow encoding of the rapidly decaying signal in EPRI.

Imaging tissue with short-decaying signal (i.e., tissue with extremely short T2* decay such as bone and tendon) is also challenging in MRI. Recently, technological advancements of imaging hardware in gradient and RF systems have enabled imaging of short T2* species, called Ultrashort Time Echo (UTE)[3] imaging. Unfortunately, UTE imaging technique that encodes k-space (Fourier transform of an image) from center to out using ramping up gradients is not feasible in EPRI due to limited slewrate in the gradient system (typically < 200mT/m/ms), where long encoding time (100μs~1ms depending on desired resolution) is required to acquire k-space data. Therefore, a constant gradient is used in EPRI, which limits the possible imaging strategy, and hence a simple encoding method using constant gradients such as a spin echo based radial frequency encoding similar with rotating ultra-fast imaging sequence (RUFIS)[4] or single point imaging (SPI) has been used.

In MRI, an early study to image solid objects with extremely short relaxation (or signal decay) was first performed by single point imaging (SPI, pure phase encoding) in 1985[5]. However, in SPI each point in k-space must be individually encoded, making 3D imaging an order of magnitude slower than conventional techniques. Due to the long acquisition time required, SPI is often denounced as an expensive and obsolete technique in MRI. However, in EPRI, SPI has recently shown utility for in vivo characterization of tissue oxygenation[6,7]. In the MR literature, SPI has also recently been revisited as a hybrid technique to improve the imaging

of short T2* species[8].

This thesis explores novel uses of SPI in EPRI and MRI. The major developments are summarized below.

1.1 Development of single acquisition quantitative SPI for EPRI

In SPI, images can be consecutively obtained through phase encoding time delays to estimate the transverse relaxation parameter (T_2*)[9] and thus characterize tissue oxygenation in EPRI oxygen imaging. A new technique using SPI was developed to synthesize k-space in the temporal domain to maintain effective k-space bandwidth and thus reduce the impact of Gibbs ringing artifact, which allows single acquisition measurement of the transverse relaxation parameter to enhance temporal resolution (e.g., at least 3x faster in EPR oxygen imaging). My abstract regarding this method was first introduced in the preceding of International Society for Magnetic Resonance in Medicine (ISMRM) 2013 annual meeting, and the journal paper was published in Magnetic Resonance in Medicine (MRM) [10] in 2013.

1.2 Development of accelerated SPI for EPRI

To further enhance spatio-temporal resolution of EPRI, a new imaging scheme was developed, which benefits from a new sampling pattern, bilateral k-space extrapolation, and model-based compressed sensing reconstruction. In this method, undersampled k-space data are combined through temporal domain, and remaining reconstruction errors are effectively suppressed using compressed sensing techniques based upon principal component coefficient maps[11]. I introduced this method in the MRS & Other oral session in ISMRM 2014 annual meeting, and magna-cum-laude was awarded to this work. The relevant journal paper was

published in MRM[12] in 2015.

1.3 Development of rapid and robust gradient measurement technique using dynamic SPI

Accurate knowledge of the k-space trajectory is critical for artifact-free MR imaging, particularly in non-Cartesian imaging. In this method, a new gradient measurement technique based on single point imaging (SPI) was developed, which allows simple, rapid, and robust measurement of k-space trajectory. In the proposed technique, the zoom-in/out effect of dynamic SPI is utilized for k-space trajectory measurement. First, 1D SPI data are acquired from a targeted gradient in each axis, and then relative FOV scaling factors between encoding times are found, which represents relative k-space position. Improvements in image quality are demonstrated for UTE, spiral, and ramp-sampled bipolar gradient echo imaging. Moreover, a gradient impulse response function (GIRF) that characterizes a gradient system with linear time invariant (LTI) concept was measured in three different MR systems using the proposed method and applied for image reconstructions. I presented this method in Mapping & Manipulating Fields electronic poster session in ISMRM 2016 annual meeting. The relevant journal paper was published in MRM[12] in 2016. A patent application describing this method was filed through WARF on October 12, 2015.

1.4 Development of ramped hybrid encoding for MRI

In hybrid UTE imaging, SPI is used to acquire data in central k-space that are missing during RF transmitter/receiver recovery time (deadtime), while frequency encoding is used to rapidly acquire k-space data in a center-out direction, where gradients are ramped before the RF excitation to allow faster encoding that is crucial in UTE imaging to improve image quality for

short-lived signals. However, this can introduce undesirable phenomena such as slice selectivity, chemical shift artifact, and blurriness of short T_2* species. The proposed Ramped Hybrid Encoding (RHE) resolves these issues and allows improved imaging of short T_2* objects compared to other conventional UTE or ZTE imaging schemes. I introduced this new imaging scheme in Novel Pulse Sequences & Trajectories oral session in ISMRM 2015 annual meeting, and summa-cum-laude was awarded to this work. The relevant journal paper was published in MRM[13] in 2016

1.5 A Novel MR-based attenuation correction for PET/MR using RHE

Recently, ultrashort TE imaging based MR-based attenuation correction (MRAC) has been proposed in literature to overcome the intrinsic difficulty in MRI to resolve bone contrast and hence enable more reliable estimation of attenuation map. However, the long acquisition time required for UTE imaging still remains challenging. In this study, we proposed a novel, rapid dual echo method for UTE based MRAC, which allows segmentation of bone, air, fat, and water with high spatial resolution ($1mm^3$) in a single scan with extremely short scan time (35sec). A manuscript describing this method is currently under preparation.

1.6 Highly efficient bi-component T2* mapping of knee based on RHE

T2* analysis is used in musculoskeletal imaging to characterize tendon, meniscus, and cartilage in human joints. With the development of high performance gradient systems, ultrashort time echo (UTE) imaging has become more feasible, allowing robust bi-component of short and long T2* tissue components. Many studies have been performed to realize robust and clinically feasible bi-component T2* imaging, but the long acquisition time required to obtain multiple echo images remains challenging. In this study, we developed a novel, rapid imaging scheme for

bi-component T2* analysis, based on ramped hybrid encoding (RHE) that allows robust bi-component T2* estimation within a single scan. A manuscript describing this method is currently under preparation.

1.7 Overview of the dissertation

In this dissertation, SPI is explored in the two aspects of different imaging modalities, EPRI and MRI. In **Chapter 2**, the background of EPR and MR imaging are reviewed. In **Chapter 3**, the single point imaging scheme is reviewed. In **Chapter 4**, a single acquisition single point imaging based EPRI method using k-space extrapolation is introduced. In **Chapter 5**, an accelerated single point imaging based EPRI method using bilateral k-space extrapolation and compressed sensing reconstruction based on principal component analysis (PCA) is described. In **Chapter 6**, dynamic SPI based gradient measurement technique is presented. In **Chapter 7**, RHE, a novel UTE imaging scheme for MRI, is explored. In **Chapter 8**, MR-based attenuation correction for PET/MR imaging utilizing RHE is presented. In **Chapter 9**, highly efficient bi-component T2* mapping of the knee based on RHE is described. In **Chapter 10**, the main findings of this dissertation are summarized, and remaining issues for future works are discussed.

Chapter 2. Background

2.1 Physics of EPRI and MRI

2.1.1 Nuclear magnetic resonance / electron paramagnetic resonance

In natural state without external electromagnetic force, an unpaired electron or an unpaired proton has ½ spin that generates a magnetic moment, which creates a small but measurable magnetization as following equation.

$$\mu = \gamma S \tag{2.1}$$

, where μ is magnetic moment, γ is the gyromagnetic ratio, and S is the spin angular momentum. For example, the gyromagnetic ratio ($\gamma/2\pi$) of ^{1}H and electron are 42.58 MHzT^{-1} and -28.02 GHzT^{-1} respectively, where electron has 658x higher gyromagnetic ratio than proton. Other atomic nuclei such as ^{3}He, ^{13}C, ^{15}N, ^{17}O, ^{19}F, ^{31}P, ^{129}Xe also have non-zero spin and thus exhibit magnet resonance phenomenon; however, for clarity we will focus only on electrons and the protons in this thesis.

In absence of an external magnetic field, each individual proton or electron spins about its own axis, generating a magnetic moment. However, net magnetization, a total sum of μ's, becomes zero since the individual magnetization of each nuclei is oriented in random direction. To harness this magnetization, an external magnetic field is applied, where the direction of B_0 field is conventionally considered as the 'z' direction. In presence of this B_0 field, protons or electrons precess (or wobble) about the z-axis in a parallel or anti-parallel direction, resulting in precessing magnetization (Figure 2.1 (a) and Figure 2.1 (b)). The frequency of precession called Larmor frequency is determined by the following equation.

$$\omega_0 = \gamma B_0 \tag{2.2}$$

Note that electrons spin and precesse in opposite direction to protons, as the opposite sign of gyromagnetic ratio implies. Naturally, there are slightly more populations in a parallel (+z) over anti-parallel (-z) direction since spins in anti-parallel direction have higher energy state than spins in parallel direction, resulting in small but effective net magnetization along z-direction. The number of nuclei or electrons in parallel or anti-parallel direction is described by Boltzman distribution as following equation.

$$\frac{N_+}{N_-} = e^{-\frac{\gamma B_0}{kT}} \tag{2.3}$$

, where N_+ and N_- denote the number of spins in anti-parallel and parallel direction respectively, k is Boltzman constant, and T is the temperature in Kelvin. The resultant net magnetization is given by

$$M_0 = \frac{1}{2}\hbar(N_+ - N_-) \cong \frac{\gamma^2 \hbar^2 N_0 B_0}{4kT} \tag{2.4}$$

, where N_0 is total number of spins, and $\hbar$ is Planck constant. M_0 is the net magnetization, also called equilibrium magnetization. Note that the magnetization increases with B_0, implying that the more signal can be obtained with higher magnetic field.

2.1.2 RF excitation and free induction decay

To measure the net magnetization, electromagnetic wave (RF pulse) with resonance frequency ω_0 is applied perpendicular to the z-axis. With the application of this RF wave (Figure 2.1(c)), the magnetization rotates about this additional field, B_1, by absorbing the electromagnetic energy, and flips onto the x-y plane. The frequency of this precession can be

described by the following equation.

$$\omega_1 = \gamma B_1 \tag{2.5}$$

Flip angle, α, is determined by magnitude of the B_1 field and duration of applied RF pulse. For example, with constant B_1 field and a duration of RF pulse τ, a flip angle $\alpha = \tau\omega_1 = \tau\gamma B_1$ is obtained. Given the flip angle α, transverse magnetization in x-y plane is calculated as $M_{xy}(0) = M_0 \sin\alpha$, while the longitudinal magnetization along z-direction is $M_z(0) = M_0 \cos\alpha$.

Once a desired flip angle is achieved, the RF pulse is cut off immediately, and then flipped magnetization returns back to equilibrium magnetization, emitting absorbed energy back in the form of electromagnetic wave, which is called relaxation (Figure 2.1(d)). The relaxation occurs independently in two folds, in z direction and on x-y plane, which are called T_1 and T_2

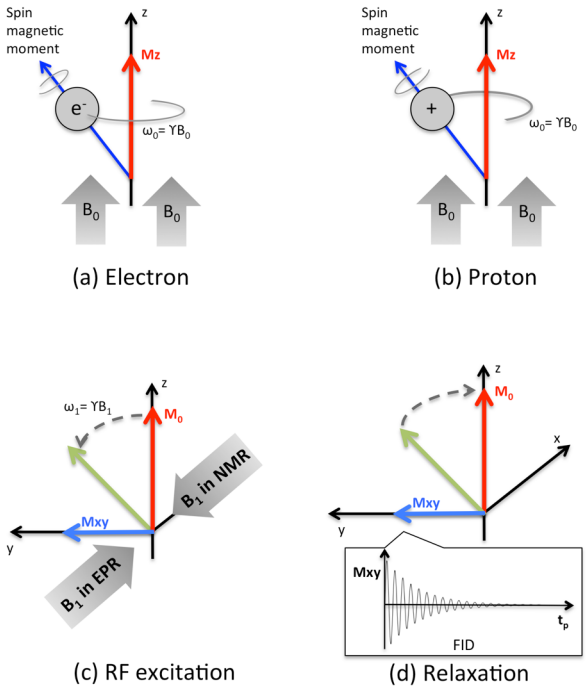

Figure 2. 1. EPR and NMR. Precession of (a) electron and (b) proton, (c) RF excitation, and relaxation.

recovery respectively. During the recovery, the transverse magnetization can be measured by receiving the emitted electromagnetic wave (RF signal) oscillating with Larmor frequency ω_0. The signal can be modeled as the following equation with time constant T_2 characterizing the signal decay in transverse plane.

$$M_{xy}(t) = M_{xy}(0)\, e^{-\frac{t}{T_2}} e^{i\omega_0 t} \tag{2.6}$$

In reality, due to imperfect imaging environments such as inhomogeneous B_0 field and magnetic susceptibility, the transverse magnetizations are dephased with a certain probabilistic distribution, and the signal decay is accelerated. The contribution of the unknown, miscellaneous dephasing factors are modeled as an additional time constant T_2' as following equation.

$$M_{xy}(t) = M_{xy}(0)\, e^{-\left(\frac{1}{T_2}+\frac{1}{T_2'}\right)t} e^{i\omega_0 t} = M_{xy}(0)\, e^{-\frac{t}{T_2^*}} e^{i\omega_0 t} \tag{2.7}$$

The total signal decay above is called T_2* decay, T_2* relaxation, or free induction decay (FID). Larmor precession term, $e^{i\omega_0 t}$, can be removed by assuming that observer is in a coordinate system rotating with ω_0, called rotating frame.

2.2 Imaging

2.2.1 Overview of EPRI/MRI hardware

In EPRI and MRI, a Fourier transform based pulsed imaging system is commonly used because of its efficiency, where a broad band RF pulse is applied to simultaneously excite all magnetization in region of interest, and spatially encode to localize individual magnetization. There are three essential elements for the Fourier transform based pulsed MRI or EPRI: a main magnet, a RF system, and a gradient system. A main magnet is used to generate homogeneous

external magnetic field, B_0, which is commonly 1.5-7T in MRI and 10-20mT in in vivo EPRI. In MRI a superconducting magnet is commonly used to obtain high and homogeneous B_0 fields, while an electromagnet is used in EPRI due to low B_0 field requirements. Active or passive shimming is standard in a MR system, while no shim is typically incorporated in a EPR system yet.

A RF system governs transmission and reception of RF signals, which operates at the Larmor frequency ω_0. In MRI, various RF coils specialized in different body parts are used for a clinical use such as a head coil, a knee coil, a wrap coil, and a chest coil other than a body coil installed in magnetic bore. In EPRI, a coil attached to a small resonator is commonly used. An extensive review of the RF coils utilized in EPRI and MRI is not possible here. The reader is referred to these articles[14–20] for further review.

A gradient system is composed of an x, y, and z gradient, which generate linearly varying magnetic field superimposed on B_0 in each direction. A Helmholtz coil for z-gradient and a saddle coil for x and y gradient are commonly used[21,22]. Strength of the gradient is controlled by a waveform generator, depending on hardware specifications such as a slew rate (temporal change, in a unit of mT/m/sec) and a maximum gradient amplitude (spatial change, in a unit of mT/m). Gradients are used for encoding k-space.

2.2.2 Spatial encoding

In pulsed EPRI and MRI magnetizations within the desired field of view (FOV) are simultaneously excited by RF pulse (B_1), and a sum of total signals over space is received. In MRI and EPRI, Fourier transform based encoding is used, where data acquisition is performed in spatial frequency domain (k-space).

Without a gradient field applied, there is ideally no phase term in the transverse magnetizations observed in rotating frame (Figure 2.2(a)), where the acquired signal is the sum of all magnetizations over the FOV. This can be interpreted as the DC component, represents a center of k-space. With a gradient magnetic fields turned on (Figure 2.2(b)), a linearly grading magnetic field (G_x Tm^{-1}) is superimposed to B_0 field which slightly changes resonance frequency, resulting in a phase shift in transverse magnetizations, M_{xy}. The phase shift at spatial position x after time t elapsed can be calculated by $\phi(x, t_p) = \int \gamma x G_x(t) dt$. Therefore, now we get a sum of phase-modulated signals as following.

$$S(t_p) = \int M(x) e^{i\phi(x,t_p)}\, dx = \int M(x) e^{i\int \gamma x G_x(t) dt}\, dx. \tag{2.8}$$

, which can be interpreted as the Fourier transform at the point k_x in k-space.

$$S(k_x) = \int M(x) e^{-i2\pi\left(\frac{\int \gamma G_x(t) dt}{2\pi}\right)x}\, dx = \int M(x) e^{-i2\pi k_x x}\, dx. \tag{2.9}$$

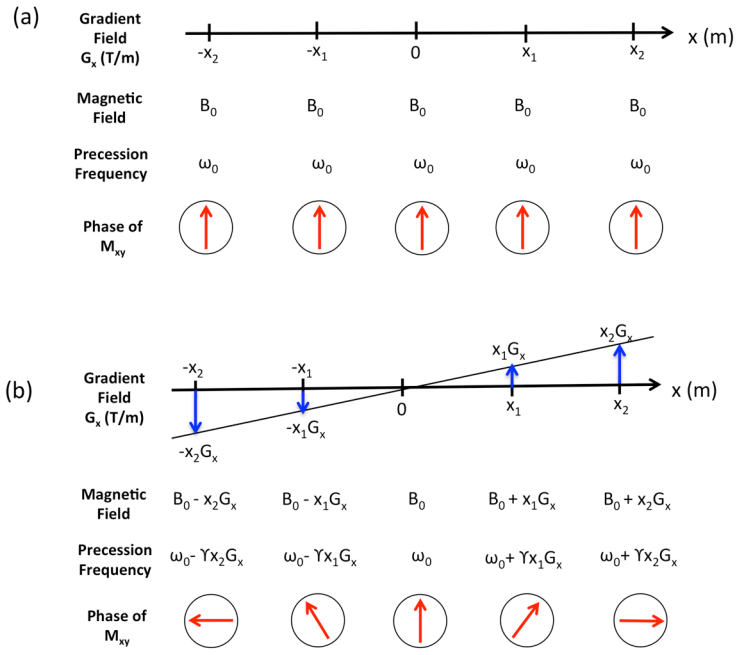

Figure 2. 2. Spatial encoding. (a) Without gradient and (b) with gradient

The encoded k-space point is determined by $k_x = \frac{1}{2\pi}\int \gamma G_x(t)dt$. By using various G_x's, we can encode other points in k-space. N linearly scaled G_x's are commonly used to encode N different points in the first dimension (here x-axis) in k-space. This is called phase encoding, in which one k-space position (in one axis) is encoded per each TR (time repetition: time interval divided by each RF excitation). Phase encoding (Figure 2.3(b)) is commonly followed by frequency encoding (Figure 2.3(c)), where k-space encoding is performed with gradient turned on. The k-space position in the frequency encoding direction changes over encoding time τ as in $k_y = \frac{1}{2\pi}\int_0^\tau \gamma G_y(t)dt$. To encode 3D k-space, three gradients are simultaneously applied to move k-space encoding position to the desired position where frequency encoding begins, and then frequency encoding is performed in the desired trajectory.

2.2.3 Image reconstruction

Once a k-space is acquired, an image can be reconstructed by inverse discrete Fourier transform. In the case that k-space samples are not on the Cartesian grid (non-Cartesian),

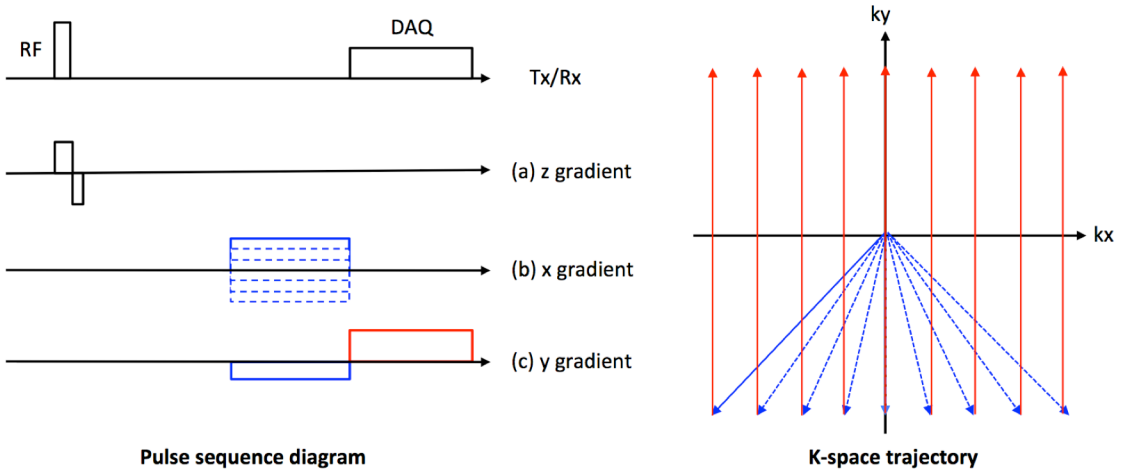

Figure 2. 3. An example of 2D Cartesian encoding (Gradient echo imaging) (a) slice selection in z-direction, (b) phase encoding in x-direction, and (c) frequency encoding in y-direction. Note that in (a) slice selection is performed by applying effective z-gradient during RF excitation, which results in selective excitation along z-direction, depending on RF bandwidth and gradient strength.

NuFFT[23] or convolution gridding[24] is commonly used to get Cartesian k-space. In this thesis, we utilize a convolution gridding method for non-Cartesian reconstructions.

Chapter 3. Single Point Imaging

3.1 Theory

3.1.1 Conventional single point imaging

Single point imaging (SPI), which is also known as a constant time imaging, was first proposed to image solid objects by Emid and Creyghton in 1985[5]. In conventional SPI a k-space is purely phase encoded using constant gradients and a broadband RF pulse, where the phase encoding gradient is linear scaled from –Gmax to Gmax with equi-spaced encoding steps over TRs as shown in Figure 3.1. Note that a single k-space data point is acquired in each TR at a constant phase encoding time delay, t_p, where a desired FOV or spatial resolution is achieved. FOVs of SPI images are calculated using a well-known FOV equation for phase encoding as

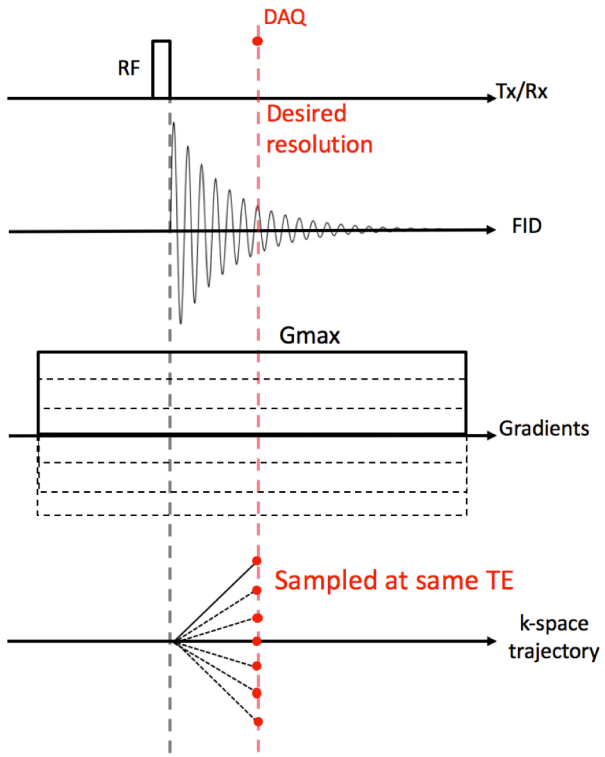

Figure 3. 1. Single point imaging

following.

$$FOV(t_p) = 2\pi N/(\gamma \int_0^{t_p} G(t)dt) \quad (3.1)$$

, where G(t) denotes gradient shape that is a function of encoding time, t. In the convention SPI where constant gradients are used with maximum phase encoding gradient amplitude, Gmax, a FOV at t_p is calculated as following equation.

$$FOV(t_p) = \frac{2\pi N}{\gamma t_p Gmax}. \quad (3.2)$$

In the conventional SPI, only one image at t_p, is commonly acquired. SPI imposes longer

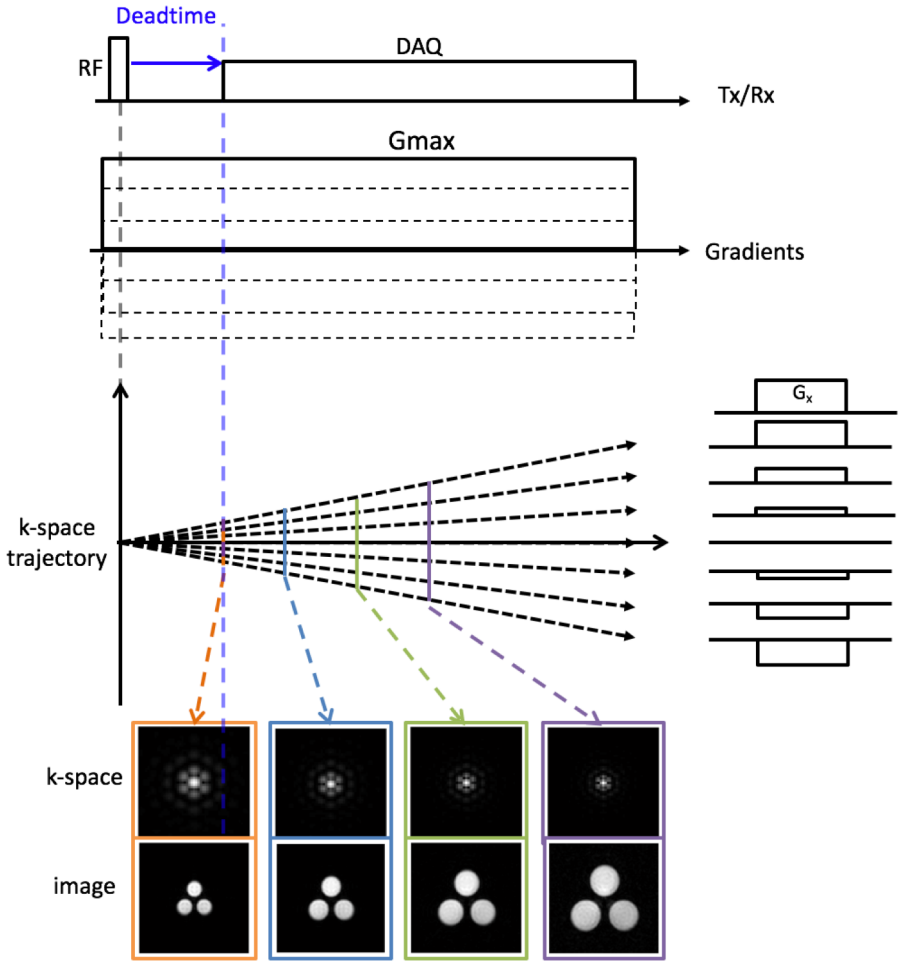

Figure 3. 2. Dynamic single point imaging

encoding time than frequency encoding. For example, to obtain NxN or NxNxN Cartesian k-space, SPI requires N times longer scan time. Therefore, SPI is not a popular imaging scheme in MRI. However, owing to the k-space data acquired in a constant time, image quality and spatial resolution in SPI are not limited by readout bandwidth or T_2* relaxation effect (or T_2* blurring effect) as in frequency encoding. Moreover, SPI is more robust to magnetic susceptibility artifact.

3.1.2 Dynamic single point imaging

Dynamic SPI, termed by Jang and McMillan[25], harnesses temporal data discarded in conventional SPI. In dynamic SPI, multiple single point images are consecutively obtained with highest readout bandwidth (e.g., sampling interval = 2μs in a recent MR system and 4ns in EPR system). Figure 3.2 shows a simple example of dynamic SPI, where data are acquired after RF coil deadtime until the end of the encoding gradient. Most important goal in dynamic SPI is to enable reliable T2* parameter estimation by utilizing the high-resolution temporal data. One challenge to achieve the goal is time changing FOV or spatial resolution as shown in Figure 3.2.

Moreover, in EPRI where matrix size is limited (typically smaller than 21x21x21), strong Gibbs ringing artifact is exhibited with the pattern changing over phase encoding time delays in dynamic SPI, resulting in oscillation in the pixelwise temporal data, which needs to be address for accurate T2* estimation. In Chapter 4 and 5, novel methods to solve the issues are presented, where dynamic SPI images with same FOV and time-invariant Gibbs ringing artifacts are obtained for reliable T2* parameter estimation in EPRI.

In conventional SPI in MRI, it is common to place a broadband RF pulse and perform encoding at constant part of a gradient as in EPRI, which simplifies calculation of TE with

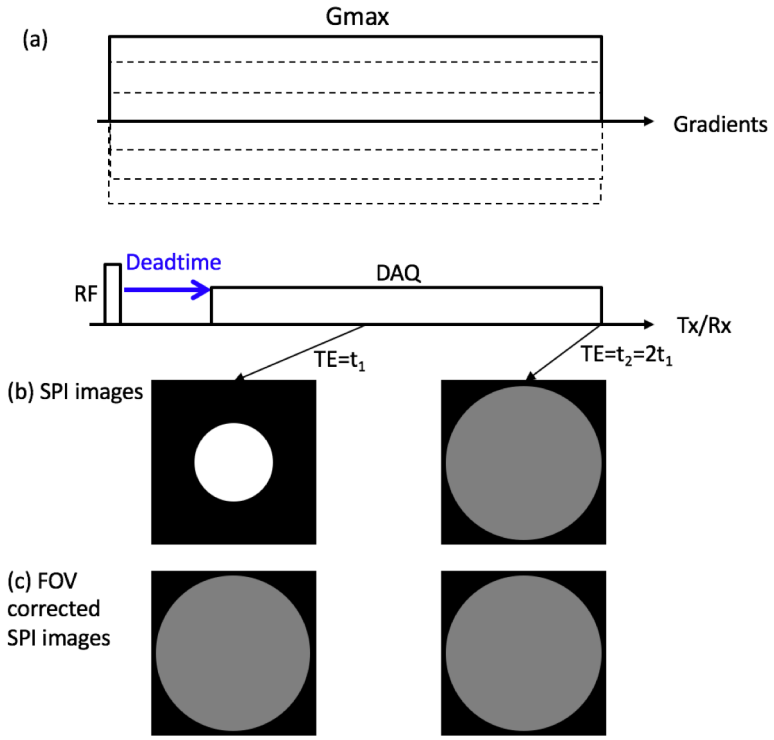

Figure 3. 3. FOV correction in dynamic SPI. (a) PSD, (b) SPI images with native FOV, and (c) FOV corrected images

desired spatial resolution. However, theoretically any shape of gradient can be used for SPI, which results in error in FOV if actual shape of a gradient waveform is not measured correctly. In dynamic SPI, accurate estimation of actual gradient shape is more important since inaccurate estimation of gradient shape can deviate temporal data, misleading T2* estimation, as describe in the following section.

3.1.3 FOV correction in dynamic SPI

In Dynamic SPI, accurate FOV correction is prerequisite for parameter fitting since the FOV correction corrects for not only size of subject but also voxel intensity. For example, let's think about a simple case shown in Figure 3.3(a), where a circular object is imaged with 2D dynamic SPI using constant gradients with maximum phase encoding gradient amplitude, Gmax.

Let's assume there is no T2* decay over encoding (T2* is infinite). Even though there is no signal decay inside object, the obtained SPI images show different intensity since voxel size changes over encoding, depending on prescribed SPI gradients. For example, FOV at TE=t_1 will be 2x larger than that at TE=t_2 if where t_2=2t_1, according to equation 3.1. Therefore, pixel intensity in the SPI image at TE=t_1 will be 4x higher than the image at TE=t_2 since voxel size is 4x larger at TE=t_1 as shown in Figure 3.3(b).

Now, we want to rescale the object (or rescale FOV) at TE=t_1 to match with the object size at TE=t_2. Then, a rescaling factor=2 can be determined using following equation based on equation 3.1.

$$scale(t_1, t_2) = \frac{\frac{2\pi N}{\gamma t_1 Gmax}}{\frac{2\pi N}{\gamma t_2 Gmax}} = \frac{t_2}{t_1} = \frac{2t_1}{t_1} = 2. \quad (3.3)$$

If the scaling factor is correctly estimated, the pixel intensity of object at t_1 will decrease to 25% of original intensity after scaling since now the pixel size is 4x smaller, matched with the intensity of the image at t_2 as shown in Figure 3.3(c). However, if the scaling factor is incorrectly estimated, it will distort signal intensity in the scale-corrected image at TE=t_1. For example, the scaling factor is estimated as 1.9 instead of 2, the resultant pixel intensity will be now 27.7% of original intensity after scaling, which causes 10.8% error (overestimation in intensity) in pixel intensity. In the case of 3D imaging, this error will be more significant, which causes 16.6% error (overestimation in intensity) in the example above.

In the case of using constant SPI gradients, this error will be negligibly small since FOV estimation is trivial. However, when an arbitrary shape of gradient is used, accurate measurement of gradient waveform is necessary. In Chapter 6, we present a novel way to measure gradients

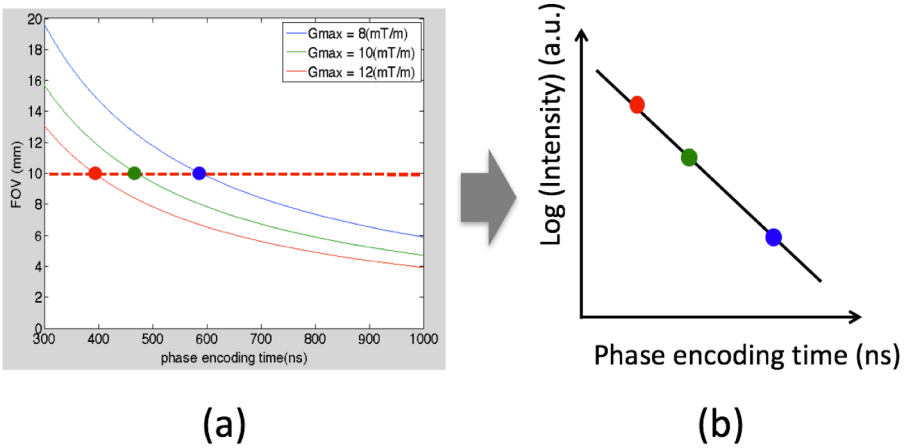

Figure 3. 4. Conventional SPI-based EPR oximetry. (a) FOV curves in dynamic SPI with 3 different maximum phase encoding amplitudes, and (b) T2* estimation.

based on dynamic SPI.

3.2 Related works

3.2.1 EPR oximetry

Due to the extremely short T_2* decay in EPR oximetry, SPI has been recently revisited as an effective imaging scheme[7,26]. In the methods, multiple data acquisitions are performed with different maximum phase encoding gradient amplitudes (G_1, G_2, G_3,…,G_n). Then, data acquisition time point in FID, $t_p(i)$, in the data acquisition using Gmax=G_i can be found based on the following equation.

$$t_p(i) = \frac{2\pi N}{\gamma G_i FOV_D}, \qquad \text{i=1,2,…,n} \tag{3.4}$$

, where FOV_D denotes a desired FOV that is kept same between different data acquisitions. Typically, three data acquisitions (n=3) are performed due to the long scan time. Figure 3.4(a) shows how FOV changes over phase encoding time delays in three different Gmax's (8, 10, and 12mT/m). Then, three SPI images with a same FOV (10mm in Figure 3.4(a)) is used for T2* estimation as shown in Figure 3.4(b).

More advanced methods based on dynamic SPI that enable EPR oxygen imaging with a single acquisition reduce the total scan time by at least a factor of 3x[10,12], which is described in Chapter 4 and 5.

3.2.2 MRI

In MRI, SPI has been explored in literature[27–32]. One application of SPI has been for industries to image solid materials with short T_2* decay such as concrete, ceramic, or cement, where scanning time was not an important factor like it is in the clinic[33]. Recently, hybrid encoding based on SPI has been lime-lighted again for clinical imaging scheme[8,34]. In the hybrid encoding, SPI is used to enable fast radial encoding, where central part of k-space is encoded by SPI. An advanced hybrid encoding scheme[13] and its applications are demonstrated in Chapter 7, 8, and 9.

There have been studies to use SPI concept (or pure phase encoding) to measure actual gradient waveform[29,35,36], to benefit from SPI's robustness to T2* decay effect. More advanced and rapid method has recently been introduced in literature, using dynamic SPI[25], which is described in Chapter 6.

Chapter 4. Single Acquisition Single Point based EPRI

4.1 Introduction

Electron paramagnetic resonance (EPR) is a spectroscopic technique that measures the magnetic moment of unpaired electron systems. Through the use of paramagnetic spin probes, EPRI has surfaced as a promising non-invasive technology for dynamically imaging in vivo tissue oxygenation, where linewidth or R_2* is proportional to pO_2[7,37,38]. Knowledge of the spatial distribution and dynamic changes of tissue oxygenation allows identification of critical intratumoral hypoxic regions where hypoxic tumor cells show high resistance against radiation and chemotherapy[39,40]. Image quality in EPRI benefits from the use of single point imaging (SPI) techniques due to extremely short spin-spin relaxation times[6]. The SPI scheme acquires the entire free induction decay (FID) signal for a single point in k-space under static phase encoding gradients. Though SPI requires long acquisition time due to point-by-point phase encoding, it is possible to obtain better imaging quality with less susceptibility artifact[26,41]. Additionally, the signal may be sampled over an extended time range allowing quantification of relaxation parameters.

One notable characteristic of SPI is the "zoom-in" effect resulting in decreasing field of view (FOV) and enlargement of the object as time delay increases[6]. This phenomenon inhibits the direct fitting of pixelwise T_2* since co-located pixel position changes over time. Therefore, conventional acquisition techniques in EPRI using SPI techniques have required repeated imaging experiments with differing maximum gradient amplitudes (typically 3) to secure multiple images. Images can be reconstructed at different phase encoding time delays (tp) with identical FOV allowing estimation of T_2*[7], which, however, reduces the achievable temporal

resolution. In related MRI techniques, the chirp-z transform has been previously used to reconstruct single-point images into images with a consistent FOV and perform T_2* measurement[9,31,42]. In this paper, we describe the use of gridding techniques to reconstruct images with equal FOV. However, equal FOV methods alone are not sufficient to reliably estimate T_2* due to k-space truncation artifacts inherent in the low-resolution of EPR images.

The true object in MRI and EPRI is continuous, thus discrete sampling itself is windowing of the true k-space. It is from this sampling window that Gibbs ringing occurs in these modalities. At sufficiently high matrix sizes (e.g., conventional MRI resolution of 256x256), this ringing artifact is minimal (high in frequency). However, due to time constraints imposed by the SPI acquisition, EPRI acquisitions are limited in spatial resolution. Limited acquisition matrix size results in truncation of a significant portion of high frequency components in k-space, resulting in unavoidable and significant Gibbs ringing artifacts in reconstructed images that are difficult to remove and impair the quality of image as shown in Figure 4.2. Similar artifacts are apparent in magnetic resonance spectroscopic imaging[43,44], which utilizes a similar resolution. In SPI, as images are reconstructed at different phase encoding time delays (t_p), the spatial frequency of ringing artifact increases as the FOV decreases and the degree of truncation decreases. This time-variant ringing artifact inhibits accurate T_2* estimation as it generates irregular oscillations in the reconstructed FID signal. To resolve this problem, we have implemented a k-space extrapolation method that improves image quality over time by propagating the high frequency components in a cascading manner, similar to the recently reported multi frame SPRITE method utilizing the chirp-z transform[31]. Note that Gibbs ringing is not eliminated; however, it remains constant in the reconstructed images to allow improved and more reliable estimation of T_2* and hence accurate measures of oxygenation.

4.2 Methods

4.2.1 Reference FOV and scaling factor

The zoom-in effect of SPI, shown in Figure 4.2, can be expressed with the following equation.

$$FOV(t_p) = 2\pi/(\gamma_e t_p \Delta G) \tag{4.1}$$

where ΔG is incremental gradient step, γ_e is gyromagnetic ratio of the electron, and t_p is the phase encoding time delay following the RF pulse. Let reference FOV, FOV(t_{ref}), denote the desired FOV that images will be reconstructed into. When selecting the reference FOV, it is desirable to consider using the FOV that minimizes excessive interpolation. Typically this would suggest that the middle t_p should be used; however, due to the implementation of the k-space extrapolation method described below, we chose FOV(t_{ref}) to be equal to the final FOV in order to maximize the spatial resolution of the ensemble images. Once the reference FOV is determined, scaling factor at current time delay t_p is estimated as given with equation (4.2), which will be used in subsequent gridding.

$$s(t_p) = FOV(t_{ref})/\, FOV(t_p). \tag{4.2}$$

To reconstruct images with a constant FOV, we employed the well-known convolution gridding methods using a Kaiser-Bessel kernel[45,46]. The sampled k-space data were gridded to a new k-space with the inter-sample distance scaled by the scaling factor, s(t_p). Note that in the current EPRI spectrometer, deadtime depends on the saturation and recovery of the preamplifier following the application of the RF pulse, where recovery is generally faster with higher gradient magnitude. Due to the nonlinear characteristic of recovery in preamplifier, it is difficult to accurately estimate the actual deadtime. When deadtime is incorrectly estimated, FOV and FOV

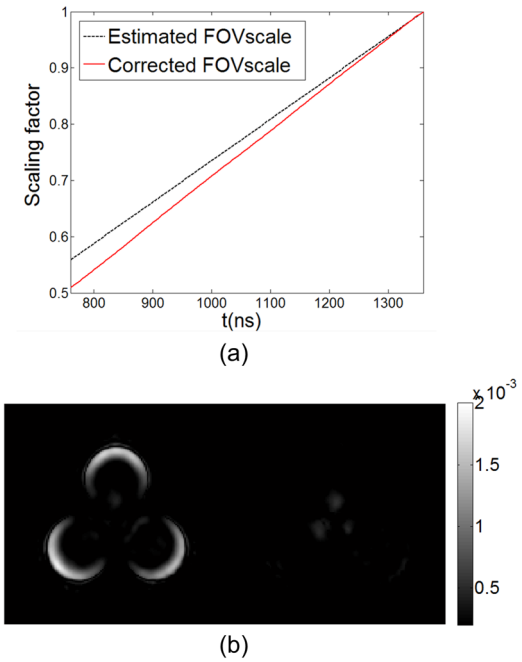

Figure 4. 1. Correction for FOV scaling factor. (a) Uncorrected FOV scaling factor vs. corrected FOV scaling factor, and (b) Difference between images reconstructed at the first time delay (760 ns) and the last time delay (1360 ns), with uncorrected (left) or corrected (right) FOV scaling factor. To compensate for FID between two images, each image was normalized by its average intensity.

scaling factor, $s(t_p)$, are also incorrectly estimated, and hence images are reconstructed at different FOVs as seen in Figure 4.1 (b). To correct the scaling factor, we used nonlinear optimization (Nelder-Mead Simplex) to automatically determine the optimal scaling factor $s(t_p)$ that minimized the difference between the reference image and current image, both reconstructed using the gridding mentioned above. Figure 4.1 (a) shows the estimated scaling factors and corrected scaling factors obtained using the abovementioned method. Figure 4.1 (b) shows difference between images reconstructed at the first time delay and the last time delay with estimated or corrected scaling factor.

4.2.2 T_2 fitting*

Once images with equal FOV are secured, pixelwise T_2* may be estimated by fitting the reconstructed FID signal to the following FID equation.

$$M = M_0 \exp\left(-t/T_2^*\right). \tag{4.3}$$

In this study, we used linear least squares fitting to estimate T_2* using the log linearization of the FID data.

Unfortunately, gridding alone is not sufficient to allow accurate quantification of T_2*. In practice, due to the low resolutions used in EPRI, images are corrupted by Gibbs ringing due to truncation as a result of the narrow k-space sampling bandwidth. This matter is further complicated by the time-decreasing FOV, and the time-increasing k-space sampling bandwidth of SPI, which results in an increasing frequency of Gibbs ringing artifacts as phase encoding

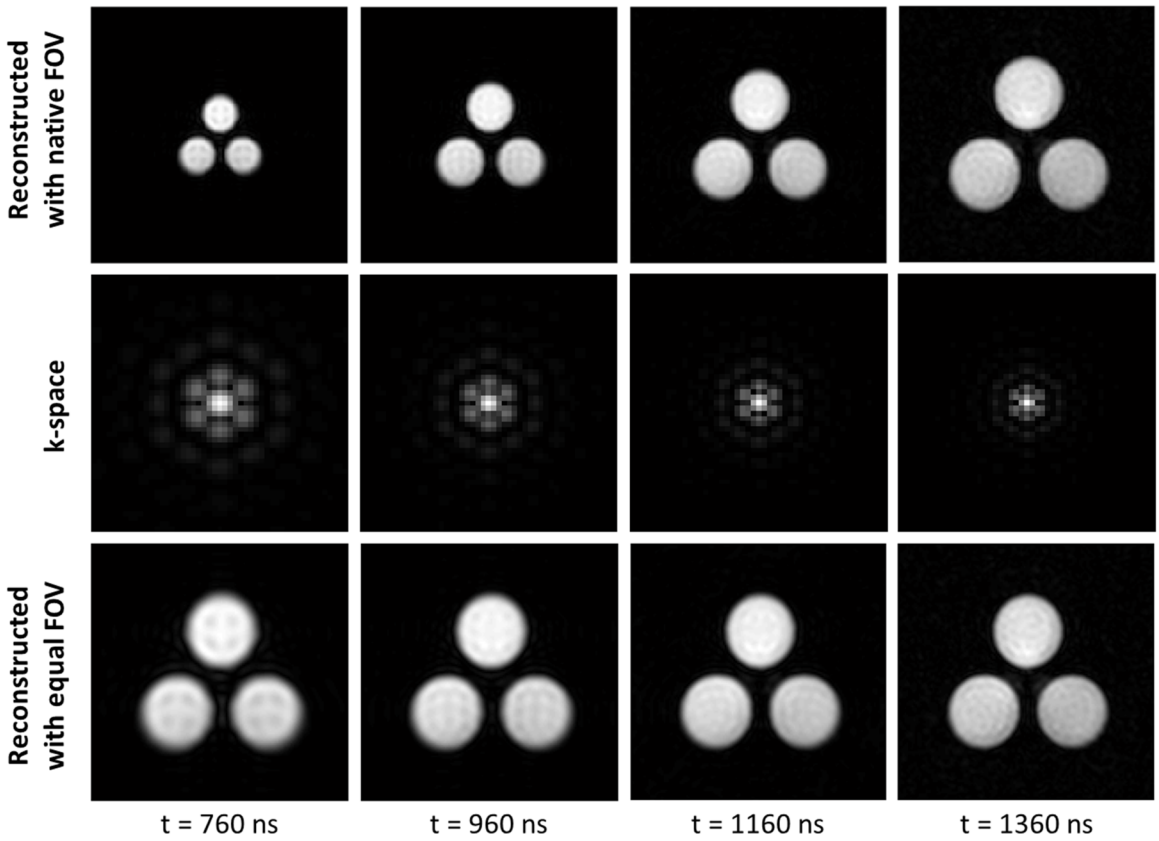

Figure 4. 2. Time-variant FOV and Gibbs ringing in SPI. 3-tube phantom data was reconstructed into native FOV (top) or equal FOV (bottom). Gridding was used to obtain images with equal FOV. Note that in both cases, the frequency of ringing artifact increases with time.

time delay increases. Figure 4.2 shows images with increasing time delay and characteristic time-varying ringing artifact, which complicates T_2* fitting for images regridded to a consistent FOV. Although methods have been proposed to alleviate Gibbs ringing artifacts in MRI by extrapolation[47–52], it is difficult to apply these techniques to EPRI due to its inherent low-resolution. To address this issue, in the next section we explore a k-space extrapolation method that enforces spatially-invariant Gibbs ringing across phase encoding time delay to enable a more robust measurement of tissue oxygenation status.

4.2.3 k-Space extrapolation

As described above (as shown in Figure 4.2), the frequency of Gibbs ringing changes with sampling bandwidth in k-space. Thus, if we can keep sampling bandwidth same, then we can achieve time-invariant Gibb ringing artifact for all reconstructed images. To do this, k-space from the later time delays (with smaller FOV, and higher spatial resolution) can be extrapolated to the k-space from earlier time delays (with larger FOV, and lower spatial resolution).

Figure 4.3 (a) shows the concept of k-space extrapolation method used herein, which propagates high frequency coefficients in later k-spaces to earlier k-spaces in a cascading manner. The following equation is used to determine the size of the region to be filled with propagated data, N_{filled}, where N is the matrix size of k-space.

$$N_{filled} = \left\lceil N\left(1 - FOV(t_{ref})/FOV(t_p)\right)\right\rceil. \quad (4.4)$$

Based on equation 4.4, a masking window is constructed for each k-space, which is used to combine k-spaces. When constructing masking windows, a merging filter can be applied to smooth the edge of mask, to avoid abrupt changes in k-space. This was implemented by convolving a 3x3 spatial averaging filter with the masking window. The propagated data is

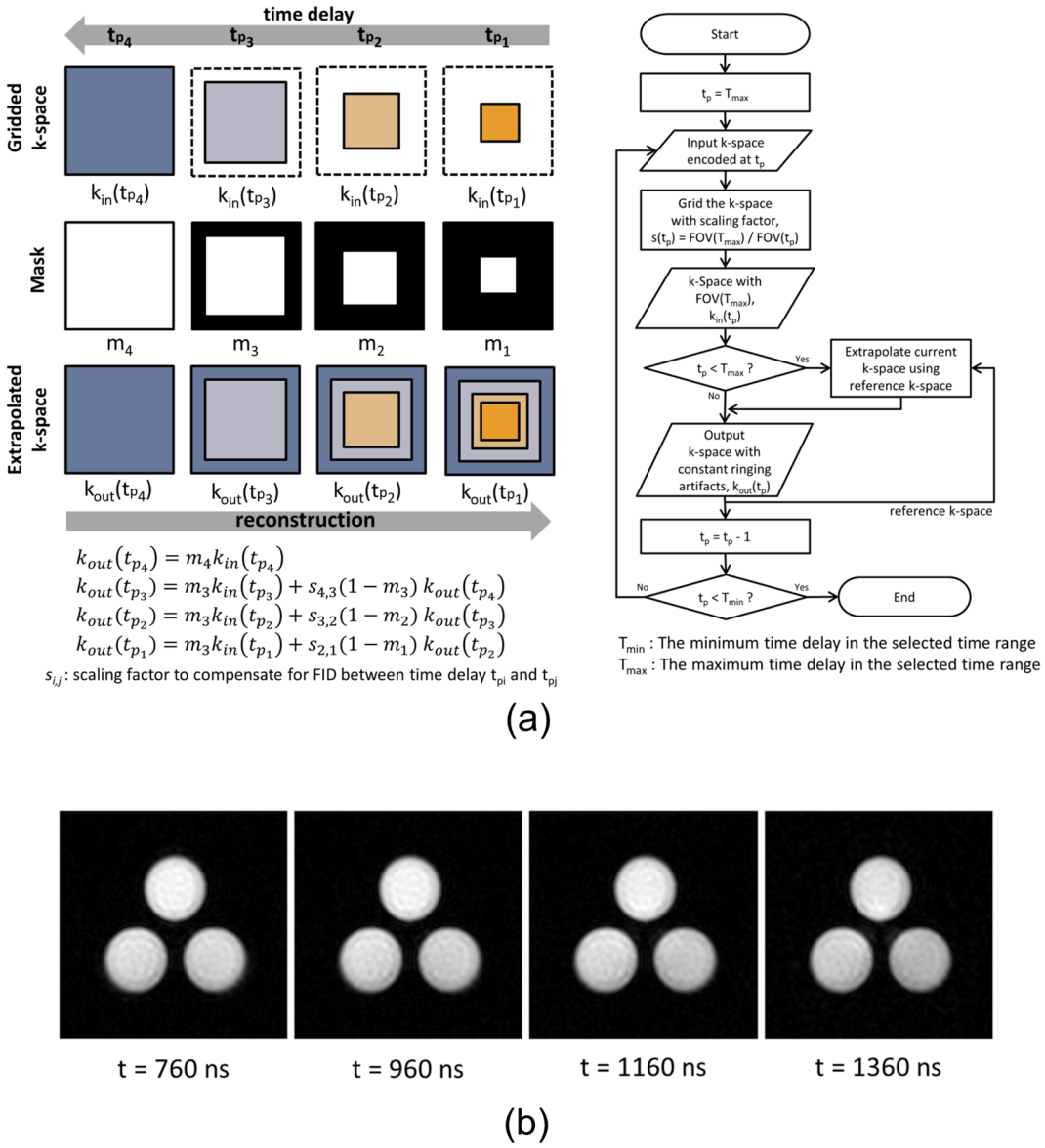

Figure 4. 3. k-Space extrapolation. (a) Concept of k-space extrapolation (phase encoding times, $t_{p4} > t_{p3} > t_{p2} > t_{p1}$), and (b) Reconstructed images with application of k-space extrapolation. Note that the k-space extrapolation method makes similar Gibbs ringing at different time delays.

multiplied by a scaling factor to compensate for inter image T_2* decay, where the scaling factor is determined by the ratio of the maximum coefficient in each k-space. To test different methods of k-space extrapolation, we tested implementations without scaling, using scaling as described above, and using scaling with a merging filter to ensure a smooth transition between the original and extrapolated k-space. As seen in Figure 4.3 (b), similar pattern of ringing artifact emerges at

different time points when k-space extrapolation method is applied.

4.2.4 Linewidth and pO_2 quantification

In EPRI, oxygen concentration (pO_2) can be quantified based on the linewidth of the spin probe that can be expressed with sum of two terms, LW' and LW_o as following equation.

$$LW = LW' + LW_o = LW' + \alpha \times pO_2 \tag{4.5}$$

where LW' denotes sum of oxygen-independent LW terms and LW_o denotes oxygen-dependent LW broadening that is linearly proportional to pO_2. In EPRI, LW (full width at half maximum height, FWHM) can be calculated from T_2* by

$$LW = 1/(2802\,\pi\,T_2^*)\ \ mGauss. \tag{4.6}$$

Since LW can be estimated by fitting the sampled FID data, a pO_2-LW calibration curve can be fitted by imaging samples with known pO_2.

4.2.5 Experimental setup

To evaluate the capability of quantitative oxygenation measurement using the abovementioned techniques, a computer simulation, a calibration phantom test, and an in vivo imaging study were performed. To simulate the calibration phantom experiment, synthetic EPRI images with much higher resolution than conventional EPRI acquisitions (255x255) were generated using MATLAB (The Mathworks, Natick, MA). The simulated data consisted of 3 tubes with different T_2*'s (200ns, 160ns and 110ns) that respectively correspond to approximately 3%, 30%, and 90% oxygen levels according to our tube phantom calibration result. T_2* shorter than these was not taken into account since current EPR scanner does not allow imaging of objects with extremely short T_2* due to the relatively long deadtime of RF transmitter/receiver (usually

longer than 200ns). Moreover, our interest is in detecting hypoxia rather than imaging highly oxygenated object, hence simulation was performed with object oxygenated less than 90%. Simulated decay curves were generated for 300 points using a sampling rate of 5ns. To simulate SPI encoding, inverse gridding was used to sample k-space with a 49x49 matrix with a spreading Dirac comb function to simulate the zoom-in effect. To create a reference standard for the simulation, the same 3-tube data was generated as above without a time-decreasing FOV (zoom-in effect), which does not require equal FOV reconstruction or k-space extrapolation. For both datasets, the SNR was set to 150 at 800ns (comparable to real experimental results) and the same level of noise power was applied to the entire FID.

Details regarding the specifications of the EPRI spectrometer have been previously published[2,53]. For the tube phantom experiment, 3D EPR data was obtained using three-tube phantom comprised of three tubes containing 2 mM Oxo-63 (GE Healthcare, Waukesha, WI) bubbled with respectively 0%, 2% and 5% oxygen. Data was encoded using three orthogonal phase-encoding gradients incrementally ramping in 19 equal steps from –8 to 8 mT/m, resulting in 19x19x19 phase-encoding steps. Data points were encoded at constant time, every 5ns after the minimum RF recovery dead time (360ns). 4000 averages per phase encoding point and an interpulse delay (TR) of 5.5 μs was used. Pixelwise T_2* was estimated and the mean T_2* from each tube was used to calibrate %-oxygenation to T_2* as a first order polynomial using linear least squares[6], which was later used in the in vivo experiment to quantify tissue oxygenation. The calibration was calculated across a range of phase encoding time delays of 400 ns in duration, and at an extended range of 600 ns. In addition, datasets obtained under various phase encoding gradients ranging from 8 to 13 mT/m were tested to verify the influence of the strength of phase encoding gradient field on T_2* estimation. Time range [800 ns, 1200 ns] was used for the test.

For the in vivo experiment, 3D EPR data was obtained from a SCC (squamous cell carcinoma) tumor bearing leg of a C3H mouse. Animals (Frederick Cancer Research Center, Animal Production, Frederick, MD) were housed in a climate controlled room and fed ad libitum. Tumor (SCCVII) cells were injected subcutaneously as a single suspension of 106 cells in the right hind leg. Tumors grew to 1.5 cm diameter (~1.8 cm^3 in volume) in approximately 10 days. All in vivo experiments were carried out in compliance with the Guide for the Care and Use of Laboratory Animal Resources (National Research Council, 1996) and approved by the National Cancer Institute Animal Care and Use Committee. Mice were anesthetized by isoflurane (1.5%) inhalation and mounted prone with hip positioned downwards on a home built transmit-receive resonator coil. Breathing rate (60 ± 10 per min.) was monitored by a pressure transducer (SA Instruments, Inc., Stony Brook, NY). Core body temperature was maintained at 37 ± 1 ºC by a steady flow of warm air. A 30 gauge needle was cannulated into the tail vein and extended using an optimum length of polythene tubing to administer the Oxo-63 spin probe (GE Healthcare, Waukesha, WI). Gradient step size was set to 19x19x19 (G_{max} = 11.4 mT/m) and other settings were set identically to the three-tube phantom data acquisition.

4.2.6 Data Processing

Using the aforementioned methods, T_2* was fit over varying ranges of phase encoding time delays to determine the dependency of chosen time range upon the accuracy of T_2* estimation. For each time range, the latest time delay/minimum FOV was used as the reference FOV. Images were reconstructed in reverse order, from the largest time delay to the smallest time delay, and high frequency components were propagated to the earlier time delays, as explained above. With serial images of differing time reconstructed over a time range, pixelwise T_2* was estimated by fitting the data to the equation 4.3 using linear least squares of the log-

linearized equation, where the estimated slope represents $-1/T_2^*$, and the resultant T_2^* map was converted into a LW map. For the tube calibration, the pixelwise LWs were grouped into each tube, and an average LW for each tube was used to generate a pO_2-LW calibration curve.

4.3 Results

4.3.1 Simulation results

To evaluate how accurately our proposed method estimates pixelwise T_2^*, we simulated SPI data for three tubes with different T_2^* (200 ns, 160 ns and 110 ns respectively for upper, lower-left and lower-right tube). Figure 4.4 (b) shows two FID curves reconstructed at point A with or without application of k-space extrapolation method. The oscillation caused by time-changing Gibbs ringing was clearly eliminated by application of the k-space extrapolation method. With time range [250 ns, 650 ns], the estimated T_2^* of three tubes of the reference standard was 199.93 ± 0.32 ns, 160.00 ± 0.24 ns, and 110.49 ± 1.89 ns, respectively. The estimation of T_2^*'s using gridding with k-space extrapolation was 198.53 ± 3.29 ns, 160 ± 2.13 ns, and 111.91 ± 4.89 ns, respectively. Using gridding without k-space extrapolation the estimates were 206.91 ± 18.30 ns, 164.55 ± 11.61 ns, and 111.79 ± 5.60 ns, respectively. Application of k-space extrapolation made the T_2^* map more spatially consistent while the unprocessed T_2^* map was severely distorted by the time-varying ringing artifact, with the estimated T_2^* map and the resultant histogram are shown in Figure 4.4 (c),(d),(e). Table 4.1 shows the performance of three different strategies in extrapolating k-space: using raw data with no scaling, applying a scaling factor and applying scaling and a merging filter. As the root mean squared error shows, scaling is required for accurate T_2^* estimation, and the application of a merging filter further improves the accuracy of estimation.

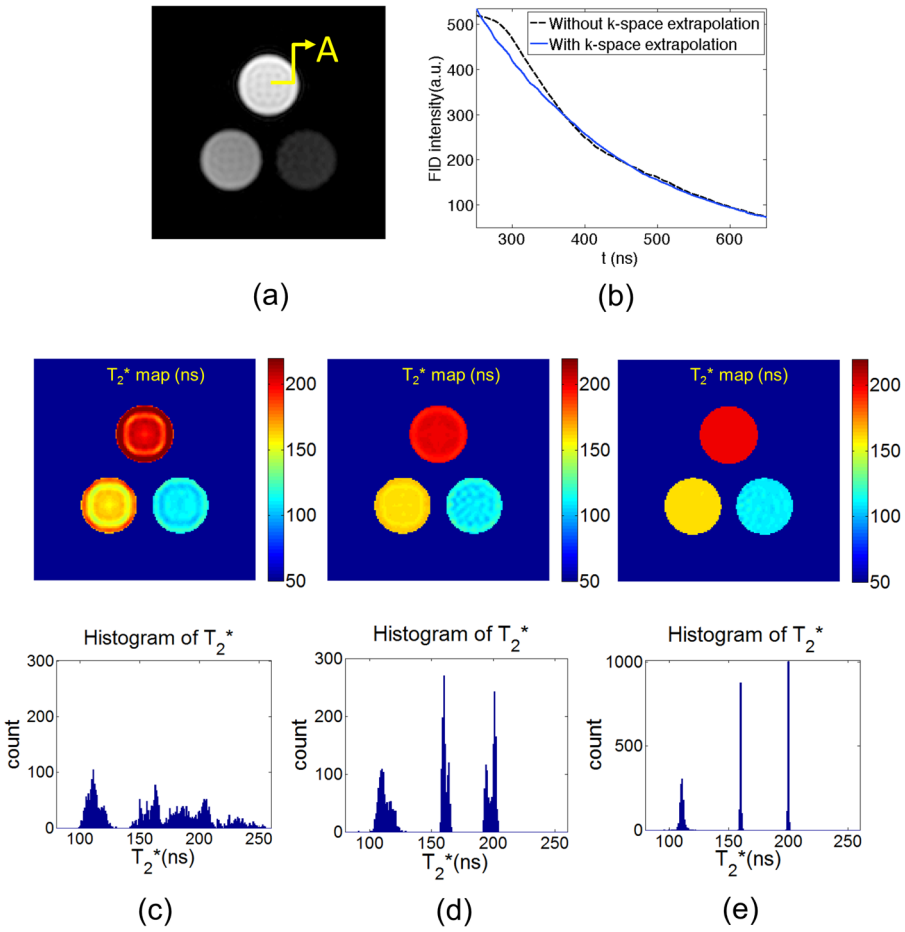

Figure 4. 4. Simulation result. (a) Reconstructed image, (b) FID curves at position A, (c) T_2* map and the resultant histogram (without using k-space extrapolation), and (d) T2* map and the resultant histogram (using k-space extrapolation). (e) T_2* map and the resultant histogram (using the reference standard). Time range [250 ns, 650 ns] was used. Note that the k-space extrapolation method reduces oscillation in the FID curve in (b), and hence more reliable T_2* estimation is possible.

Time range (ns)			Root mean squared error (ns)		
t_{min}	t_{max}	Range	Without scaling	With scaling	Scaling + merging filter
200	600	400	29.9	4.5	4.4
250	650	400	24.9	4.0	4.0
300	700	400	20.6	4.8	4.3
350	750	400	18.2	6.1	5.6
400	800	400	17.5	8.5	7.8
200	800	600	20.0	6.4	6.1

Table 4. 1. Evaluation of k-space extrapolation strategies. As the root mean squared errors show, scaling is required for k-space extrapolation to perform well, and the merging filter improves accuracy of T_2^* estimation.

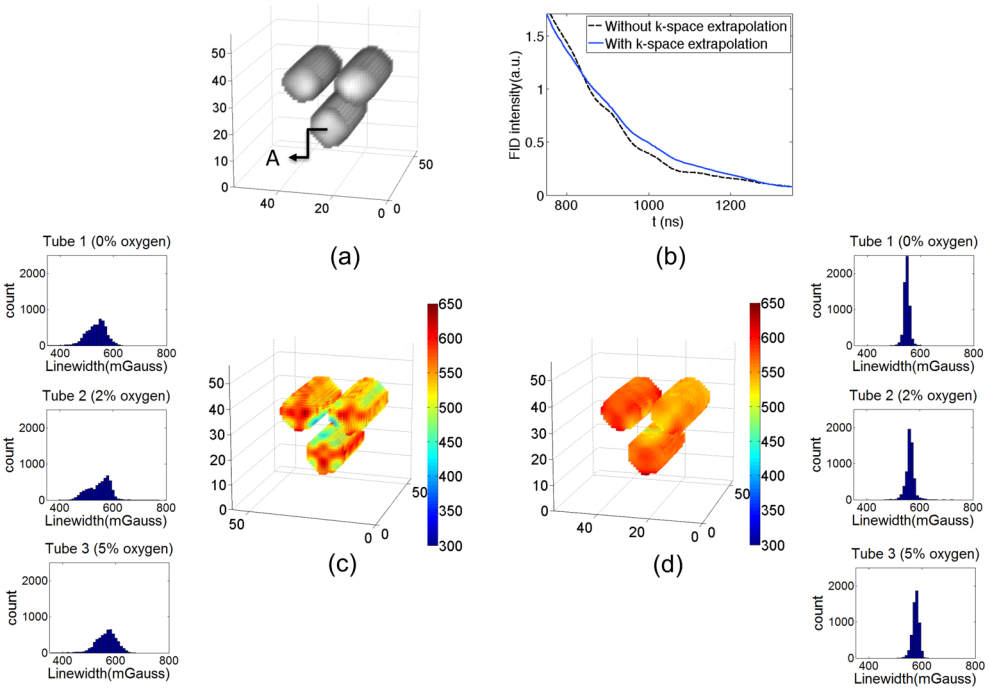

Figure 4. 5. Tube phantom result. (a) Visualization of reconstructed image (at 750 ns), (b) FID curves at position A, (c) LW map and the resultant histograms (without k-space extrapolation), and (d) LW map and the resultant histograms (with k-space extrapolation). Note that Gibbs ringing effect shown in (c) is greatly alleviated by applying k-space extrapolation in (d).

4.3.2 Tube phantom results

Table 4.2 shows quantitative result of tube calibration obtained using various time ranges. Since oscillation is not perfectly removed from the FID data in practice, presumably due to noise sources other than Gibbs ringing, as seen in Figure 4.5 (b), LW may show time range dependency if the time range used to compute T_2* is too short. In Table 4.2, slopes for the 400 ns time range are distributed within 5.36 ± 0.15 mG/% and y-intercepts are distributed within 537.39 ± 5.23 mG, with a coefficient of variation of 2.79% and 0.97%, respectively, indicating a stable estimation of T_2* across a wide time range. We determined the pO_2-LW calibration curve for the following in vivo experiments using the larger 600ns time range reconstruction (slope = 5.35 mG/% y-intercept = 549.59 mG). Figure 4.5 (c),(d) shows two 3D LW images and the resultant histograms estimated respectively using gridding alone and gridding with k-space extrapolation within a time range of [750 ns, 1350 ns]. As seen, k-space extrapolation enables

minT (ns)	maxT (ns)	Range (ns)	Slope (mG/%)	Y-intercept (mG)	R^2
750	1150	400	5.58	531.69	0.9943
800	1200	400	5.41	535.64	0.9906
850	1250	400	5.33	535.92	0.9658
900	1300	400	5.26	537.85	0.9774
950	1350	400	5.20	545.84	0.9993
750	1350	600	5.35	549.59	0.9803

Table 4. 2. Calculated LW fit with various time ranges using k-space extrapolation. The slopes and y-intercepts show little variation according to time ranges.

	Phase encoding gradient amplitude (|mT/m|)	Average LW in Tube 1 (mGauss)	Average LW in Tube 2 (mGauss)	Average LW in Tube 3 (mGauss)
Gridding with k-Space extrapolation	8	534.73	547.98	562.08
	9	546.88	554.18	569.86
	10	544.40	545.84	569.93
	11	544.29	550.30	568.37
	12	539.70	548.98	567.00
	13	543.87	553.07	571.65
Conventional method	8 10 12	546.72	551.16	572.08

Table 4. 3. LWs calculated using gridding with k-space extrapolation under various phase encoding gradients or using conventional method. Time range [800 ns, 1200 ns] was used for gridding with k-space extrapolation. Three datasets obtained under phase encoding gradients -8~8 mT/m, -10~10 mT/m and -12~12 mT/m were used to implement the conventional method.

more stable LW estimation less affected by Gibbs ringing. Table 4.3 shows the result of LW estimation obtained using gridding with k-space extrapolation under increasing phase encoding gradient and amplitude and the conventional multiple gradient method implemented using 3 different phase encoding gradients. As the result shows, gridding with k-space extrapolation allows LW estimation as accurate as the conventional method, regardless of the strength of phase encoding gradient field.

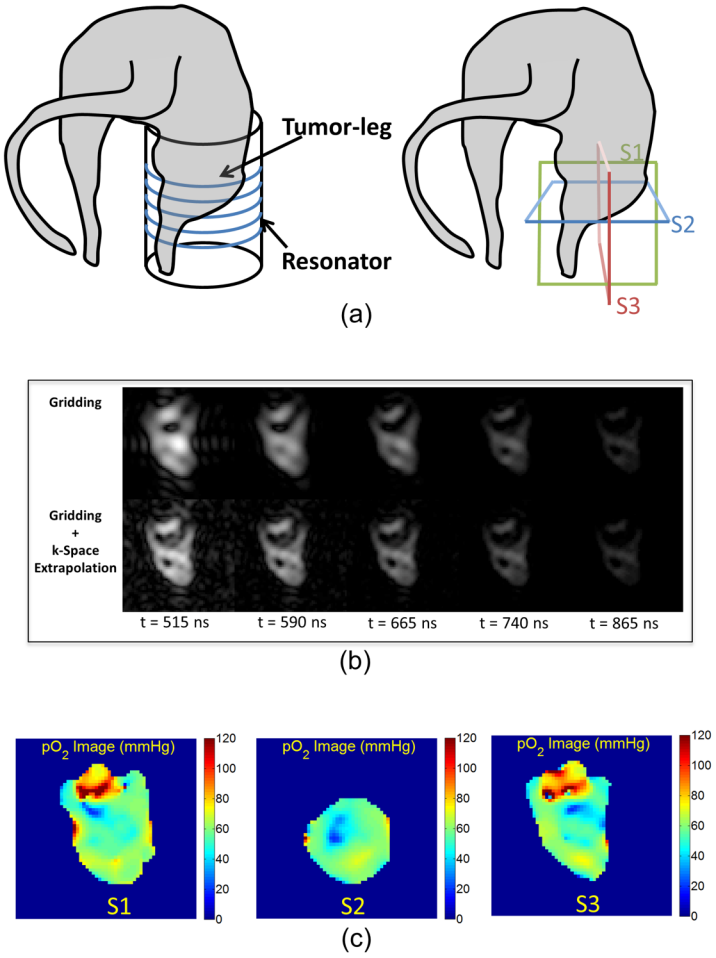

Figure 4. 6. In vivo result. (a) Experimental setup, (b) Reconstructed images shown in log scale, and (c) Estimated pO_2 maps with different slices of anatomy. Note that gridding combined with k-space extrapolation preserves high frequency details even at early time delays comparing to gridding alone in (b). Note that hypoxic region can be localized with the estimated pO_2 maps in (c).

4.3.3 In vivo results

Figure 4.6 (b) shows images reconstructed at different time delays using gridding combined with k-space extrapolation. The k-space extrapolation method maintains Gibbs ringing and more notably preserves the high frequency details in the reconstructed image. The resultant pO_2 maps are shown in Figure 4.6 (c), which are estimated using several slices of reconstructed 3D image as shown in Figure 4.6 (a), with k-space extrapolation. The pO_2 maps enable localization of hypoxic region where SCC tumor cell is embedded. The detected hypoxic region

shows pO_2 near 10 mmHg.

4.4 Discussion

The implementation of our gridding-based k-space extrapolation technique, and other similar techniques using the chirp-z transform[31] have similarities to the keyhole method and time-resolved techniques that have been explored in MRI[54–56]. These techniques use varied approaches to k-space substitution to enable improved image acquisition rate while maintaining voxel resolution. One substantial difference from the method described herein is that such techniques are typically used to image dynamic objects where fully acquiring the data would result in an acquisition time where physiological relevant information might be missed. Here, the early phase encoding delay images depict differences of only hundreds of nanoseconds in the evolution of the EPR signal. Because this range is miniscule with respect to the overall time it takes to acquire an EPR image, there will be no loss in physiologically relevant information in the extrapolated k-space. The only difference is related to T_2*-related signal loss in the extrapolated regions, which is minimized by extrapolating only the temporally neighboring phase encoding time delays. This should not result in blurring as the T_2* times of the EPR tracers have been shown not to be resolution limiting in practice using SPI acquisitions[6].

A substantial advantage of this new method is that it allows quantification of T_2* from a single dataset. Other techniques have used repeated experiments with differing maximum gradient amplitudes (typically 3 different amplitudes are chosen) to secure images with equal FOV at different phase encoding time delay[6,57,58], which usually takes 7.5 minutes to acquire image data with 19x19x19 gradient steps[53]. By using the technique presented herein, temporal resolution can be improved by a factor of 3. Furthermore this new technique allows T_2* to be

calculated over an extended time range, with many data points (120 as performed above), to allow for a more accurate parameter estimation. Because tumor hypoxia is known to fluctuate on 30-60 second time intervals[59–63] this new technique will allow better characterization of hypoxic components of the tumor microenvironment. Conversely, because SPI EPR is limited in temporal resolution as it is a pure phase encoded technique, the improved temporal resolution can be used to improve spatial resolution by factors of 1.7 and 1.4 for 2D and 3D imaging, respectively, for a 3-fold improvement in temporal resolution.

4.5 Conclusion

In this chapter, we described a technique to allow reconstruction of SPI EPR images at a consistent FOV. Further, we implemented a k-space extrapolation approach to demonstrate a new technique for pO_2 quantification method that requires only a single image acquisition. With simulation and tube phantom experiment, we have verified that gridding combined with k-space extrapolation is capable of reliable pO_2 quantification with enhanced temporal resolution (by a factor of 3), which enables higher temporal resolution to resolve pO_2 fluctuations in dynamic EPR imaging or increased spatial resolution with equivalent temporal resolution.

Chapter 5. Accelerated 4D Quantitative Single Point EPR imaging Using Model-based Compressed Sensing

5.1 Introduction

Electron Paramagnetic Resonance Imaging (EPRI) is a non-invasive imaging technique that measures the spatial distribution of unpaired electrons, akin to protons in MRI. Owing to the recent development of biologically compatible spin probes[64–66], EPRI has emerged as a promising non-invasive imaging modality capable of dynamically and quantitatively imaging in vivo tissue oxygenation. However, due to extremely short spin-spin relaxation times, slice-selective imaging and conventional frequency encoding techniques are difficult to achieve and single-point imaging (SPI) techniques are often utilized to improve image quality[6,53]. In single point EPRI (SP-EPRI), gradients remain constant during excitation, and data is acquired immediately after transmit dead time until no signal remains. Thus SP-EPRI is rich in the spectral domain, but inherently suffers from reduced spatial and temporal resolution due to the time needed for a globally phase-encoded acquisition.

SPI also exhibits a "zoom-in" effect due to the use of constant gradients, where k-space samples spread and objects enlarge (as FOV decreases) at increasing phase encoding time delays. Recently, we proposed a method based on gridding termed k-space extrapolation (KSE) to maintain FOV across all phase encoding time delays and to improve the reliability of parameter estimation[10]. Although this method improves temporal resolution (by a factor of 3) by eliminating the need of multiple data acquisitions[7] required to secure multiple images with same FOV, further reduction in acquisition time is needed for SPI. In MRI, a myriad of techniques have been proposed to accelerate imaging, such as parallel imaging[67–69], partial Fourier

reconstruction[70] (also applied to SP-EPRI[71]), and compressed sensing reconstruction[72]. Among them, compressed sensing has recently surfaced as a promising method that can accelerate image acquisition by enabling high ratio of undersampling without a loss of image quality.

Compressed sensing was first introduced in the area of signal processing and information theory[73,74], which was based on the idea that signals can be reconstructed from highly reduced measurements if the signals show sparse representation. Recently, there have been many successful efforts employing compressed sensing to medical imaging[75–79]. Since medical images usually do not show sparse representation by themselves (except some special cases such as angiography), compressed sensing applications benefit from transform domain sparsity that is achieved by transformations such as the discrete wavelet transform (DWT).

Unfortunately, the application of compressed sensing is difficult to employ in SP-EPRI due to its small matrix size that inhibits transform domain sparsity. However, since SP-EPRI acquires abundant data in the parameter domain (measurement of the T_2* decay of the FID) and the T_2* relaxation model is monoexponential and well-known, SP-EPRI can benefit from model-based compressed sensing techniques that simultaneously use k-p-space data in reconstructing images. In such model-based methods, an overcomplete dictionary or principal component analysis (PCA) can be used to sparsify the acquired data and improve T_2* estimation[78,80,81].

In this study, we improved our previous KSE technique to add parameter domain reconstruction and further enhance spatial and temporal resolution in SP-EPRI. The improved, bilateral k-space extrapolation (bi-KSE) allows more sample points to be secured in a target k-space by bilaterally extrapolating k-space samples from the neighboring k-spaces. In addition, a 3 zone sampling strategy was utilized for which a different sampling criterion was applied to

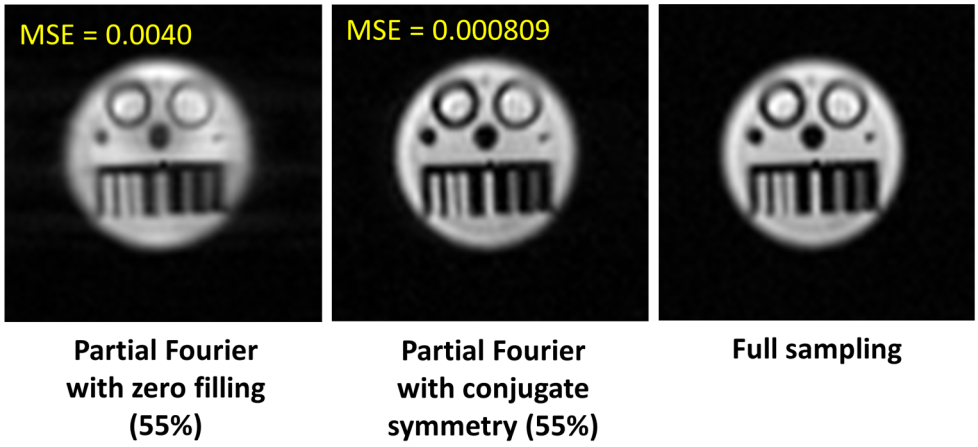

Figure 5. 1. High degrees of partial Fourier sampling with conjugate symmetry can be utilized in SP-EPRI.

each zone while taking advantage of the large degree of conjugate symmetry possible in EPRI. Model-based compressed sensing using PCA[78] was implemented to further improve accuracy of T_2* parameter estimation. During the reconstruction process, aliasing artifacts caused by undersampling are iteratively suppressed by promoting sparsity of PC coefficient maps in the DWT domain.

5.2 Methods

5.2.1 k-Space Sampling Strategy

An incoherent sampling trajectory is a necessary component for sparsity-promoting reconstruction techniques where noise-like aliasing artifacts are desirable. The trajectory used herein utilizes conjugate symmetry and randomized sampling. Owing to pure phase encoding and low B0 field (10 mT), image phase in SP-EPRI is more tractable than in MRI[71]. The reconstructed images in Figure 5.1 show a high degree of conjugate symmetry is possible in SP-EPRI. Therefore, we exploited conjugate symmetry when prescribing randomized sampling patterns by avoiding all symmetric points. Further, we designed a hierarchical random sampling

scheme to effectively maximize the number of k-space samples in an undersampled acquisition.

Figure 5.2 (a) shows an example of the proposed hierarchical random sampling scheme, where k-space is segmented into 3 zones. Zone 1 is a fully sampled central region. Zone 2 is a region where k-space is undersampled by a factor of 2, which is converted to a fully sampled region after the application of conjugate symmetry. This large fully sampled region is required to maximize the performance of model-based compressed sensing explained in later section. Zone 3 is more sparsely sampled than Zone 2. In Zone 2, k-space is uniform randomly sampled, whereas

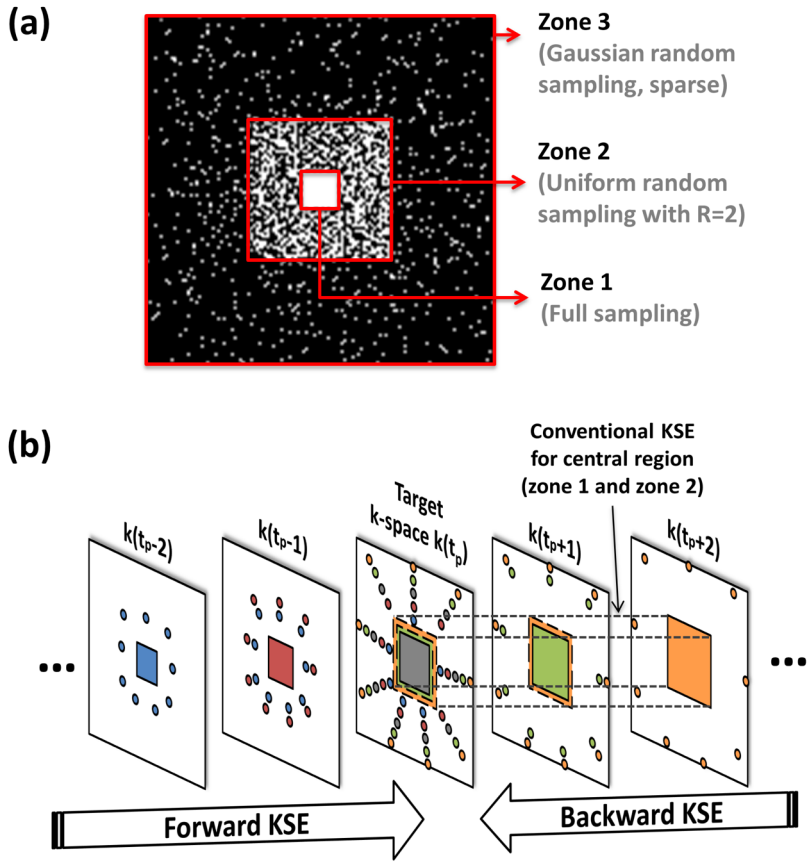

Figure 5. 2. (a) Hierarchical random sampling pattern with 127x127 matrix and R=8, and (b) Concept of bilateral k-space extrapolation (bi-KSE). In (a), sampling positions are first assigned for Zone 1 or Zone 2. Then, sampling positions are sparsely assigned for Zone 3 until the total number of sampling reaches the desired number of points for the prescribed acceleration factor. Zone 2 will be effectively fully sampled after applying conjugate symmetry.

in Zone 3, Gaussian random sampling is applied. After sampling, the sampled points in Zone 2 and Zone 3 are used to estimate the samples at the symmetric position by the application of conjugate symmetry. In this study, 10% of matrix size was used for the width of Zone 1, and the size of Zone 2 was set to 50%, 40%, and 33% respectively for 61x61x61, 95x95x95, and 127x127x127 dataset. 40% of the matrix size was used for the standard deviation of the Gaussian random sampling in Zone 3.

5.2.2 Bilateral k-space extrapolation

We developed a gridding technique for SP-EPRI, called k-space extrapolation (KSE), to achieve equal FOV reconstruction with time-invariant Gibbs ringing and thereby enable more reliable pixelwise T_2* estimation[10]. Unfortunately, this method is not suitable for highly undersampled k-spaces since high frequency regions will be too sparsely sampled and there exist too few samples to be extrapolated from the later phase encoding time delays to earlier delays. Therefore, this method has been improved by performing k-space extrapolation bilaterally as shown in Figure 5.2 (b).

When performing bilateral k-space extrapolation (bi-KSE) with a hierarchical sampling pattern, Zone 1 and Zone 2 do not need bilateral extrapolation since those regions are fully sampled (Zone 2 becomes equivalent to fully sampled after the application of conjugate symmetry). Therefore, Zone 1 and Zone 2 are extrapolated using unilateral/backwards KSE, while Zone 3 is extrapolated bilaterally as described in Figure 5.2 (b). The extrapolated k-space samples need to be scaled to harmonize with the target k-space, compensating for T_2* decay. This scaling factor can be approximated by simply referring to the center of k-space. However, when performing k-space extrapolation within the central region (low spatial frequencies), small errors in the estimated scaling factors can lead to severe distortion in image reconstruction and

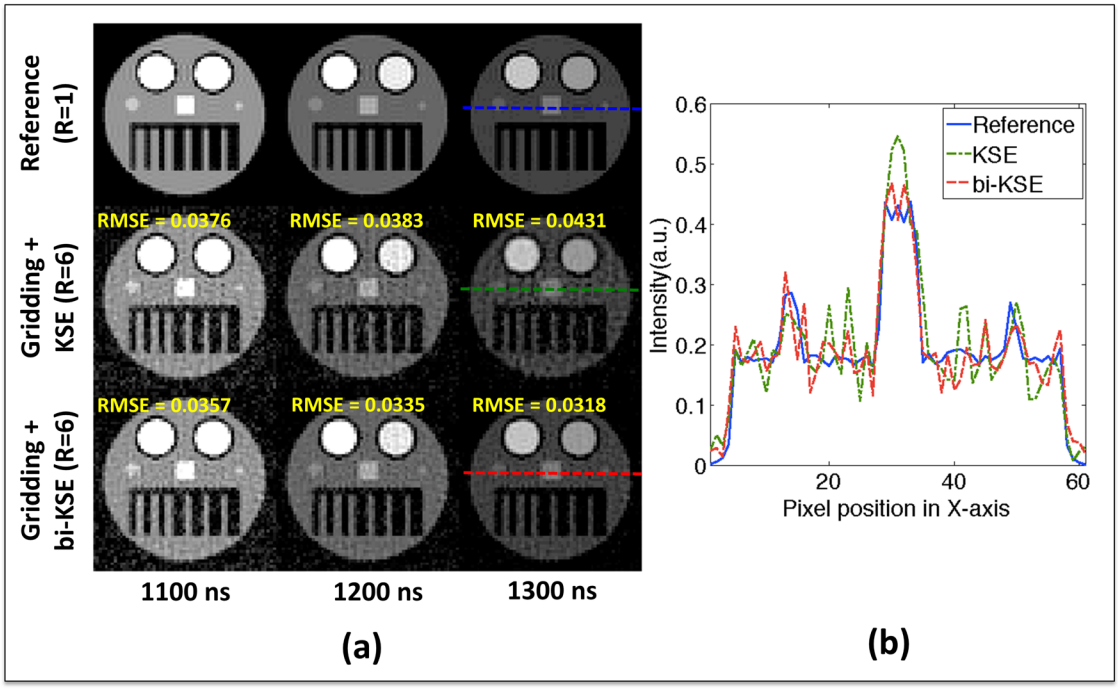

Figure 5. 3. (a) Images reconstructed from undersampled k-space (R=6, 61x61 2D digital phantom, data reconstructed over time range [900 ns, 1300 ns]) using gridding with KSE or gridding with bi-KSE, and (b) 1D profiles at y=29 (along the dotted line) at t_p = 1300 ns.

parameter estimation. To address this issue, the scaling factor is refined iteratively so that the Gibbs ringing pattern of the extrapolated image becomes similar with the reference image (the one with the highest bandwidth). To evaluate the similarity between two images, the numerical gradient of the images were used where gradient values near strong edges were discounted to purely consider changes resulting from Gibbs ringing. The numerical gradient images were obtained using the central differencing scheme[82]. The scaling factor was adjusted by evaluating the error function that is the l_1-norm of error between the target and reference gradient image, using the Nelder-Mead simplex search algorithm as implemented by MATLAB (The Mathworks, Inc., Natick, MA).

After bilateral k-space extrapolation, equal FOV images are reconstructed by applying convolution gridding[45,46]. Iterative density correction was used before gridding[83], which is an

indispensable process for reliable quantification, because spatial sampling density changes at each reconstructed time delay. As the reconstructed images show in Figure 5.3 (a), bi-KSE dramatically improves the quality of images reconstructed with undersampled k-spaces, especially for images at later time delays (1300 ns) where reconstruction error is greatly reduced (Figure 5.3 (b)). The proposed bi-KSE method dramatically increases available k-space samples (74,379 vs 1,191 at 1300 ns for bilateral and unilateral k-space extrapolation, respectively) and provides improved image quality compared to previous techniques. However, not all reconstruction error is removed. Therefore, we employed PCA-based reconstruction to exploit the rich spectral domain of the SP-EPRI dataset to further improve image quality and resulting T_2* estimation, as explained below.

5.2.3 Model-based compressed sensing

To evaluate compressed sensing reconstruction in highly undersampled SP-EPRI, we have utilized PCA-constrained reconstruction[78]. In PCA-based reconstruction, a training matrix whose columns consist of training data, which consist of time series for all possible FID signals, are used to obtain principal components. The eigenvectors or singular vectors obtained from the training matrix (by using eigenvalue decomposition or singular value decomposition) will span the signal subspace where true FID signals exist.

The training data is generated within a predefined T_2* range and is a factor that affects the performance of PCA-based reconstruction. Utilizing a T_2* range that does not encompass the T_2*'s of targeted objects may result in a false signal space. In hypoxia imaging EPRI, the T_2*'s of Oxo-63 are distributed within a small range, approximately 400-650 ns corresponding to a dissolved oxygen level between 5% and 0%, respectively. To encompass all possible oxygen levels (0-100%), a T_2* range of [1ns, 700ns] was used in this study.

With the estimated T_2* range [p,q] (p<q), a training matrix can be composed using the independent monoexponential curves as equation 5.1.

$$D = \begin{bmatrix} e^{-\frac{t_1}{p}} & e^{-\frac{t_1}{p+1}} & \cdots & e^{-\frac{t_1}{q}} \\ \vdots & & \ddots & \vdots \\ e^{-\frac{t_{T-1}}{p}} & e^{-\frac{t_{T-1}}{p+1}} & \cdots & e^{-\frac{t_{T-1}}{q}} \\ e^{-\frac{t_T}{p}} & e^{-\frac{t_T}{p+1}} & & e^{-\frac{t_T}{q}} \end{bmatrix} \quad (5.1)$$

Then, D is decomposed by SVD to yield singular vectors, and L significant singular vectors (L=3 or 4 was used in this study) are selected to compose matrix $\hat{B}$. PC coefficient matrix M can be obtained by equation 5.2, whose n-th column vector represents PC coefficient map corresponding to n-th PC.

$$M = I\hat{B} = \begin{bmatrix} I_{1,1} & I_{1,2} & \cdots & I_{1,T} \\ I_{2,1} & I_{2,2} & & I_{2,T} \\ \vdots & & \ddots & \vdots \\ I_{N-1,1} & I_{N-1,2} & \cdots & I_{N-1,T} \\ I_{N,1} & I_{N,2} & & I_{N,T} \end{bmatrix} \begin{bmatrix} B_{1,1} & B_{1,2} & \cdots & B_{1,L} \\ B_{2,1} & B_{2,2} & & B_{2,L} \\ \vdots & & \ddots & \vdots \\ B_{T-1,1} & B_{T-1,2} & \cdots & B_{T-1,L} \\ B_{T,1} & B_{T,2} & & B_{T,L} \end{bmatrix} \quad (5.2)$$

, where I is an image matrix containing vectorized initial images, T is the number of images, and N is the length of image vector. Now, the model-based compressed sensing problem can be formulated by the following equation:

$$\widehat{M} = argmin_M \left\{ \sum_{j=1}^{T} \left\| FT_j\left(M\hat{B}^T\right) - \overrightarrow{K_j} \right\|_2^2 + \sum_{i=1}^{L} \lambda_i P_i(M) \right\} \quad (5.3)$$

,where FTj denotes the operator for discrete Fourier transform with image at time delay j, $\overrightarrow{K_j}$ is measured k-space vector at time delay j, $P_i(M)$ is penalty based on discrete wavelet transform (Daubechies 4, Wavelet Toolbox in MATLAB 2011b) and total variation[84] of PC coefficient maps, and λ_i is the Lagrange multiplier that is selected differently with each PC coefficient map.

The penalty term is calculated as in equation 5.4:

$$P_i(M) = \|\psi(M_i)\|_1 + \alpha\, TV(M_i) \tag{5.4}$$

, where ψ is a DWT transform, TV is total variation, M_i is i-th PC coefficient map, and α is tuning constant between two objectives.

In equation 5.3, the first and the second summation term in the brace represent data fidelity and penalties respectively. In practice, calculation of the data consistency term requires significant computational power due to repeated gridding and inverse gridding steps (to deal with non-Cartesian k-space samples accumulated by bi-KSE), especially when dealing with large numbers of samples in 3D imaging. To improve the speed of reconstruction, we enforced data fidelity in the image domain rather than in the k-space domain as the following equation shows:

$$\widehat{M} = argmin_M \left\{ \sum_{j=1}^{T} \left\| \left(M\hat{B}^T\right)_j - \vec{I_J} \right\|_2^2 + \sum_{i=1}^{L} \lambda_i P_i(M) \right\} \tag{5.5}$$

, where $\left(M\hat{B}^T\right)_j$ and $\vec{I_J}$ denote j-th column vector in respectively updated and initial image matrix. This approximation is possible owing to the hierarchical random sampling pattern which provides good quality image reconstruction after the application of bilateral k-space extrapolation (as seen in Figure 5.3 and Figure 5.6 (g)). In experiments not presented herein, image-based consistency performed as well as conventional k-space methods, likely due to the strong performance of bi-KSE alone for undersampled acquisitions.

This optimization problem was solved using the nonlinear Polak-Ribiere Conjugate Gradient algorithm initiated with steepest gradient and backtracking line search with contraction factor 0.4. Once the PC coefficient maps are optimized, the image sequence can be reconstructed by performing a linear combination of PC coefficient maps and PC vectors as equation 5.6.

$$\hat{I} = \hat{M}\,\hat{B}^T \tag{5.6}$$

In this method, the image sequences were normalized by the maximum value of the initial image in the sequence. By doing this, we were able to limit the effective range for parameter setting (α, λ_1, λ_2, λ_3, and λ_4), which can be generally applied in different experiments without dependence on any scaling factors between datasets. The effective parameter ranges $0.1 \leq \alpha \leq 1.0$, and $0.1s_k \leq \lambda_k \leq 0.5s_k$ were empirically found and used, where $(s_k)_{k=1}^4 = (1, 2, 5, 10)$ for the k-th PC coefficient map. The selected λ_k is then scaled by $\|M_k\|/\|M_1\|$ to compensate for the scale difference between PC coefficient maps. Note that larger λ_k is used for the less significant PCs that commonly contain more noisy data. By using larger λ_k we can promote sparsity and smoothness in the corresponding PC coefficient map and thereby suppress noise more effectively.

5.2.4 Simulation

To evaluate the capability of the proposed method for T_2* estimation with undersampled k-space, a computer simulation and a phantom experiment using SP-EPRI were performed. For the computer simulation using MATLAB (The Mathworks, Natick, MA), synthesized SP-EPRI images with much higher resolution (187x187x187) than conventional acquisitions (e.g., 19x19x19) were generated based on the 3D T_2* map shown in Figure 5.7 (a). From the 3D T_2* map, FID curves were simulated from 1ns to 1800ns using a sampling rate of 5ns and a dead time of 300ns. To simulate SPI encoding, inverse gridding was used to sample k-space with a 61x61x61, 95x95x95 or 127x127x127 matrix with a spreading Dirac comb function to simulate the zoom-in effect due to constant gradients. For 2D phantom experiments, only the central slice of the phantom was used.

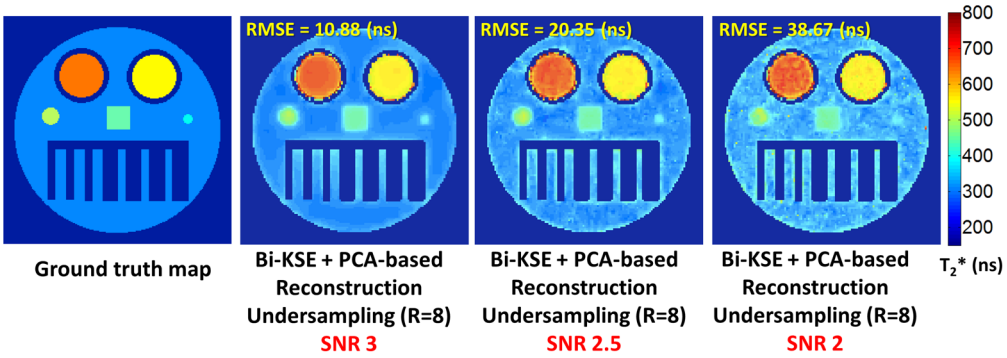

Figure 5. 4. Critical SNR. 8-fold undersampled data was used for reconstruction (127x127 matrix). SNR was iteratively tuned by adjusting noise level to achieve the targeted SNR before performing undersampling. For these experimental conditions, an SNR of 3 is the minimum for acceptable quality reconstruction.

5.2.4.1 Simulation - undersampling vs. reduced Averaging

The voxel size for the proposed acquisitions is 25~220x smaller than previous SP-EPRI acquisitions, which results in a large reduction in SNR. Even for conventional resolutions, a large number of averages (1000~8000) is typically applied in SP-EPRI to improve SNR. Therefore, it may be also possible to accelerate imaging by simply reducing the number of averages rather than undersampling k-space; however, this is not expected to perform well due to the already low SNR of the data. To verify this, a simulation was performed to compare the proposed undersampled k-space acquisition to reduced average data, with and without the proposed PCA-constrained reconstruction. The reduced average method was simulated by adjusting noise levels to decrease SNR by a factor of $\sqrt{R}$ (R: acceleration factor attained by reducing average). A 127x127 2D digital phantom was generated as explained above to simulate comparable undersampled and reduced averaging datasets with R=8.

The 2D simulation was performed at the critical SNR limit for the proposed method, where critical SNR is the lower SNR limit in the region of shortest T_2* at time delay 1300 ns that still enables reasonable parameter estimation. For these experimental conditions, this was

determined to be approximately 3, as shown in Figure 5.4. Simulated data with an SNR of 3 was undersampled with R=8 and processed by the proposed method explained in the above sections. For the reduced average method with R=8, the SNR was reduced by a factor of $\sqrt{8}$ (SNR=1.06), and then the data were fully-sampled. The sampled k-spaces were processed with the conventional unilateral KSE and PCA-based reconstruction. 101 consecutive k-spaces from 800ns to 1300ns were used for reconstruction.

5.2.4.2 Simulation - resolution and acceleration

The fully sampled k-spaces were retrospectively undersampled with different acceleration factors (R) by using the hierarchical random sampling explained in the above section. The data were generated with low SNRs to highlight the performance of the proposed method (5 for 127x127x127, 7 for 95x95x95, and 9 for 61x61x61 k-spaces, when measured at 1100 ns). Data were acquired at R=1, 4, 6, 8 for 61x61x61 k-space; R=8, 12, 15 for 95x95x95; R=15, 30, 60 for 127x127x127 k-space.

5.2.5 Phantom experiment

Details regarding the specifications of the EPRI spectrometer have been previously published[2,53]. For the tube phantom experiment, 3D EPR data was obtained using three-tube phantom comprised of three tubes containing 2 mM Oxo-63 (GE Healthcare, Waukesha, WI) bubbled with 0%, 2% and 5% oxygen, respectively. Data was encoded using three orthogonal phase-encoding gradients incrementally ramping in 61 equal steps from –40 to 40 mTm^{-1}, resulting in 61x61x61 phase-encoding steps. 581 data points were encoded with a sampling period of 5ns after the minimum RF recovery dead time (530 ns). 8000 averages per phase encoding point and an interpulse delay (TR) of 10 μs was used. A total of 28,373 points (approximately 8-fold undersampling) with a 61x61x61 matrix size were phase-encoded using

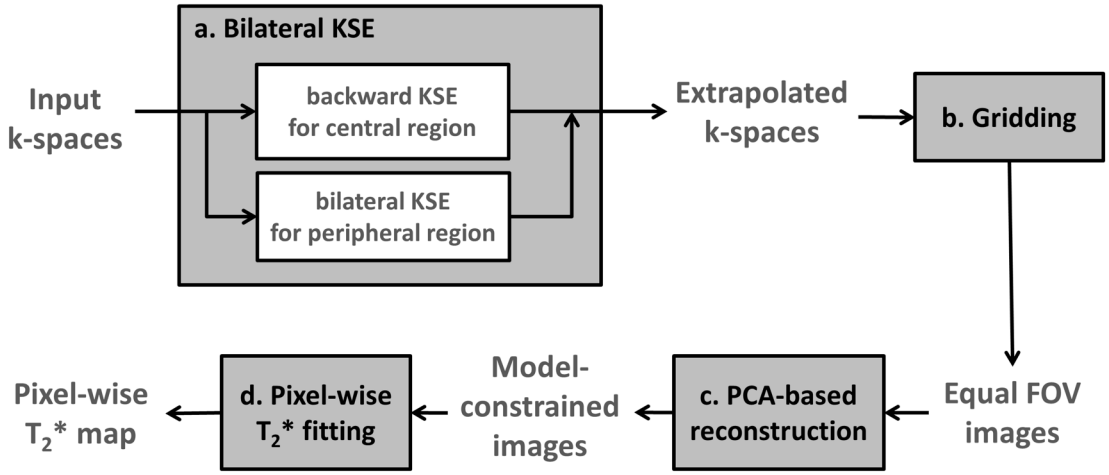

Figure 5. 5. Data processing flowchart. (a) Bilateral k-space (bi-KSE) extrapolation, (b) gridding, (c) PCA-based reconstruction, and (d) pixelwise T_2* fitting.

the hierarchical random sampling strategy.

5.2.6 Data Processing

Bi-KSE was performed in the peripheral region (Zone 3), and unilateral/backwards KSE was independently performed in the central region (Zone 1 and Zone 2) in a reversely cascading manner, as depicted in Figure 5.5 (a). The extrapolated k-spaces from each phase encoding time delay were individually gridded into Cartesian k-space to generate equal FOV images (Figure 5.5 (b)). Then, these images were used as input to the PCA-based reconstruction (Figure 5.5 (c)). With a sequence of final images reconstructed by using above-explained methods, T_2* was fit using a traditional T_2* relaxation model for the magnitude of pixelwise transverse magnetization (Figure 5.5 (d)). Linear least-square curve fitting was applied to the log-linearized FID curve in which the slope and the y-intercept represent respectively $-1/T_2$* and $\log(M_0)$.

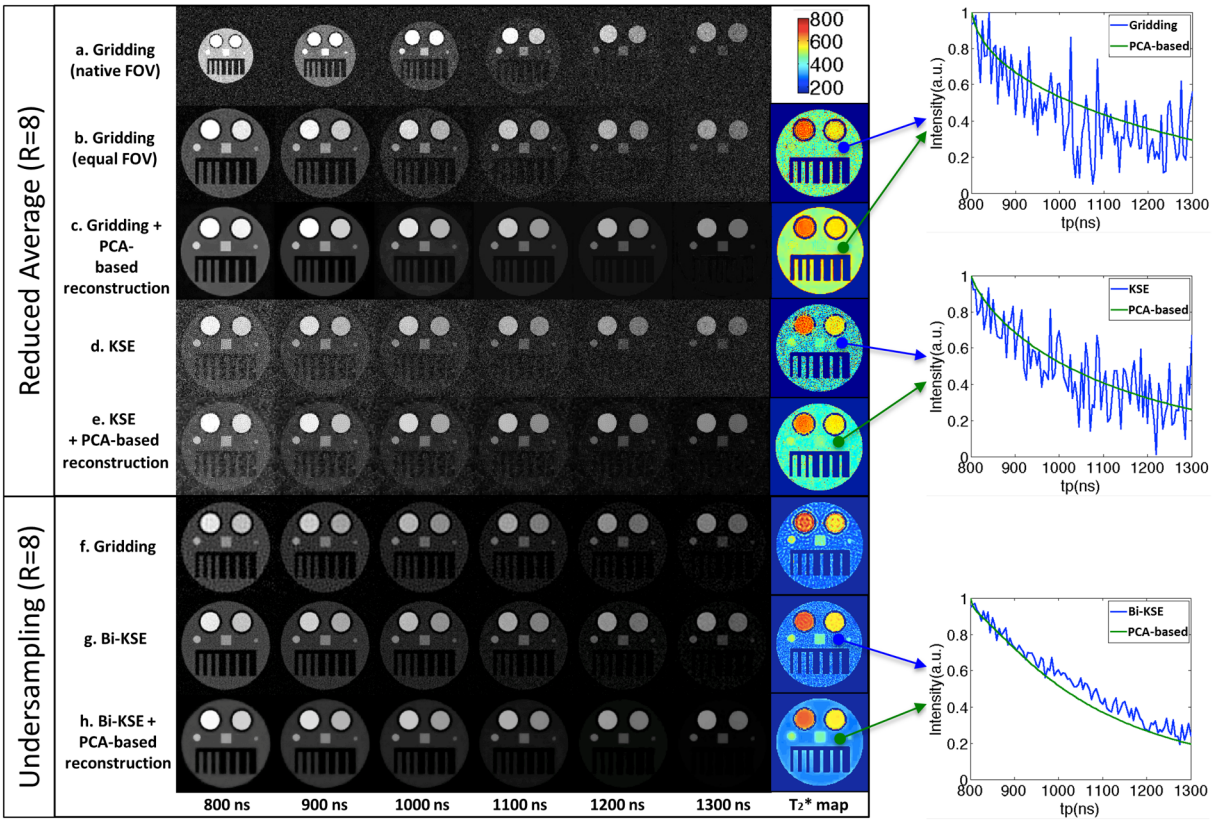

Figure 5. 6. Reduced average vs. undersampling acquisition. (a) Images reconstructed with native FOV (reduced average), (b) equal FOV images with gridding only (reduced average), (c) equal FOV images with gridding and PCA-based reconstruction (reduced average), (d) equal FOV images with unilateral KSE (reduced average), (e) equal FOV images with unilateral KSE and PCA-based reconstruction (reduced average), (f) equal FOV images with gridding only (undersampling), (g) equal FOV images with bi-KSE (undersampling), and (h) equal FOV images with bi-KSE and PCA-based reconstruction (undersampling). 127x127 2D data with initial SNR of 3 was simulated, and then reduced average or undersampling was applied to obtain 8-fold acceleration. In (d), high noise in the later images are propagated to the earlier by the KSE process. Note that in the results with reduced average T_2* estimates are biased due to the severe noise resulting from reduced averages. The PCA-based reconstruction method using undersampling (h) provides the best performance.

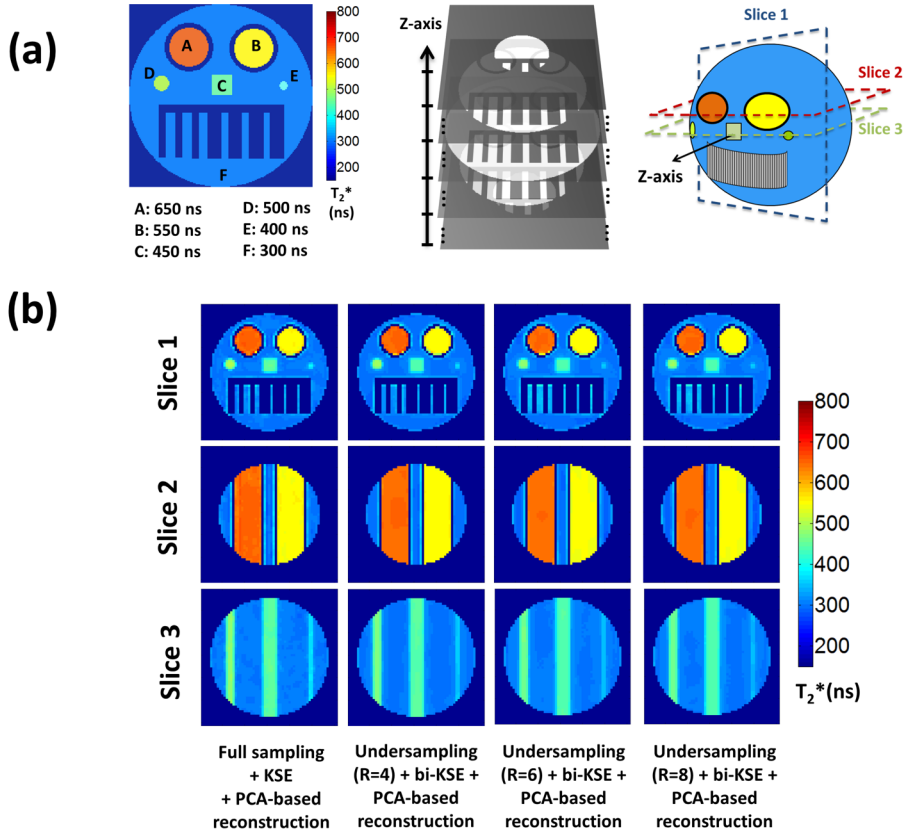

Figure 5. 7. Simulation result with 61x61x61 dataset. (a) Center slice of ground truth T_2* map (left), composition of 3D T_2* map (middle), and slice location (right), and (b) estimated T_2* maps. Note that the estimated T_2* map is still accurate with 8x acceleration although the detail in small region E was slightly lost.

	Segment	A	B	C	D	E	F
R = 8	mean (ns)	646.92	549.89	441.69	492.76	369.05	302.77
	standard deviation (ns)	2.45	2.19	5.4612	0.98	2.58	8.04
	RMSE (ns)	3.93	2.19	9.94	7.30	31.06	8.50
R = 6	mean (ns)	647.27	549.59	442.97	493.15	366.94	302.04
	standard deviation (ns)	2.35	1.94	5.65	3.36	2.69	7.91
	RMSE (ns)	3.60	1.98	9.01	7.62	33.16	8.17
R = 4	mean (ns)	645.72	549.23	443.95	491.89	365.97	301.77
	standard deviation (ns)	2.10	1.33	3.69	1.40	1.35	6.91
	RMSE (ns)	4.76	1.54	7.08	8.23	34.06	7.13
R = 1	mean (ns)	649.19	550.04	448.82	500.07	383.37	302.13
	standard deviation (ns)	5.54	3.53	4.83	3.36	2.45	6.41
	RMSE (ns)	5.60	3.53	4.97	3.35	16.81	6.75

Table 5. 1. Quantitative result of estimated T_2* for various acceleration factors with 61x61x61 matrix size. The result was evaluated with mean, standard deviation, and root mean square error (RMSE) within each segment. Note that the result shows error of 1% to 2% for the segment A, B, C, D, and F, whereas it shows relatively higher error (around 10%) in segment E. Refer to Figure 7-a for the labeling and corresponding regions.

5.3 Results

5.3.1 Simulation Results – Undersampling vs. Reduced Averaging

The reconstructed images and the resultant T_2* maps obtained using reduced average or undersampling are shown in Figure 5.6. Reconstructions with gridding are shown in 5.6(a), 5.6(b), 5.6(c) for reduced average data, and 5.6(f) for undersampled data. KSE is applied to the reduced average data in 5.6(d) and 5.6(e), and bi-KSE is applied to the undersampled data in 5.6(g) and 5.6(h). PCA-based reconstruction is applied to the reduced average data in 5.6(c) and 5.6(e), and to the undersampled data in 5.6(h). As seen in the reconstructed images and the resulting estimated T_2* maps, undersampling (5.6(h)) outperforms reduced averaging (5.6(c) and 5.6(e)).

5.3.2 Simulation Results – Resolution and Acceleration

To evaluate how accurately the proposed method estimates T_2* with undersampled k-space data, we performed computer simulations using synthesized 3D data consisting of various T_2*'s (Figure 5.7 (a)). In addition to the proposed method, a conventional k-space extrapolation method with full sampling (R=1) was also implemented for comparison. 81 consecutive k-spaces from 700 ns to 1100 ns with a 5 ns time interval were used for reconstruction. Figure 5.7 (b) shows the estimated T_2* maps obtained using undersampled k-spaces with 61x61x61 gradient steps with acceleration factors of R=1, 4, 6, and 8. Table 5.1 shows the corresponding quantitative result. Our method enabled accurate T_2* estimation up to 8-fold acceleration at this matrix size. However, the small segment E tends to be blurred due to the large voxel size. Figure 5.8 depicts how the proposed method works with larger matrix sizes. As seen, when higher matrix size is used, the overall performance of our method tends to be improved at the same acceleration factor (R=8) due to the larger central region and higher expected transform sparsity.

Moreover, good quality T_2* estimation with even higher acceleration factors (R=15 for a 95x95x95 k-space, and R=30 for a 127x127x127 k-space) is attainable.

5.3.3 Phantom Experiment Results

Figure 5.9 shows the T_2* map estimated from prospectively undersampled k-spaces (R=8). 91 consecutive k-spaces from 1530 ns to 1980 ns with a 5 ns time interval were used for reconstruction. As seen in Figure 5.9, the proposed method enables reliable parameter estimation with reduced sampling. The estimate was 684.45 ± 39.10 ns, 659.79 ± 31.11 ns, and 591.10 ± 25.52 ns for tube bubbled with 0%, 2%, and 5% oxygen, respectively, which lie within the our expected range. The estimated numbers show 4%-6% standard deviation, which is presumably due to the system noise in the current EPR scanner. Fitted %oxygen-R_2* curve showed slope of 4.68×10^{-5} (ns^{-1} $\%oxygen^{-1}$) and y-intercept of 1.45x10-3 (ns^{-1}) with R_2=0.9662.

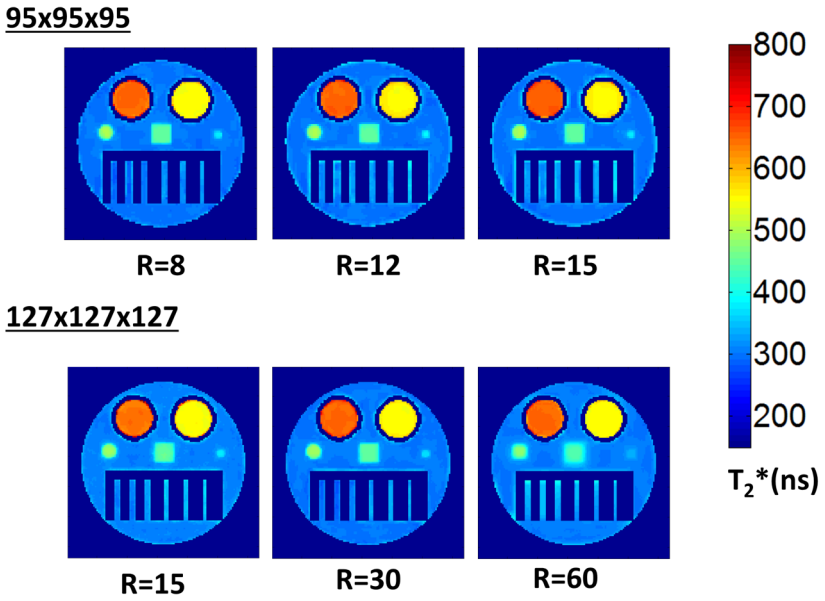

Figure 5. 8. Quantitative results with higher matrix sizes. Note that higher matrix size enables higher acceleration factors.

5.4 Discussion and Conclusions

The proposed reconstruction method allows significant improvement in the spatial resolution of single point EPRI. For example, if we acquire data with 61x61x61 gradient steps, the full sampling scheme will require a scanning time of approximately 75.7 min (226,981 points x 2,000 averages x 10 μs TR), whereas 8-fold undersampling will enable imaging within approximately 9.5 min (28,373 points). Compared to methods that require multiple gradient acquisitions (typically 3), the proposed technique represents a 24-fold increase in temporal resolution. When using higher matrix size, we were able to achieve higher acceleration factors, for example R=15 with 95x95x95 or R=30 with 127x127x127 gradient steps. Nonetheless, these larger matrix sizes may not be realistic for SP-EPRI since a large number of sampled points are still required, for example 57,158 points and 68,279 points to achieve R=15 with 95x95x95 and

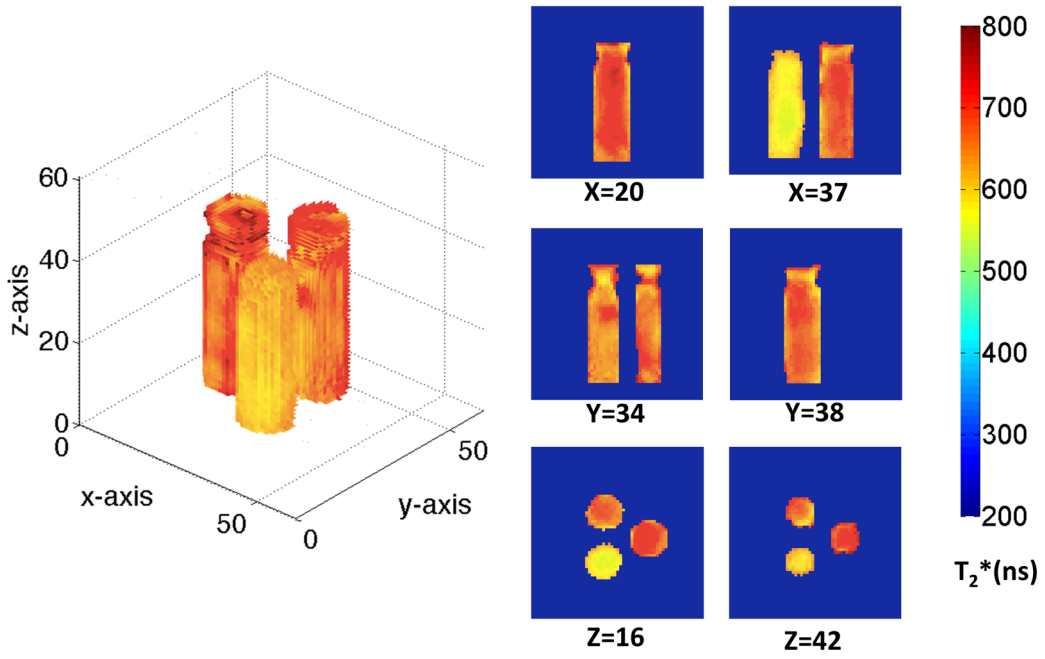

Figure 5. 9. Estimated T_2* map in imaging experiment of three tubes of 2 mM Oxo-63 bubbled with 0%, 2%, and 5% oxygen. Prospectively undersampled (R=8) k-spaces from 1530ns to 1980ns were used for reconstruction. The estimated T_2* in each tube is quite homogeneous for the 0% (684.45 ± 39.10 ns), 2% (659.79 ± 31.11 ns), and 5% (591.10 ± 25.52 ns) tubes.

R=30 with 127x127x127 matrix size, respectively, which are equivalent to 19.1 min and 22.8 min of scanning time. Such scans might also operate at unrealistic signal to noise levels, despite our methods strong performance with low SNR data (SNRs of 5 for 127x127x127, 7 for 95x95x95, and 9 for 61x61x61 k-spaces, when measured at 1100 ns were utilized). Therefore, choosing a lower resolution (61x61x61) and moderate acceleration (R=8) enables reasonable scanning time (<10 min) but also achieves high spatial resolution to localize hypoxic tissues. However, with the addition of other complimentary fast imaging techniques, such as parallel imaging, further improvements may allow higher resolution image will be able to be obtained within reasonable scanning time, well within the probe clearance time. Improvements in SNR will be aided by the development of phased-array coils[85].

It is not unexpected that undersampling performs better than reduced averaging in SP-EPRI. In our proposed method, the large central region is secured with a hierarchical random sampling pattern, where the sampled k-space is acquired with a higher SNR than full sampling would allow. Even though PCA-constrained reconstruction is applied to both sampling methods, when the SNR falls below a critical threshold noise (and aliasing) is unable to be separated. By applying undersampled acquisitions we can trade recoverable aliasing for improved SNR[75]. Note that our simulations comparing reduced averaging to undersampled acquisitions were performed with R=8. For higher acceleration factors, it is not controversial to expect even greater improvements for undersampled acquisitions compared to reduced averaging. Finally, because the KSE techniques propagate k-space points from the periphery of k-space, they perform poorly in instances of low SNR (Figure 5.6 (d) and (e)). This is also not unexpected due to low signal levels in the periphery of k-space with a higher noise floor in the case of reduced averaging.

In this chapter, we have explored the methods to accelerate EPR imaging without loss of

accuracy in the T_2*/oxygen quantification. To secure k-space samples as many as possible we have developed the bi-KSE method. Moreover, the model-based compressed sensing using PCA has been adapted to further improve the accuracy of T_2* estimation. With a computer simulation and phantom experiment, we have verified that the proposed methods enable significant acceleration (8-fold, 15-fold, and 30-fold accelerations respectively for 61x61x61, 95x95x95, and 127x127x127 gradient steps), which realizes more reasonable scan time and higher spatial resolution in the current SP-EPRI system.

Chapter 6. A Rapid and Robust Gradient Measurement Technique Using Dynamic Single Point Imaging

6.1 Introduction

The gradient system is an essential component in modern clinical MR imaging. It performs temporal-spatial encoding of transverse magnetization through a spatially varying magnetic field. Gradient waveforms can be synthesized to perform a range of image encoding strategies including conventional Cartesian image encoding, as well as non-Cartesian acquisitions such as radial[3] and spiral[86] imaging. Unfortunately, there still exist many factors that inevitably cause distortions in the realized gradient magnetic field: eddy currents[87–90], imperfection induced by the power amplifier, and mechanical/thermal vibrations[91,92]. Due to these undesired distortions, it is challenging in practice to realize the actual gradient field exactly as prescribed, which, if the prescribed gradient is assumed during reconstruction, can result in image artifacts (e.g., blurring, ringing, or phase error). This can be a critical issue in non-Cartesian acquisitions, and is further exacerbated in acquisition schemes with a long readout duration such as spiral or echo planar imaging (EPI)[93,94]. In these cases, the k-space trajectory is prone to deviate from that prescribed due to accumulated error in the phase evolution resulting from the distorted gradient.

Methods to estimate the actual gradient shape and the resultant k-space trajectory have been previously presented in the MR literature, and can be classified as follows: Imaging based gradient measurement (IGM) and magnetic field monitoring (MFM). In IGM, a (typically) 1D imaging technique based on a specialized pulse sequence is exploited to measure the gradient shape. In MFM, several NMR-based field probes are placed inside the magnet bore and used to

record field characteristics temporally and spatially [95–98]. While this provides the most direct measurement of the gradient field, the use of additional external hardware adds complication and expense.

According to the methodology of data acquisition, IGM methods can be further classified into two categories: frequency encoding based gradient measurement (FGM) and phase encoding based gradient measurement (PGM). In FGM[99], off-centered selection of a thin slice is performed to the avoid signal dephasing effect caused by gradient, followed by measurement of the phase evolution over encoding time in the manner of frequency encoding. Although the efficacy of this measurement scheme has been verified in many critical studies[100,101], there still exist limitations such as the dependency on slice selection and T_2* decay. Alternatively, in previously proposed PGM methods[29,35,36,102], the phase evolution is measured at a constant (and single) echo time after a RF pulse, which is advantageous in terms of reducing the impact of T_2* decay. However, a series of RF pulses must be applied to measure the whole gradient, which requires extensive measurement times.

Once the gradient has been characterized, it can be used directly in image reconstruction to improve image quality. However, such a measurement is specific to the characterized gradient and pulse sequence parameters and is not typically generalizable to other acquisitions. To enable more accurate output waveforms, it is routine in current generation MR systems to perform pre-emphasis correction by inputting a filtered (or intentionally distorted) waveform into the gradient subsystem[103]. Such methods rely on the assumption that gradient systems are generally characterizable as linear time invariant (LTI) systems[104]. Unfortunately, these system-level corrections do not realize sufficiently accurate waveforms, which may necessitate the further use of the gradient measurement techniques described above. Thus, a more generalizable approach to

gradient measurement is to utilize these techniques and the LTI concept to compute a gradient impulse response function (GIRF). This approach allows estimation of the distorted gradient shape instead of directly measuring the realized gradient. By acquiring a comprehensive measurement of the gradient (e.g., obtained from one of the methods described above), the GIRF can be determined as a unique finite impulse response filter, and then any gradient shape realized in the same gradient system can be analytically predicted by convolving an estimated GIRF with the prescribed gradient [105–107].

In this study, we have developed a new gradient measurement method utilizing 1D dynamic single point imaging (SPI)[5] performed across a range of phase encoding time delays, which does not require slice selection, additional equipment, or knowledge about the imaged subject. The field of view (FOV) in SPI changes over phase encoding time delay, exhibiting a variable FOV property under an applied gradient. In the proposed gradient measurement method, 1D SPI encoding is implemented in each gradient axis by linearly scaling the amplitude of a tested gradient with each TR (i.e., from -1x to +1x to implement phase encoding). Then, the FOV scaling factors between different phase encoding time delays are estimated by using k-space or image domain representations of the 1D SPI data. The FOV scaling factors represent relative encoding positions in k-space between two phase encoding time delays, and the 1st derivative of FOV scaling factors represents relative amplitude in the measured gradient. This measured k-space trajectory can then be utilized in reconstruction to improve image quality.

Three gradient-intensive sequences (ultrashort time echo (UTE) [3], spiral, and multi-echo bipolar gradient echo (GRE)) were tested to evaluate the efficacy of the new SPI-based gradient measurement scheme. In UTE, a center-out radial acquisition is used to minimize the achievable echo time and enable contrast for species with ultrashort T_2*'s. In spiral imaging, the gradient

waveforms are simultaneously designed to operate within the peak gradient slew rate and peak gradient amplitude limits. Finally, multi-echo bipolar GRE with ramp sampling for more robust reconstruction in quantitative fat-water imaging is demonstrated. GIRFs were also estimated using the proposed method, and applied to obtain an estimated k-space trajectory in UTE, spiral, and multi-echo bipolar GRE imaging.

6.2 Methods

6.2.1 Theory

The proposed method is based on assumption that gradient distortion is a LTI function of the gradient input [104]. In the proposed technique, 1D dynamic SPI is performed by linearly scaling with N_p steps (-1x to 1x) the entire gradient waveform along a single axis to obtain N_px1 data. Note that dynamic SPI differs from conventional SPI approaches where multiple k-spaces are continuously acquired with a prescribed sampling rate while phase encoding gradients are on.[10,12,31] Figure 6.1 (a) shows an example of a trapezoidal readout gradient to be measured, and Figure 6.1 (b) shows the corresponding dynamic SPI encoding gradient used for the proposed calibration technique. The FOV at phase encoding time delay (t_p, the elapsed time after RF excitation) in dynamic SPI is determined by the following equation[6,7,10]:

$$FOV(t_p) = \frac{\pi N_p}{\gamma \int_0^{t_p} G(\tau) d\tau} \tag{6.1}$$

, where N_p is the number of phase encoding steps, γ is a gyromagnetic ratio, and $G(\tau)$ is an amplitude of maximum phase encoding gradient at time delay τ, for example, which is the trapezoidal gradient with solid line in Figure 6.1(b). Figure 6.1(c) shows the RF pulse and data acquisition window. Note that in dynamic SPI, multiple images can be acquired at every ΔTs (sampling interval) which improves sampling efficiency over conventional SPI approaches. Figure 6.1(d) shows how the SPI sampling trajectory changes, exhibiting a time-decreasing FOV. The minimum N_p can be determined by the required FOV (typically larger than the

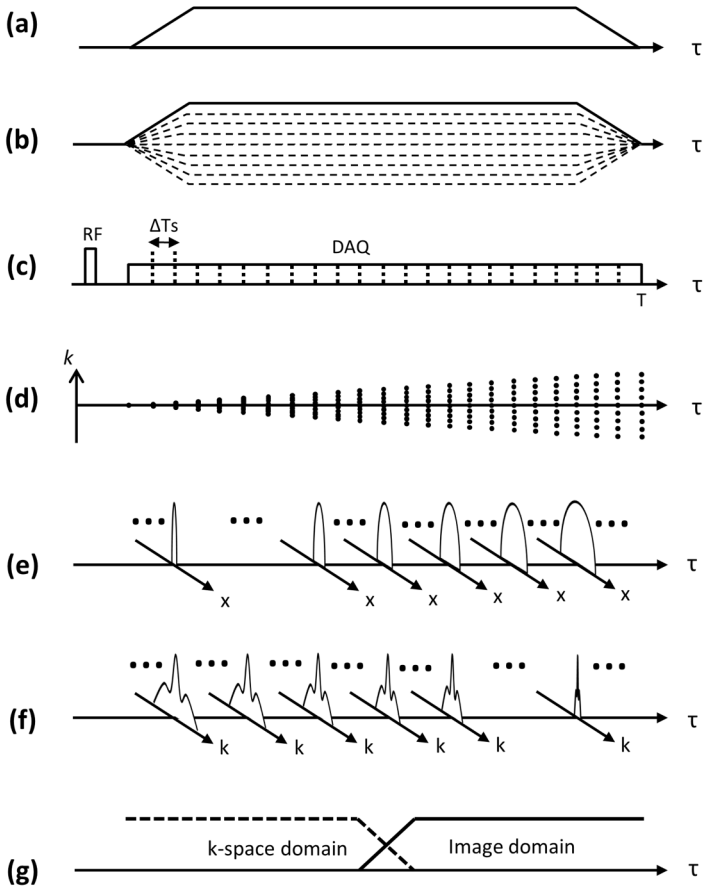

Figure 6. 1. 1D dynamic SPI acquisition for gradient measurement. An example of (a) targeted gradient, (b) the corresponding SPI encoding gradient, (c) RF transmission and data acquisition, (d) k-space trajectory, (e) image domain SPI data, (f) k-space domain SPI data, and (g) merging filter. 1D SPI sampling can be implemented by simple linear scaling the gradient amplitude with each TR. Note that the FOV change directly reflects the gradient shape. The image or k-space domain data can be adaptively used for FOV scaling search, according to the FOV at encoding time.

diameter of imaged subject to avoid aliasing), fov_R, and gradient amplitude, $G(\tau)$, as in the following equation:

$$N_p = \left\lceil \frac{1}{\pi} fov_R \, \gamma \max\left(\int_0^t G(\tau)d\tau\right) \right\rceil, \; where \; 0 \leq t < T \tag{6.2}$$

, where T is the end of readout. Data is acquired using the same acquisition window as desired for imaging, and numerous k-spaces over encoding time can be obtained depending on the sampling rate.

6.2.2 FOV scaling search

For gradient measurement, a reference point at a certain encoding time is first selected among the SPI encoded data. Then, the relative FOV scaling factor directly reflects the relative k-space trajectory with respect to the k-space coordinate at reference encoding time, t_r, as following equation shows:

$$FOVscale(t) = \frac{FOV(t_r)}{FOV(t)} = \frac{\pi\gamma \int_0^t G(\tau)d\tau}{\pi\gamma \int_0^{t_r} G(\tau)d\tau} = \frac{k(t)}{k(t_r)} \tag{6.3}$$

, where t denotes a phase encoding time delay, and $k(t)$ is a k-space position in the unit of cycle m^{-1} at encoding time, t. Note that any data point can be used for the reference encoding time, t_r, however data acquired around the encoding time at which the SPI image has one-half of the required FOV (fov_R) may be desired such that both k-space and image domain 1D profiles contain enough information (or resolution) for reliable estimation of FOV scaling factors. Two possible approaches to estimate the relative FOV scaling factor exist: a k-space domain or an image domain approach, which can be formulated as a minimization problem. k-Space based optimization is shown in the following equation:

$$FOVscale(t) = \frac{FOV(t_r)}{FOV(t)} = argmin_s\, E_K\big(K(t, sk), K(t_r, k)\big) \quad (6.4)$$

,where $K(t,k)$ denotes the magnitude of k-space encoded at phase encoding time t in 1D SPI, s is a real number that is local FOV scaling factor, and E_K is an error function between two k-spaces. In practice since a finite number of data (N_p) is acquired, data interpolation is used to synthesize the scaled k-space K(t,sk) from original k-space K(t,k). Image domain optimization is performed as follows:

$$FOVscale(t) = \frac{FOV(t_r)}{FOV(t)} = argmin_s\, E_I\big(I(t, x/s), I(t_r, x)\big) \quad (6.5)$$

, where $I(t,x)$ denotes the magnitude of 1D image at encoding time t, and E_I is an error function between two images. As in k-space domain, interpolation is applied to synthesize the scaled image I(t,x/s).

The 1D profile in the image domain has more resolution (more information that can be used in FOV scaling search) when the FOV is small (Figure 6.1(e)), while the k-space profile shows a broader line-shape when the FOV is large (Figure 6.1(f)). To exploit this property, the two estimates may be combined using a simple merging filter as shown in Figure 6.1(g).

6.2.3 Absolute k-space trajectory

As shown in equation 6.3 above, the estimated FOV scaling factor, FOVscale(t), represents the relative k-space position at encoding time t with respect to the k-space position at the reference encoding time t_r. The absolute k-space trajectory, which allows reconstruction of the image at the prescribed FOV, can be calculated by simply scaling the relative k-space trajectory. Most trivially, this is done by scaling the unitless measured gradient waveform to match the prescribed gradient amplitude (e.g., in units of mTm^{-1}). Note that potentially more

accurate scaling could utilize the GIRF-distorted gradient waveform or consider only the plateaus of trapezoidal gradients. Alternatively, a phantom of known dimension could be scanned to obtain this calibration if the system gradient amplitude is inaccurate or unknown. If the targeted gradient system is well calibrated, the DC component at 0 Hz in Fourier transform of the measured and prescribed gradient can be used to obtain the scaling factor.

6.2.4 GIRF

We have utilized the SPI-based gradient measurement technique herein to estimate GIRF, using multiple triangular input gradients using methodology analogous to [105]. Figure 6.2(a) shows the pulse sequence diagram depicting the input gradients used for GIRF measurement. Note that a "pre-dephasing" gradient is prescribed before the input gradient to remove ambiguity in FOV scaling estimation due to the large FOV when SPI data is acquired near the center of k-space. We performed estimation of GIRF in the frequency domain (i.e., the transfer function) by

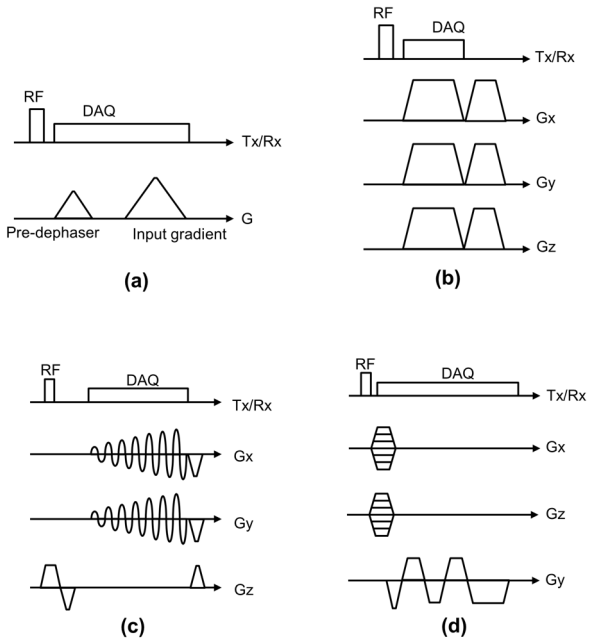

Figure 6. 2. Pulse sequence diagrams. (a) GIRF estimation, (b) Ultra-short echo (UTE) imaging, (c) spiral imaging, and (d) multi-echo bipolar GRE imaging. Note that in (d) a gradient spoiler is implemented by stretching the readout gradient.

dividing the measured output gradient by the prescribed input gradient after discrete Fourier transform to calculate a transfer function of the LTI system. The estimated transfer function is low-pass filtered to cut off unreliable, high frequency components using a reduced cosine filter.

6.2.5 Experimental setup

The imaging parameters for GIRF measurement, dynamic SPI based gradient measurement, and imaging experiments performed on three different scanners are shown in Table 6.1. For GIRF measurement of a 3T MR750 scanner (S1) (GE Healthcare, Waukesha, WI, USA) utilized 21 triangular gradients with amplitude between 7 mTm^{-1} and 33 mTm^{-1}, and a slew rate = 200 $mTm^{-1}ms^{-1}$ were used. A pre-dephasing gradient with amplitude 21.7 mTm^{-1} was placed with 464 μs spacing before the largest input gradient. To measure the GIRF of a 1.5T Signa HDxt scanner (S2) (GE Healthcare, Waukesha, WI, USA), 15 triangular gradients with amplitudes equally spaced between 6.7 mTm^{-1} and 20 mTm^{-1} were prescribed. A pre-dephasing gradient with amplitude 11.4 mTm^{-1} was prescribed with 476 μs spacing before the largest input gradient. Slew rate = 118 $mTm^{-1}ms^{-1}$ was used for all triangular gradients. To measure the GIRF of a 3T Signa PET/MR scanner (S3) (GE Healthcare, Waukesha, WI, USA), 21 triangular gradients with amplitude between 10 mTm^{-1} and 30 mTm^{-1}, and a slew rate = 118 $mTm^{-1}ms^{-1}$ were used. A pre-dephasing gradient with amplitude 21 mTm^{-1} was placed with 588 μs spacing before the largest input gradient. GIRFs for all scanners were measured with vender provided pre-emphasis correction turned on. A GE Healthcare 8-channel receive-only head coil was used, and a manufacturer-provided 15 cm spherical phantom (with no internal structure) was imaged. Total scan time to measure GIRF on each of the 3 scanners was 106 sec for S1, 75 sec for S2, and 106 sec for S3.

		GE MR750 (S1)	GE Signa HDxt (S2)	GE Signa PET/MR (S3)
GIRF measurement	**RF pulse**	24μs hardpulse	24μs hardpulse	24μs hardpulse
	Np	401	401	401
	Flip angle (degree)	6	6	6
	Slew rate ($mTm^{-1}ms^{-1}$)	200	118	118
	# of input gradient	21	15	21
	Pre-dephaser (mTm^{-1})	21.7	11.4	21.0
	Input gradients (mTm^{-1})	7~31	6.7~20	10~30
	Spacing (μs)	464	476	588
	TR(ms)	4.4	4.4	4.4
	Sampling rate (kHz)	500	250	500
	# of data points	988	378	982
	RF Coil	8-ch receive only head coil		
	Scan time (sec)	106	75	106
		3D UTE	**2D Spiral**	**3D Ramp sampling**
Imaging experiment	**RF pulse**	24μs hardpulse	Sinc pulse	24μs hardpulse
	Flip angle (degree)	6	30	6
	TE (ms)	0.09	2.42	Cartesian: 1.06, 1.97, 2.87, 3.77 Ramp sampling: 0.85, 1.49, 2.13, 2.77
	TR (ms)	3.3	13	Cartesian: 5.2 Ramp sampling: 3.7
	Sampling rate (kHz)	500	250	500
	# of data points	415	512	Cartesian: 1234 Ramp sampling: 1830
	# of TR	80000	48	101x31
	RF coil	8-ch receive only head coil	Single CH T/R coil	8-ch receive only head coil
	Scan time	4min 28 sec	0.6 sec	Cartesian: 16.3 sec Ramp sampling: 11.6 sec
SPI-based gradient measurement	**Np**	401	401	401
	TR (ms)	3.3	13	3.7
	Reference time, tr (ms)	0.29	2.94 for x-axis 3.18 for y-axis	21
	Sampling rate (kHz)	500	250	500
	# of data points	415	512	1830
	RF coil	8-ch receive only head coil		
	Scan time	4sec	quick: 42sec extensive: 385sec	1.5sec

Table 6. 1. Imaging parameters. The proposed method was tested on three different clinical scanners.

3D radial UTE imaging was performed on system S1 using a GE Healthcare 8 channel receive-only head coil. k-Space was encoded using a center-out half radial trajectory, using the pulse sequence shown in Figure 6.2(b). After RF excitation using a 24μs hard pulse, 80,000 spokes were scanned at TE=90 μs (after RF coil deadtime) with an encoding duration of 588 μs. The maximum amplitude of readout gradient was 35 mTm^{-1}, slew rate was 118 $mTm^{-1}ms^{-1}$, flip angle was 6 degrees, sampling bandwidth was 500 kHz, and TR was 3.3 ms. SPI-based gradient measurement was performed in the x, y, and z directions with Np = 401 using the same scan parameters. An image was reconstructed at FOV = 24x24x24 cm and 1x1x1 mm resolution using gridding. The brain of a human volunteer was scanned under approval from our institutions IRB, and a 15 cm spherical phantom was used for gradient measurement as in GIRF measurement. The scan time for UTE imaging was 4 min 28 sec, and the scan time to perform gradient measurement for all three gradient axes was 4 seconds in total.

2D spiral imaging was performed on GE Signa HDxt scanner (S2) using the pulse sequence in Figure 6.2(c). A single channel GE Healthcare transmit/receive head coil was used for imaging. A sinc pulse was used to achieve 30 degree flip angle, and a single axial slice at iso-center was obtained. 48 spiral arms with 512 readout points in an arm was encoded with a sampling bandwidth of 250 kHz. FOV was 12x12 cm, slice thickness was 8 mm, and spatial resolution was 1.04x1.04 mm. TR was 13 ms, and TE was 2.42 ms. SPI gradient measurement with Np = 401 was performed in two different ways for comparison: extensive and quick. All 48 different pairs of x and y gradients were measured with the extensive gradient measurement (385 seconds), while 2 pairs of x and y gradients were measured and reproduced to estimate trajectories for all 48 arms using a linear combination in the quick gradient measurement (42

seconds). In the quick measurement, the readout gradients in x and y-axis in the arm with rotational angle θ, $gx(\theta, t)$ and $gy(\theta, t)$, can be estimated by the following equation.

$$gx(\theta, t) = cos\theta * gx(0, t) - sin\theta * gy(\frac{3\pi}{2}, t)$$

$$gy(\theta, t) = sin\theta * gx\left(\frac{\pi}{2}, t\right) + cos\theta * gy(0, t). \quad (6.6)$$

Note that $gx(0, t)$, $gx\left(\frac{\pi}{2}, t\right)$, $gy(0, t)$, and $gy\left(\frac{3\pi}{2}, t\right)$ are measured gradient shapes, where $gx\left(\frac{\pi}{2}, t\right)$ can be interpreted as a x-gradient waveform realized in physical y-gradient, and $gy\left(\frac{3\pi}{2}, t\right)$ is y-gradient waveform realized in physical x-gradient. A 15 cm spherical phantom was used for gradient measurement as for the GIRF measurement, and a manufacturer-provided resolution phantom was scanned and reconstructed with the nominal and measured (extensively and quickly) k-space trajectory.

In the experiment for multi-echo bipolar GRE imaging, non-selective 3D GRE imaging was performed on GE Signa PET/MR scanner (S3) using an GE Healthcare 8 channel receive-only head coil, with 2 mm spatial resolution and FOV = 6x26x20 cm. Phase encoding was performed in x and z direction with 61 and 201 phase encoding steps, respectively, and frequency encoding was performed in y direction. 8 vials containing 0%, 5%, 10%, 15%, 20%, 30%, 40%, and 50% fat with a T_1 shortening agent were used for the experiment. Two different pulse sequences using the bipolar gradients shown in Figure 6.2(d) were used to acquire 4 gradient echoes, where the readout gradients with a longer and shorter plateau were used for the conventional Cartesian sampling and ramp sampling, respectively. TE was 1061, 1965, 2869, and 3773 μs for Cartesian sampling and 847, 1487, 2127, and 2767 μs for ramp sampling. The

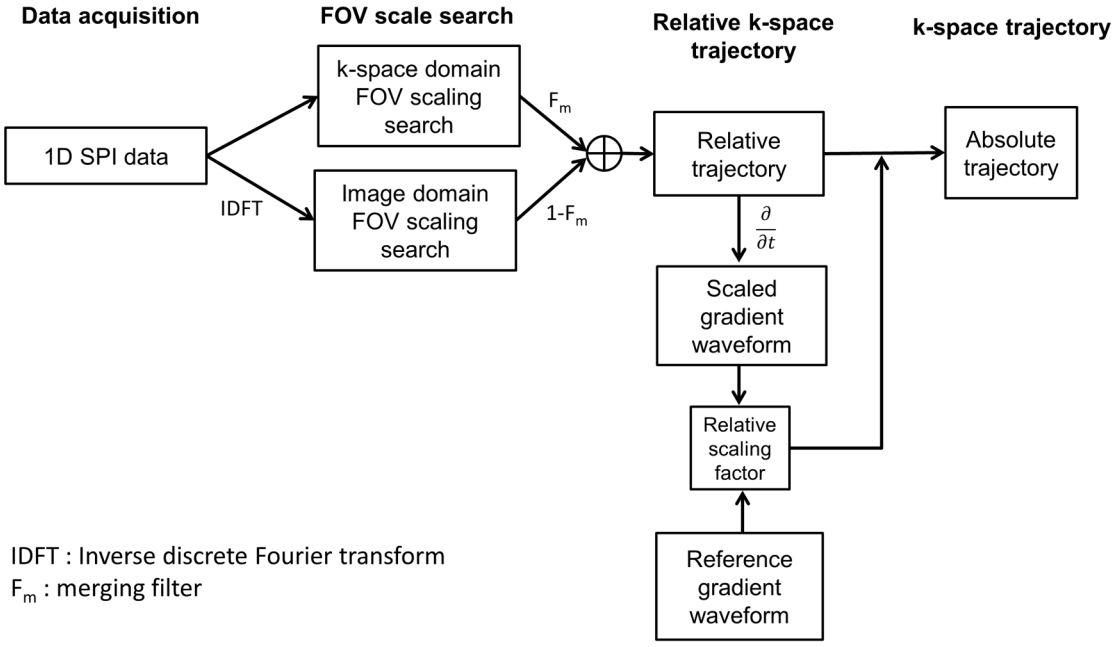

Figure 6. 3. Block diagram. This process is independently performed to obtain the k-space trajectory in each gradient axis.

maximum amplitude of the readout gradient for Cartesian or ramp sampling acquisition was respectively 22.6 mTm^{-1} or 33.0 mTm^{-1}. Note that a gradient spoiler was applied in the readout direction by stretching the trapezoidal gradient at the end of the pulse sequence. The minimum TR was 5.2 ms for Cartesian sampling and 3.7 ms for ramp sampling (a 29% reduction), where scan time was 16.3 sec for Cartesian and 11.6 sec for ramp sampling. A 24 μs hard pulse with a 6 degree flip angle was used, and the sampling rate was 250 kHz and 500 kHz bandwidth for Cartesian and ramp sampling acquisitions respectively. SPI-based gradient measurement was performed for ramp sampling in the readout direction (y-axis) with Np = 401. The acquisition time for gradient measurement was 1.5 sec. A 15 cm spherical phantom was used for gradient measurement.

6.2.6 Data processing

Figure 6.3 shows a block diagram delineating the steps in the proposed method. The acquired data were processed in MATLAB (The Mathworks Inc, Natick, MA, USA). In the FOV scaling factor search stage, the reference encoding time, t_r, is selected by referring to the nominal trajectory. Once the FOV scaling factors are estimated in k-space and image domain, they are combined using a merging filter. The merging filter was designed to have a linear slope in transition, where the width of transition was prescribed to cover five data points. Then, the absolute k-space trajectory is computed by scaling the relative k-space trajectory to physical gradient units. After estimating trajectories for the sampled k-space data, a convolution gridding reconstruction [45,46,83,108] was performed with oversampling ratio = 1.5 and a gridding kernel width = 5 pixels.

Note that any non-linear optimization method can be used to solve equation 6.4 and 6.5. In GIRF estimation, UTE imaging, and ramp sampling experiments, simple unconstrained optimization based on Nelder-Mead simplex (fminsearch in MATLAB) was used to estimate the FOV scaling factors. In the spiral imaging experiment, bounded nonlinear function optimization based on golden section search and parabolic interpolation[109] (fminbnd in MATLAB) was used for the FOV scaling search. The search range was set to ±7% of initial guess. The nominal k-space trajectory was used as an initial guess for the optimization in UTE imaging, and the GIRF-corrected trajectory was used as an initial guess for spiral imaging and ramp sampling. To scale the 1D image and k-space data in each iteration of optimization, cubic interpolation was applied. L2-norm and negative linear correlation were used as an error function for k-space (E_K) and image (E_I) respectively. Image domain SPI data was used for GIRF estimation, while k-space and image domain data was used for direct gradient measurement in UTE imaging, spiral

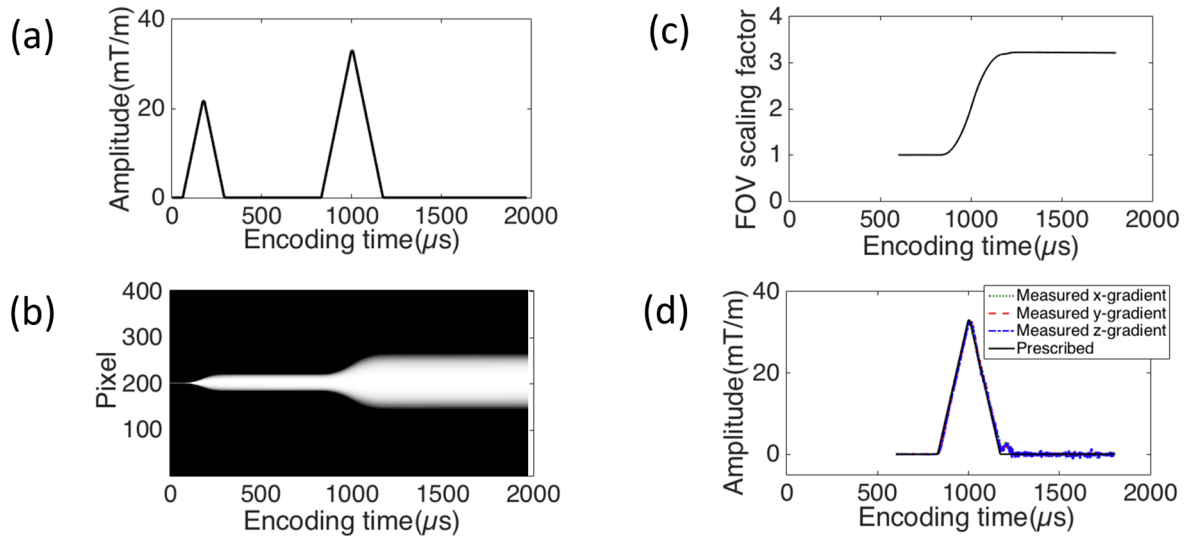

Figure 6. 4. SPI based GIRF estimation. (a) A prescribed gradient, (b) normalized magnitude of 1D SPI images over phase encoding time delays in the y-gradient, (c) estimated FOV scaling factors, (d) measured gradient shape. The size of the 1D projected object in (b) directly reflects the FOV scaling factor (or relative k-space trajectory) in (c).

imaging, and ramp sampling. To scale the unitless, relative gradient shape to an absolute gradient shape, estimated amplitudes in plateau of the first readout gradient was compared with the corresponding part in prescribed gradient shape in UTE imaging. In spiral imaging, entire gradient shape was compared with the GIRF-distorted gradient shape to scale the estimated gradient shape to obtain the correct FOV in image reconstruction. In multi-echo GRE imaging and all GIRF measurements in three systems (S1, S2, and S3), the DC component of Fourier transform measured and prescribed gradient waveform was used to obtain the absolute gradient shape.

In multi-echo bipolar GRE imaging, conventional Cartesian data (non-ramp sampled data) was directly reconstructed with no additional phase correction. Data acquired with ramp sampling was reconstructed using the GIRF-corrected trajectory or the measured trajectory. After

reconstructing multi echo images, Iterative Decomposition of Water and Fat With Echo Asymmetry and Least-Squares Estimation (IDEAL) was applied to obtain fat and water separated images[110], and the fat fraction was calculated.

6.3 Results

6.3.1 GIRF estimation

Figure 6.4(a) shows one input gradient with amplitude of 33 mTm^{-1} following a pre-dephasing gradient, which was used for GIRF estimation in S1. Figure 6.4(b) shows the normalized magnitude of the 1D SPI images over encoding time obtained in y-axis, and Figure 6.4(c) shows the estimated FOV scaling factors. Figure 6.4(d) shows the measured gradient

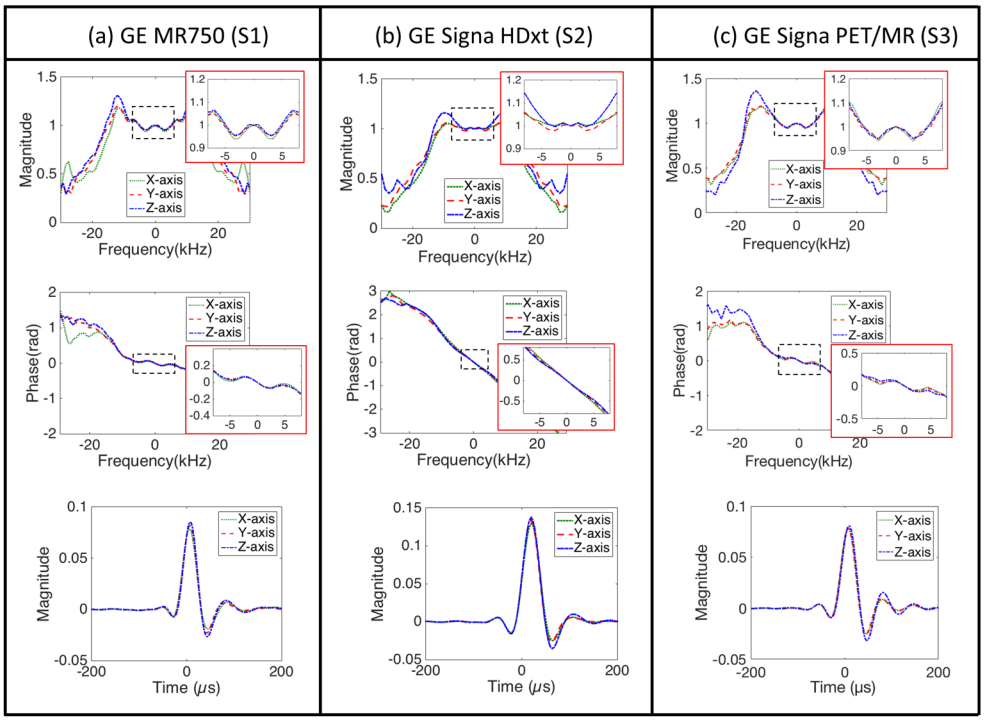

Figure 6. 5. Estimated GIRF. Magnitude and phase of GIRF in the Fourier transform domain and the corresponding time domain representation in (a) S1, (b) S2, and (c) S3. Note that the off-centered peak in GIRF implies group delay in gradient system.

shape. Figure 6.5(a),(b),(c) shows the estimated transfer function in the Fourier transform domain and the corresponding GIRF in the time domain for three different systems, S1, S2, and S3, respectively. The magnitude and phase of the estimated transfer functions (discrete Fourier transform of GIRF) in the frequency domain and the corresponding GIRFs in the time domain are shown here, which shows suppressed noise up to 20 kHz. The GIRFs were obtained by low-pass filtering and performing the inverse discrete Fourier transform to the transfer function**.** The parameters for the low-pass filter was empirically determined to suppress the amplified noise, where full width half max was 44.4 kHz, and the transition band was 16 kHz. The off-centered peak in the GIRF implies a group delay of approximately 8 μs for S1 and S3 and 20 μs for S2, which matches with an empirically observed delay in the three systems in our group.

6.3.2 Ultra-short echo imaging

Figure 6.6(a) shows the log magnitude of 1D k-space obtained using SPI encoding for gradient measurement in the x, y, and z-axis, and Figure 6.6(b) shows the magnitude of the corresponding 1D SPI images that are normalized by the maximum amplitude in each encoding time. Under the mono-polar trapezoidal gradient, the encoded 1D k-space shows time-narrowing line shape over encoding, while the 1D image shows a time-broadening shape, where the both k-spaces and images exhibit time-decreasing FOV. Figure 6.6(c) shows the GIRF measured trajectory, the SPI measured trajectory, and the nominal trajectory in physical x, y, z-axis, and a zoomed-in view, where group delay is shown between the nominal and the measured k-space trajectories. Figure 6.6(d) show the UTE images reconstructed with the nominal, GIRF, and SPI measured trajectory for a sagittal and axial slice. The image reconstructed with the GIRF and SPI measured trajectory shows good quality with no visible imaging artifact such as ringing, while the image with the nominal trajectory exhibits ringing and mis-aligned image components.

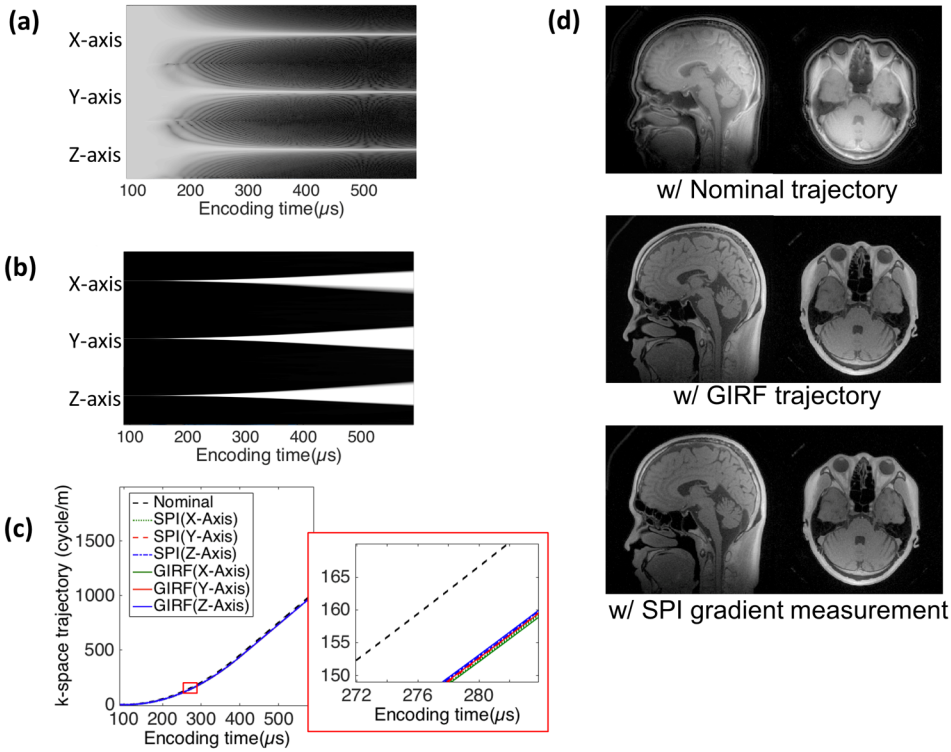

Figure 6. 6. 3D UTE imaging. (a) Log magnitude of k-spaces and (b) normalized images over encoding time in SPI data used for gradient measurement, (c) nominal, GIRF, and SPI measured k-space trajectory, (d) sagittal and axial slice of the image reconstructed with nominal trajectory, GIRF, and SPI measured trajectory. In the images with measured trajectory, no ringing artifact is visible, which is present in the images with nominal trajectory. Note that the coil component is also visible in the images with GIRF and SPI measured trajectory.

6.3.3 Spiral imaging

Figure 6.7(a) shows the nominal, GIRF measured, and SPI measured trajectory. Figure 6.7(b) shows the image reconstructed using the nominal trajectory, and Figure 6.7(c) shows images reconstructed with the delay-corrected trajectory where a group delay of 20 µs was used. Figure 6.7(d) shows images reconstructed with trajectory estimated using GIRF. Figure 6.7(e) and (f) show images reconstructed using the trajectory obtained by extensive and quick measurement, where all 48 spiral arms were measured independently or only 4 arms of measurement, respectively. Figure 6.7(g) shows a difference image relative to the image using

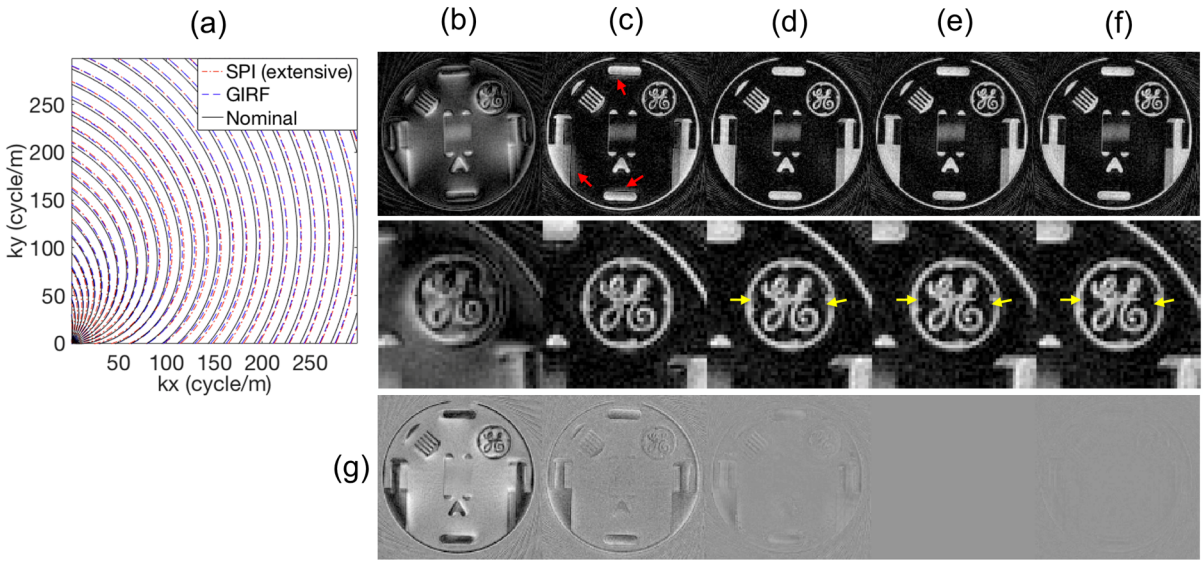

Figure 6. 7. 2D Spiral imaging. Reconstructed images with (a) Nominal and measured trajectory, image reconstructed with (b) nominal trajectory, (c) delay-corrected trajectory, (d) GIRF trajectory, (e) extensively measured trajectory, (f) quickly measured trajectory, and (g) difference image with respect to (e). Note that all 48 arms were individually processed in the extensive measurement in (e), while only 4 basis arms were processed in quick measurement in (f).

the extensively measured trajectory in Figure 6.7(e). The image reconstructed with the delay-uncorrected trajectory shows a severe blurring artifact, while the image with delay-corrected trajectory shows reduced blurring artifact, however there is remaining blurriness artifact as indicated by the red arrows. Images reconstructed using the GIRF-trajectory, extensively measured trajectory, or quickly measured trajectory show a much better result, while images with the measured trajectory show sharper edges as indicated by yellow arrows. The quick gradient measurement shows a comparable result to the full measurement as shown in the difference image in Figure 6.7(g), with 8.3% of the scan time compared to the extensive measurement time.

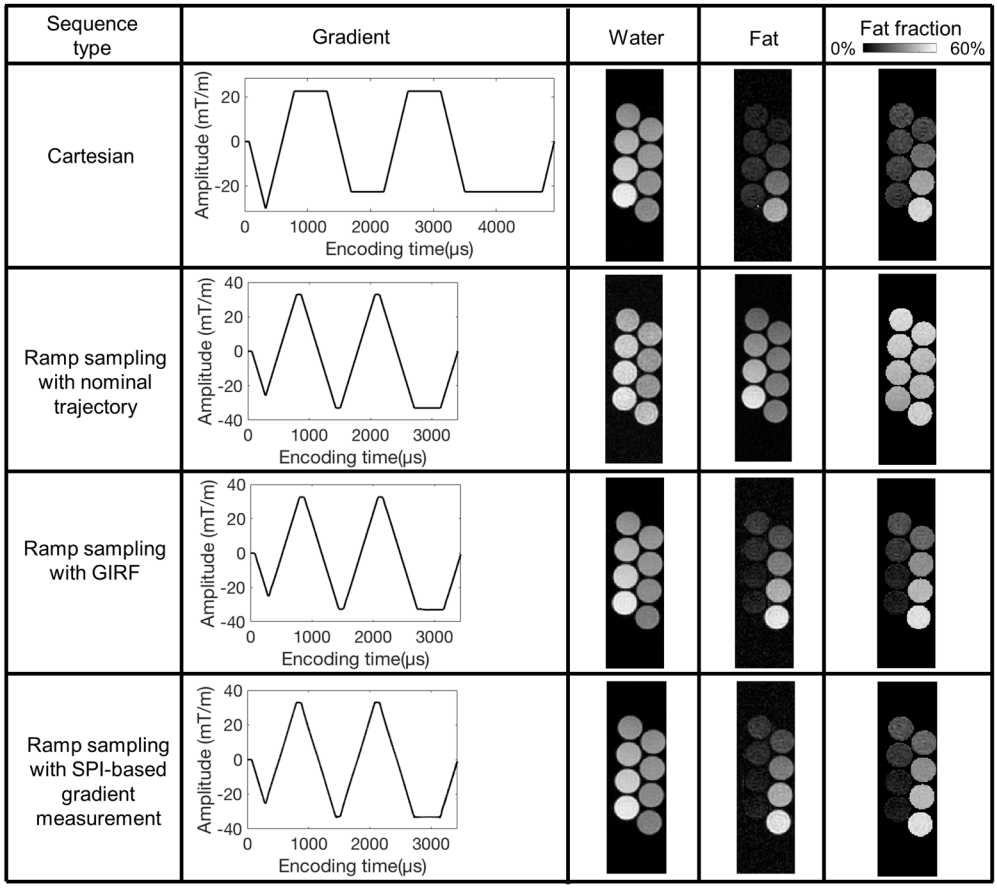

Figure 6. 8. Multi-echo bipolar GRE imaging. Ramp sampling images were reconstructed with nominal, GIRF-estimated, or SPI-measured trajectory. A cross sectional view of tubes with 0, 5, 10, 15, 20, 30, 40, and 50% fat fraction is shown here.

	SNR	0% fat (%)	5% fat (%)	10% fat (%)	15% fat (%)	20% fat (%)	30% fat (%)	40% fat (%)	50% fat (%)
Cartesian	55.3	10.4 ±13.2	12.2 ±21.5	13.0 ±2.3	13.8 ±3.1	13.2 ±2.8	21.5 ±2.1	34.6 ±1.6	47.3 ±1.8
Ramp sampling with nominal trajectory	45.9	37.9 ±1.9	42.3 ±1.7	46.7 ±1.9	50.4 ±1.8	48.1 ±2.0	43.5 ±2.1	42.6 ±1.7	48.2 ±1.7
Ramp sampling with GIRF	56.1	5.9 ±2.1	6.2 ±2.0	9.9 ±2.4	14.8 ±2.6	19.7 ±2.6	29.0 ±1.6	39.6 ±1.5	50.6 ±1.7
Ramp sampling with SPI-based measurement	56.4	5.4 ±2.1	6.2 ±2.2	10.3 ±2.3	15.3 ±3.0	19.8 ±2.5	29.1 ±1.7	39.8 ±1.5	50.3 ±1.8

Table 6. 2. Fat fraction. Conventional Cartesian imaging shows apparent error in fat fraction estimation due to the artefactual phase caused by mis-aligned k-spaces between gradient echoes. SNR was measured with separated water in all tubes.

6.3.4 Multi-echo bipolar GRE imaging

Figure 6.8 shows fat and water separated images and the resultant fat fraction map obtained by three different imaging and reconstruction schemes: conventional Cartesian imaging, ramp sampling with nominal trajectory, ramp sampling with GIRF, and ramp sampling with SPI-based gradient measurement. The measured gradients show the raw data (unfiltered) of the estimated gradient waveform. The SNR measured from the separated water in all tubes, the mean and standard deviation of estimated fat fraction in each tube are shown in Table 6.2. In conventional Cartesian sampling, erroneous estimation of fat faction is shown due to the phase error between the echoes acquired with positive and negative readout gradient. In ramp sampling with GIRF-estimated or SPI-measured trajectory, the estimation of fat fraction is significantly improved, which is likely due to a combination of the improved accuracy in the k-space sampling position that center-aligns k-spaces across echoes as well as the reduced echo spacing, while use of the nominal trajectory yields an incorrect estimation of fat fraction with lower SNR than in ramp sampling with the corrected trajectory. The SNR measured in ramp sampling was comparable with the SNR in Cartesian sampling. The estimated fat fraction shows both GIRF and SPI-based gradient measurement method allow robust measurement of the readout gradient.

6.4 Discussion

The proposed SPI-based gradient measurement technique does not require any special hardware unlike other reported methods for PGM and MFM that need specialized equipment such as NMR field probes(11,12,20,39). While these methods have been shown to be viable techniques to measure gradient waveforms, the use of external hardware adds complication and may be cost prohibitive. In the proposed method, a 15 cm spherical phantom was used to perform gradient waveform measurement; however in theory, any object (including a human

patient) can be used to perform gradient measurement. However, the imaged object does require definite boundaries (determined either by object size, coil sensitivity, or slice selectivity) to allow computation of the relative scale factors. The proposed method is robust to rigid motion of the object in two ways: the k-space scheme that only use magnitude that does not influenced by motion, and short measurement times that mitigate possible motion during the scan. The proposed SPI-based gradient measurement technique requires very minor modifications to the targeted pulse sequence, requiring only an additional loop during which the to be measured gradient amplitude is scaled for each gradient channel measured. Thus, this gradient waveform measurement can be added into existing sequences with little effort.

Compared with previously reported PGM[29,35,36] methods, where the number of RF pulses determines the resolution of estimated trajectory or gradient, the proposed technique allows higher resolution sampling of the gradient waveform (determined by the sampling bandwidth of the readout event). Therefore, the k-space position can be directly estimated from the measurement without any interpolation using the identical sampling rate for image acquisition. Furthermore, acquisition of the gradient measurement can be extremely rapid when the scan TR is short (e.g., ~1.5 sec per gradient axis). Furthermore, the use of the proposed methodology to perform in vivo measurement is feasible, where, for example, a database gradient measurement (e.g., obtained using a phantom) could be used to provide robust estimates for rapid gradient measurements. In vivo gradient measurement time for longer readouts (e.g., spiral and echo-planar imaging) could be further reduced by sub-sampling the number of phase encoding steps, particularly when a database calibration measurement is used. Note that in vivo calibration could be challenged when static field gradients due to magnetic field distortion is significant.

One additional feature of the SPI-based gradient measurement is that k-space trajectory can be independently recovered without knowing the history of previous k-space position. Theoretically, the FOV itself in a 1D SPI image is a direct and independent measure of k-space position as implied in equation 6.1. This allows flexibility to measure k-space trajectory in any type of pulse sequences even when the central region of k-space is not acquired as in hybrid encoding[8,13] and zero TE imaging[112–115]. Furthermore, in the SPI-based method, noise or mis-estimation at earlier encoding times is not propagated to the later estimation since no integration or cumulative summation is required to obtain k-space position.

As demonstrated herein, the proposed gradient waveform method can be used to improve the quality of reconstructed images. This is particularly important for non-Cartesian imaging where small k-space trajectory errors lead to significant artifacts as seen in Figure 6.6. Another application is the use of the technique to measure trajectories in more conventional Cartesian-type acquisitions. In Figure 6.8, improvement is seen in chemical-shift encoded imaging (IDEAL) with a multi-echo bipolar readout by reconstructing to a measured trajectory which reduces artefactual phase due to an inaccurate k-space trajectory[116–118]. Furthermore, ramp sampling reduced the total scan time by approximately 30%. The ability to perform a robust and rapid gradient measurement technique to enable ramp sampling, particularly for oblique slice orientations would be beneficial to many MRI sequences (e.g., fast gradient echo, echo-planar imaging, balanced SSFP, fast-spin echo) to provide moderate scan time reductions (20-30%) with minimal effect upon SNR.

The key idea of the proposed SPI-based gradient measurement technique is based on the assumption of linearity of the gradient distortion. This is typically a reasonable assumption when distortions are mostly caused by eddy currents that linearly scale with gradient amplitude.

However, these conditions may be violated in certain instances such as gradient operation close to the limit of slew rate and amplitude, resulting in nonlinear distortion in the realized gradient shape, which is a limitation of the proposed method based upon this LTI assumption. Furthermore, the demonstration of the proposed method relies upon accurate gradient amplitude calibration (which is already a requirement to enable geometrically precise MR imaging). If mis-calibrated, global geometric distortions will be apparent relative to the physical x, y, and z gradient errors. However, this scaling can readily be compensated for by imaging a phantom with known geometry (for which the proposed method would be particularly well-suited).

Concomitant field effects are another nonlinear factor that cause deviations in the k-space trajectory. These time-variant, non-linear magnetic fields depend on gradient amplitudes and are inversely proportional to field strength. The concomitant field effects become more problematic in imaging with long readout duration and preparation gradients (e.g. velocity encoding). Despite the efficacy of the proposed gradient measurement method as shown in the experiments herein, it is difficult to directly measure the concomitant magnetic field or higher order fields since in the proposed method (and other FGM and PGM methods) the gradient measurement is performed independently in each axis, based on the linearity assumption of the gradient system. In practice, concomitant magnetic fields are modeled as second order approximations and several successful correction methods have been proposed and implemented [94,119–121]. Thus, these additional correction terms could be readily applied to gradient measurement data obtained using the proposed method.

The proposed technique can be used as a calibration technique to estimate the GIRF without external hardware. As shown hereinbefore, the data collection for GIRF requires only 25~35 sec per gradient axis, making it very feasible for measurement during routine (e.g., daily

or weekly) quality assurance imaging. In the present experiment using triangular gradient blips, the spectral resolution is inherently limited, and hence it may not be sensitive to long lasting eddy currents which is not visible in the estimated GIRF. This could potentially be overcome by applying frequency sweep methods [107,122], which we will explore in future work.

6.5 Conclusions

In this study, we implemented a robust and rapid gradient measurement method based on dynamic SPI, which allowed accurate measurement of k-space trajectory with high fidelity and no need of additional equipment to improve reconstructed image quality.

Chapter 7. Ramped Hybrid Encoding for Improved Ultrashort Echo Time Imaging

7.1 Introduction

MR imaging of objects with extremely short transverse relaxation times such as bone[114,123–125], brain[126,127], lung[101,128,129], or teeth[112,130] is challenging due to the rapid signal decay of these tissues and the physical limitations of MR hardware. Particularly, performance of the gradient system is limited in slew rate and amplitude and thus is a critical factor in the design of Ultra-short TE (UTE) acquisitions. Conventional nonselective frequency-encoded 3D UTE (FE-UTE) methods utilize a radial trajectory to rapidly frequency encode k-space, by encoding the free induction decay as rapidly as possible in a "center-out" acquisition[3]. In these methods, data encoding must wait for the signal to recover from transmitter/receiver switching time (deadtime) to obtain non-corrupted central k-space data. However, overall encoding time is not optimal because the gradient must be ramped from zero to the maximum amplitude after deadtime.

Other techniques such as Back-projection Low Angle ShoT (BLAST)[131], Rotating Ultra-Fast Imaging Sequence (RUFIS)[4], or Water- And fat Suppressed Projection MR Imaging (WASPI)[132] perform encoding under constant gradients within a short TR, eliminating the need for gradient ramping during readout. Although this imaging scheme allows simple and fast imaging, data cannot be collected during the receiver deadtime, thus complicating acquisition of the central regions of k-space. To address this issue, methods such as Zero TE (ZTE)[112,114,115,125,129,130] and Pointwise Encoding Time Reduction With Radial Acquisition (PETRA)[8] have been proposed. While ZTE and PETRA are highly similar, ZTE utilizes an

algebraic reconstruction to estimate missing central regions of k-space and PETRA utilizes single point imaging (SPI) to encode the central regions of k-space. Unfortunately, the maximum gradient amplitude in these acquisitions is limited by unwanted slice selectivity due to bandwidth constraints of the RF pulse[34,115,133]. Similarly, the family of Sweep Imaging with Fourier Transform (SWIFT)[134–136] or Single-Point Ramped Imaging with T_1 Enhancement (SPRITE)[27,28,31,137] whose encoding gradients are turned on during RF excitation also exhibit unwanted slice selectivity issue.

In PETRA/ZTE, gradients are set to the maximum encoding amplitude, G_{max}, before the application of a short, high-bandwidth RF pulse, as depicted in the pulse sequence diagram shown in Figure 7.1 (a), to save the time required to ramp gradients and thereby shorten total encoding time. However, the effective gradient during RF excitation results in an unwanted slice selection effect, where the magnetization is not uniformly flipped, but subject to a non-uniform

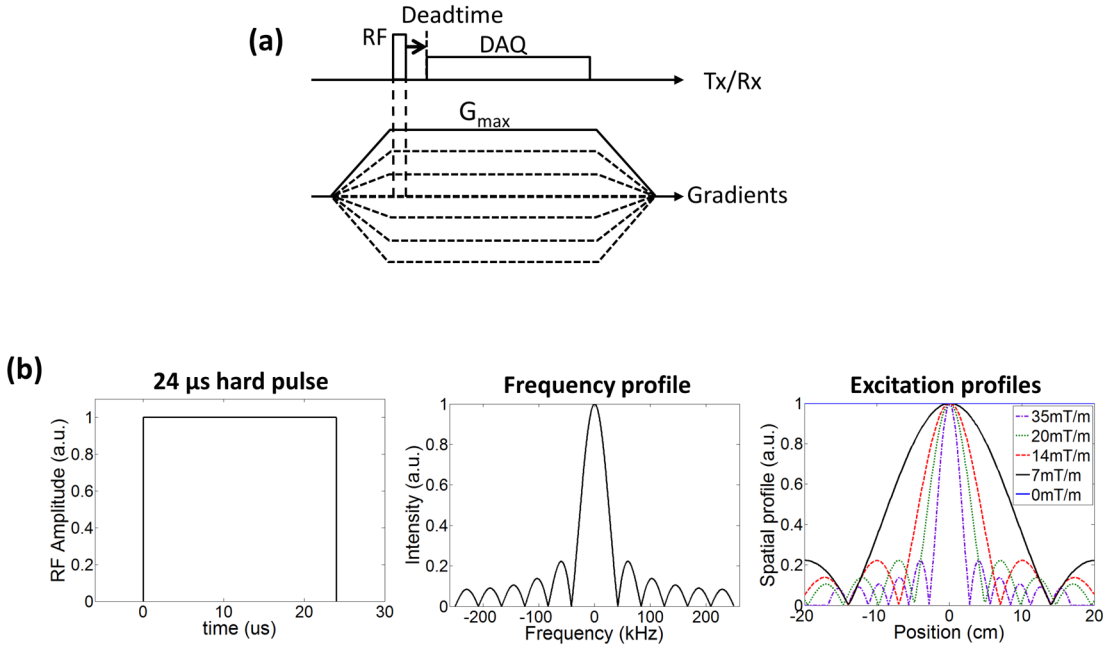

Figure 7. 1. Slice selectivity (a) PSD as used in PETRA/ZTE, and (b) Excitation profile of a 24µs hard pulse, Note that the degree of slice selectivity increases with encoding gradient amplitude in (b).

(e.g., sinc-shaped) excitation profile as shown in Figure 7.1 (b). The effective orientation and width of the slice selection change according to the orientation and amplitude of the encoding gradients. Therefore, encoded k-space data can be considered to come from an object with different slice selection, resulting in blurring and artifacts in the reconstructed image, manifested radially from the gradient isocenter. This artifact gets stronger as G_{max} increases, and a larger region of the image is affected by the blurriness.

This blurriness can be avoided by simply using an encoding gradient with low amplitude. However, in that case longer encoding time is required to achieve the desired spatial resolution, resulting in two significant limitations. First, the long encoding time reduces the spatial resolution of short T_2* species[138], resulting in blurring and loss of detail in the very components that are being imaged. Second, this results in chemical shift artifacts of the second kind (intravoxel fat-water interference), which results in an out-of-phase appearance, particularly at 3T and above. Shorter RF pulses with higher bandwidths can be used to alleviate the slice selection artifact; however, this limits the maximum attainable flip angle and thus reduces SNR and the capability to achieve T_1-weighted contrast. Several methods have been proposed to address the slice selection problem by performing post processing or modulating RF pulse[34,115,133].

In this chapter, we have developed a new encoding scheme, termed ramped hybrid encoding (RHE), which allows reduced per-excitation encoding time and minimized slice selectivity effects to improve the sharpness of high resolution UTE imaging. In RHE, gradients are held at low amplitude (e.g., below 7mTm^{-1} with a 24μs hard pulse for FOV=200mm) during RF excitation to minimize slice selectivity, and ramped to the maximum amplitude immediately following RF pulse. A 1D SPI-based gradient calibration method was developed to estimate the

true sampling trajectory of the encoding gradients. The efficacy of RHE was evaluated by comparing it to other UTE imaging schemes in computer simulation and phantom and in vivo experiments.

7.2 Methods

7.2.1 Ramped Hybrid Encoding

We propose RHE as a technique to allow the greatest flexibility compared to currently available methods in controlling unwanted slice selectivity while optimizing overall encoding time for ultrashort TE imaging. Figure 7.2 (a) shows the pulse sequence diagram for RHE. In RHE, an initial gradient during RF excitation, G_{RF}, is chosen to be small enough to minimize slice selectivity (by considering the limitations of the frequency profile of the RF pulse). After application of the RF pulse, the gradient is ramped to the maximum encoding amplitude, G_{max}, at the highest slew rate possible to minimize sampling duration. Data are acquired after RF deadtime until the desired spatial resolution is achieved.

As in PETRA, we have implemented RHE to use SPI to measure the data in central k-space that frequency encoding omits during RF deadtime. Central k-space is encoded by Cartesian SPI, and the outer k-space is acquired by frequency encoding as shown in Figure 7.2 (b). Note that in Figure 7.2 (a) the solid line in the pulse sequence diagram (PSD) shows gradient amplitude along the readout direction used to scan half radial spokes (blue arrows in Figure 7.2 (b)). The readout gradient is rotated over TRs to frequency-encode k-space as in a conventional radial acquisition. In Cartesian SPI sampling (red dots in Figure 7.2 (b)), the maximum gradient amplitude is linearly scaled as dotted lines in Figure 7.2 (a) shows to encode different k-space point at the constant encoding time over TRs. Note that the same maximum gradient is applied to

both SPI and frequency encoding to prevent discontinuity in encoding times at the interface between the two different encoding schemes. This acquisition can be extended to multi-echo acquisitions, where Figure 7.2 (c) shows the pulse sequence used to obtain multi-echo RHE images with 5 half-echoes obtained within a single acquisition. Note that by using SPI encoding to fill central region of k-space 5 half echoes can be obtained rather than 3 full echoes of the conventional gradient echo acquisition.

In RHE, the diameter of the SPI-encoded region in k-space, N_{SPI}, is determined by the following equation.

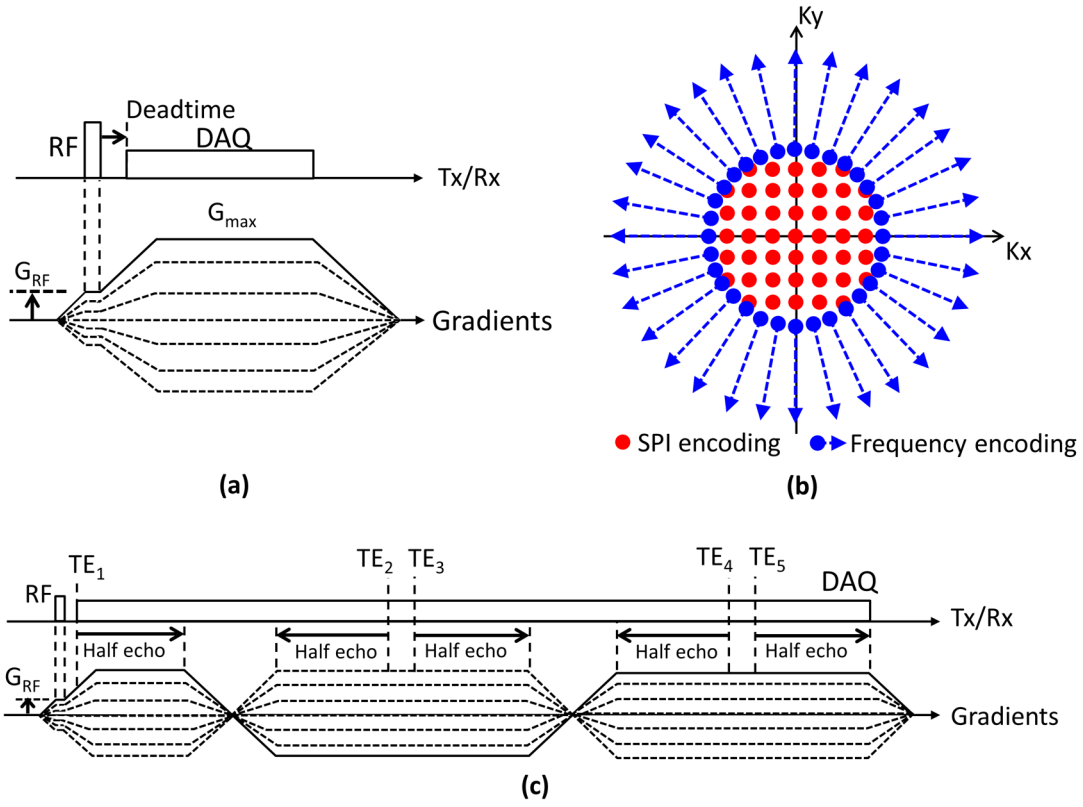

Figure 7. 2. Ramped Hybrid Encoding (RHE). (a) Pulse sequence diagram, (b) sampling scheme, and (c) example of a multi-echo encoding scheme. RHE allows flexible control of G_{RF} to minimize slice selectivity artifacts, and allows the best possible encoding time by rapidly ramping gradient after RF excitation. Like PETRA, single point encoding is employed to acquire central k-space data.

$$N_{SPI} = \lceil 2\bar{\gamma}\, fov_D(G_{RF}t_D + 0.5\, g_S\, t_D^2)\rceil \quad if\ t_D \le (G_{max} - G_{RF})/g_S,$$

$$\lceil 2\bar{\gamma}\, fov_D(G_{max}t_D - 0.5\, (G_{max} - G_{RF})^2/g_S)\rceil \quad otherwise, \tag{7.1}$$

where $\bar{\gamma}$ is the gyromagnetic ratio in unit of Hz/T, g_S denotes gradient slew rate in units of $Tm^{-1}s^{-1}$, fov_D denotes the desired field of view (FOV), and t_D is the desired echo time chosen after deadtime. Due to eddy currents that effectively derate the gradients in ramping, SPI data are prone to be slightly oversampled and hence result in a larger FOV than the desired FOV (fov_D) at the desired TE (t_D). The FOV can be corrected in the reconstruction stage using conventional convolution gridding methods. In practice, larger N_{SPI} can be intentionally used to obtain more oversampled SPI data allowing some flexibility in selecting TE when RF deadtime is not known a priori.

The maximum gradient amplitude during RF excitation, G_{RF}, can be selected by considering both slice selectivity and N_{SPI}. An upper bound for G_{RF} can be analytically determined using the expected RF pulse shape and its frequency profile. However, large G_{RF} amplitudes may result in impractical scan times due to a large N_{SPI} required. In that case, G_{RF} needs to be reduced to allow reasonable scan times. The maximum readout gradient, G_{max}, can be as large as possible within the constraints of the readout bandwidth and safety factors such as gradient heating and peripheral nerve stimulation.

7.2.2 Gradient calibration

In RHE, data is acquired during ramping gradients. Therefore, timing errors and eddy current effects may distort the k-space sampling trajectory, and hence naïve reconstruction based on the prescribed gradient parameters is generally not suitable. In this study, we developed a new calibration method that benefits from the well-known zoom-in effect (decreasing FOV with

increasing phase encoding time delay) in SPI[6,31,137]. For calibration, three sets of 1D projection images are acquired using an SPI scheme in each gradient axis. 1D SPI imaging can be easily implemented in any pulse sequence by scaling the gradients to enable pure phase encoding. To phase encode different points in k-space over TRs, the prescribed gradient is linearly scaled. Typically this calibration data can be acquired very rapidly, within a few seconds for all gradient axes.

1D single point images can be reconstructed without calibration. The three sets of 1D projection images across a range of encoding time are reconstructed at native FOVs (exploiting

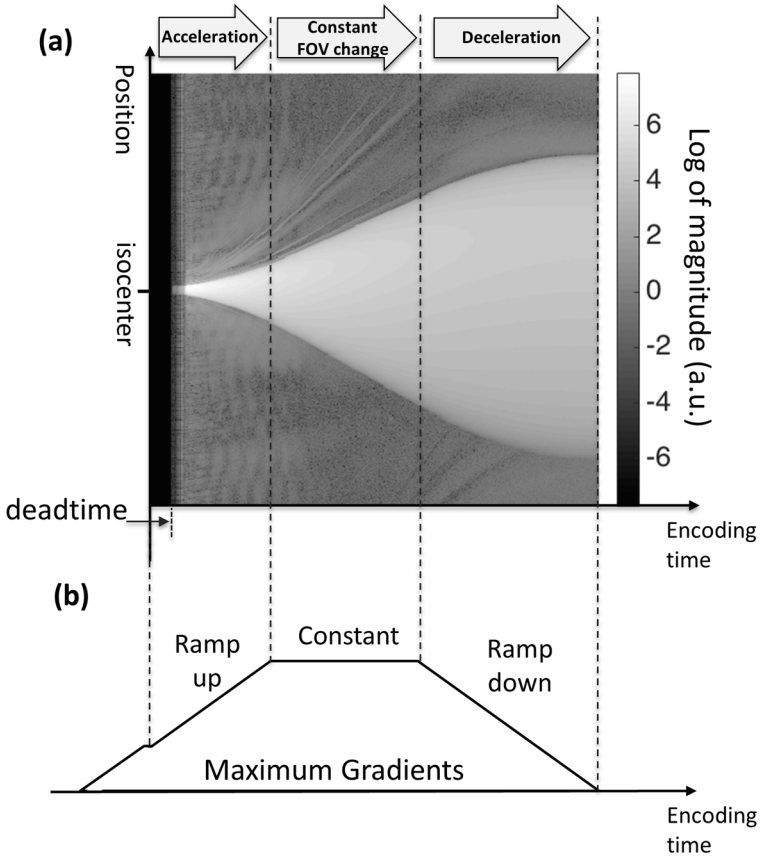

Figure 7. 3. The zoom-in effect of SPI and gradient calibration. (a) 1D SPI image matrix, and (b) the prescribed gradient shape. Note that the FOV change in (a) directly represents gradient shape in (b), which can be utilized for gradient calibration.

the zoom-in effect), as depicted in Figure 7.3. The image matrix shown in Figure 7.3 (a) contains 1D projection images (y-axis) versus phase encoding time delay (x-axis) for a gradient direction encoded by 1D single point imaging. The size of the object (bright region in center of FOV) increases with encoding time (zoom-in effect). The speed of FOV change in Figure 7.3 (a) is directly proportional to the gradient strength shown in Figure 7.3 (b), exhibiting acceleration in ramping up, constant change in plateau, and deceleration in ramping down. Therefore, the gradient waveform can be calibrated by estimating the scaling factors between neighboring phase encoding time delays within the 1D SPI data.

The FOV scaling factors between images are found automatically using unconstrained nonlinear optimization (Nelder-Mead Simplex). A reference image is first selected as the latest time delay, t_{ref}, and the relative scaling factors between t_{ref} and other time delays are found by minimizing the L_2-norm of the error function as shown in the following equation.

$$FOVscale(t) = FOV(t_{ref})/FOV(t) = argmin_s \sqrt{\sum_{x=1}^{N} |I(t_{ref}, x) - I(t, s(x - N_c) + N_c)|^2} \quad (7.2)$$

, where I(t,x) denotes magnitude of 1D image at encoding time t and spatial position x, N is 1D matrix size, s is a scaling factor between images, and N_c is index for the center of image (e.g., for matrix size=N, $N_c = \lceil N/2 \rceil$). Images are transformed based on the scaling factor, s, to find the best scaling factor. Scaling transformation can be performed in the either image or k-space domain by using an affine transform or convolution gridding, respectively. In this study, the transform was performed in the image domain using bilinear interpolation because it provided reliable results that could be computed much faster than using a gridding approach.

Once proper FOV scaling factors are found across all phase encoding time delays, relative k-space position can be recovered. Note that the FOV scaling factors only describe the relative scaling difference between encoding times. To obtain the absolute FOV, we examine the RHE data acquired during constant gradient. First, the slope of FOV scaling factors is calculated at a time (t_{ref}) when the gradient is constant (and known) G_{max}. Then, the slope can be used to calculate the true FOV at the reference encoding time, t_{ref}, using following equation.

$$FOV(t_{ref}) = c(N-1)/(2\bar{\gamma}G_{max}) \tag{7.3}$$

, where c is slope of FOV scaling factor found at constant gradient. Now, the FOV for the entire encoding time, FOV(t), can be recovered by simply using equation 7.2 with the given FOVscale(t) and FOV(t_{ref}).

7.2.3 Image reconstruction

After the k-space trajectories are calculated via the above gradient calibration method, the acquired SPI and radial data are combined together. 3D convolution gridding is applied to obtain the k-space with desired FOV[45,46,83]. To control variable density sampling within k-space, iterative density compensation[108] is applied. Note that the sampling density along a half radial spoke in frequency encoding is determined by readout bandwidth and the shape of the encoding gradient, while within the SPI region it is determined by TE and the shape of the encoding gradient. In Figure 7.4, a block diagram shows how raw data are processed to obtain a final RHE image.

7.2.4 Computer simulation

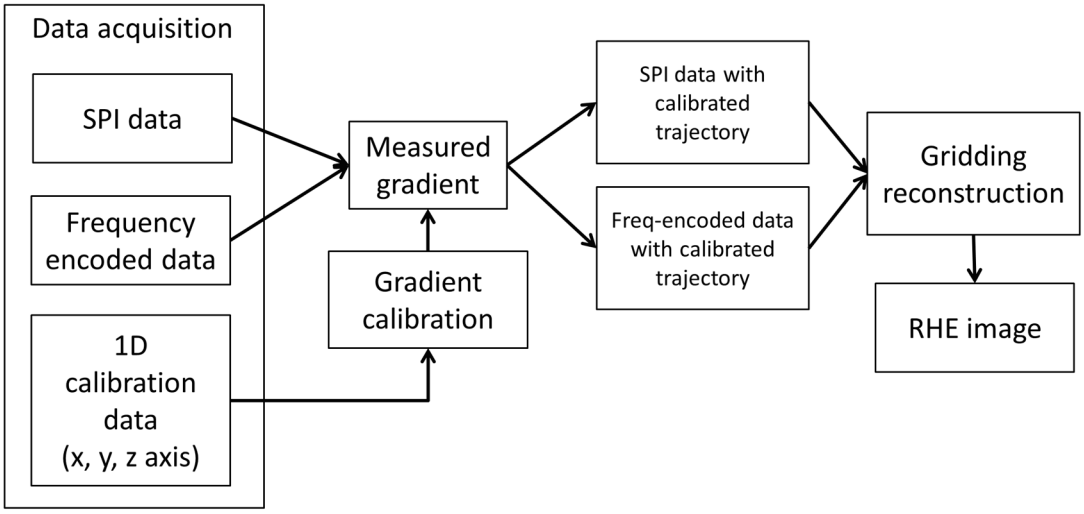

Figure 7. 4. Raw data processing in RHE. Raw data acquired by RHE contains Cartesian SPI data, radially frequency encoded data, and 3 sets of 1D SPI data for calibration. After calibration, combined data with estimated k-space position are processed by convolution gridding.

To compare encoding times and the resultant image quality between RHE and other UTE imaging schemes, a 1D computer simulation was performed. Note that a conventional point spread function (PSF) simulation is not possible because the PSF is spatially-variant at each encoding position in k-space, as described above. Therefore, each point in k-space was independently simulated using a 1D digital phantom. To generate the 1D digital phantom, 11 tubes were generated with different proton densities, 0.7, 1.0, 0.7, 0.3, 0.7, 1.0, 0.7, 0.3, 0.7, 1.0 and 0.7 in arbitrary unit from left to right. The diameter of each tube was 40mm. A mono-exponential T_2* decay model (T_2* = 100μs or 500μs) was simulated for all tubes.

System parameters included a TE of 80μs, a slewrate of 118 mTm-1ms^{-1}, and a maximum gradient of 35 mTm^{-1}. For PETRA Gmax = 7 or 20 mTm^{-1} was used. For RHE, GRF = 3.5 or 7 mTm^{-1} and Gmax = 35 mTm^{-1} was used. For RHE and FE-UTE, the gradients were ramped immediately after the RF pulse or after deadtime, respectively. 1D sampling was simulated using

	Phantom					Knee	Brain				
	PETRA	PETRA	PETRA	UTE	RHE	RHE	PETRA	PETRA	PETRA	UTE	RHE
G_{max} (mTm^{-1})	7	14	20	35	35	35	7	14	20	35	35
G_{RF} (mTm^{-1})	n/a	n/a	n/a	n/a	7	5	n/a	n/a	n/a	n/a	7
RF pulse width (μs)	24					24	8, 24				
Flip angle (^{o})	6					6	2, 6				
NSPI	33	33	33	n/a	33	33	33	33	33	n/a	33
# of SPI encoding	17707	17707	17707	n/a	17707	17707	17707	17707	17707	n/a	17707
# of FE encoding	80000	80000	80000	80000	80000	80000	80000	80000	80000	80000	80000
Slew rate ($mTm^{-1}ms^{-1}$)	118	118	118	118	118	118	118	118	118	118	118
TE (μs)	90	90	90	90	90	90, 1502, 1550, 2900, 2950	90	90	90	90	90
T_{Enc} (μs)	1680	838	588	588	438	788	1680	838	588	588	438
TR (ms)	3.3	3.3	3.3	3.3	3.3	5.6	3.3	3.3	3.3	3.3	3.3
RF coil	8ch receive only head coil					8ch T/R knee coil	8ch receive only head coil				
Scan time	5m 23s	5m 23s	5m 23s	4m 28s	5m 23s	9m 10s	5m 23s	5m 23s	5m 23s	4m 28s	5m 23s

Table 7. 1. Parameters for MR experiments.

frequency encoding or PETRA/RHE encoding to acquire a 500x1 k-space with FOV=500mm, which achieves approximately 1mm resolution. For PETRA and RHE, the slice selectivity effect was simulated using the spatial profiles of the 24μs hard pulse shown in Figure 7.1(b). NSPI was set to the minimum value according to the prescribed gradient shape (NSPI=24, 69, 29, and 40 respectively for PETRA with Gmax=7mTm^{-1}, PETRA with Gmax=20mTm^{-1}, RHE with GRF=3.5mTm^{-1}, and RHE with GRF=7mTm^{-1}). No eddy current effects were applied in the computer simulation.

7.2.5 Experimental setup

To evaluate the proposed encoding scheme, MR experiments were performed on a 3.0T MR scanner (MR750, GE Healthcare, Waukesha, WI). A phantom experiment was performed to compare UTE imaging schemes (PETRA, FE-UTE, and RHE) with an object that only has short T_2* components. Human brain imaging was performed with 2 different RF pulses (8μs, 24μs) with flip angle 2^o and 6^o respectively) and gradient settings. A multi-echo RHE experiment to generate a short T_2* image was performed in the human knee.

For phantom experiments, a phantom made of Acrylonitrile Butadiene Styrene (ABS) plastic (Big ben, item # 21013, a cowboy minifigure from palace cinema, item # 10232, and a white horse made by LEGO, Billund, Denmark) with T_2* approximately 400-500μs. An 8-ch receive-only head coil (GE Healthcare) was used for the phantom experiment. For in vivo experiments, a human subject was imaged in accordance with local IRB protocols. The 8-ch receive-only head coil was used for in vivo brain imaging, and an 8-ch transmit-receive knee coil (GE Precision Eight Knee Array Coil, Invivo, Gainsville, Florida) was used for in vivo knee imaging.

All parameters used for the phantom, knee, and brain imaging are shown in Table 7.1. A single echo acquisition (as shown in Figure 7.2 (a)) was performed in phantom and brain imaging, while multi-echo imaging (as shown in Figure 7.2 (c)) was performed in the knee. For all datasets the TE was 90μs, which is defined as the first encoding time after which the receiver is fully recovered from RF deadtime (as shown in Figure 7.3 (a)). Deadtime was determined empirically by observing the signal magnitude at the center of k-space. A sampling period of 2μs was used. In the phantom and knee imaging experiment comparing PETRA, FE-UTE, and RHE, N_{SPI} and TR were set identically to allow reasonable comparisons between imaging schemes.

N_{SPI} was set to 33, the largest N_{SPI} required by PETRA with largest G_{max} (=20mTm^{-1}), while TR was set to 3.3ms, is the minimum TR of PETRA with lowest encoding gradient (G_{max}=7mTm^{-1}). The minimum possible TR for RHE can be significantly shorter (approximately 2ms).

To perform gradient calibration, three 1D 401x1 SPI images were acquired along each physical gradient axis using linearly scaling encoding gradient over TRs (401 equispaced steps between -1.0x and 1.0x of gradient shape to calibrate). The additional scan time required for the calibration was 401(encodings/axis) x 3(axis) x TR, which is 4 sec for a single echo acquisition and 6.7 sec for multi-echo acquisition. For more reliable calibration, SPI-based calibration was first performed using a spherical phantom (in a separate imaging session on a separate day and only once for all experiments), which was then used as the initial guess during calibration. The proposed SPI-based calibration was applied to both FE-UTE and RHE imaging.

During image reconstruction, convolution gridding was performed using a Kaiser-Bessel kernel with grid width=5 (for phantom and head imaging) or 7 (for knee imaging) and oversampling ratio=2. Phantom data were gridded to achieve FOV=200mm and matrix size of 201x201x201, and brain data were gridded to achieve FOV=240mm and matrix size of 241x241x241, which is equivalent to 1mm resolution. In knee experiment five 3D knee images were reconstructed at TE=90μs, 1502μs, 1550μs, 2900μs, and 2950μs with FOV=200mm and a matrix size of 401x401x401, which is equivalent to 0.5 mm resolution. Separate fat and water images were computed using Iterative Decomposition of water and fat with Echo Asymmetry and Least-squares estimation (IDEAL)[110]. All 5 images at different TE were used for the IDEAL reconstruction. The image representative of short T_2* species was obtained by subtracting the computed water and fat images from the RHE image at TE=90μs.

7.3 Results

7.3.1 Simulation results

Figure 7.5 shows the simulated curves for the per-excitation encoding time in three different UTE encoding schemes, conventional FE-UTE, PETRA/ZTE, and RHE, (Figure 7.5 (a)) and the corresponding reconstructed images (Figure 7.5 (b),(c)). As seen in Figure 7.5 (a), RHE with G_{RF}=7mTm^{-1} allows the shortest per-excitation encoding time (=429μs) between the three methods (1669μs for PETRA with G_{max}=7mTm^{-1}, 584μs for PETRA with G_{max}=20mTm^{-1}, 562μs for FE-UTE, and 454μs for RHE with G_{RF}=3.5mTm^{-1}) while controlling for blurring caused by T_2* or the finite RF pulse duration. The reconstructed images with normalized scales are shown in Figure 7.5 (b),(c). Root Mean Squared Error (RMSE) was calculated using the normalized images.

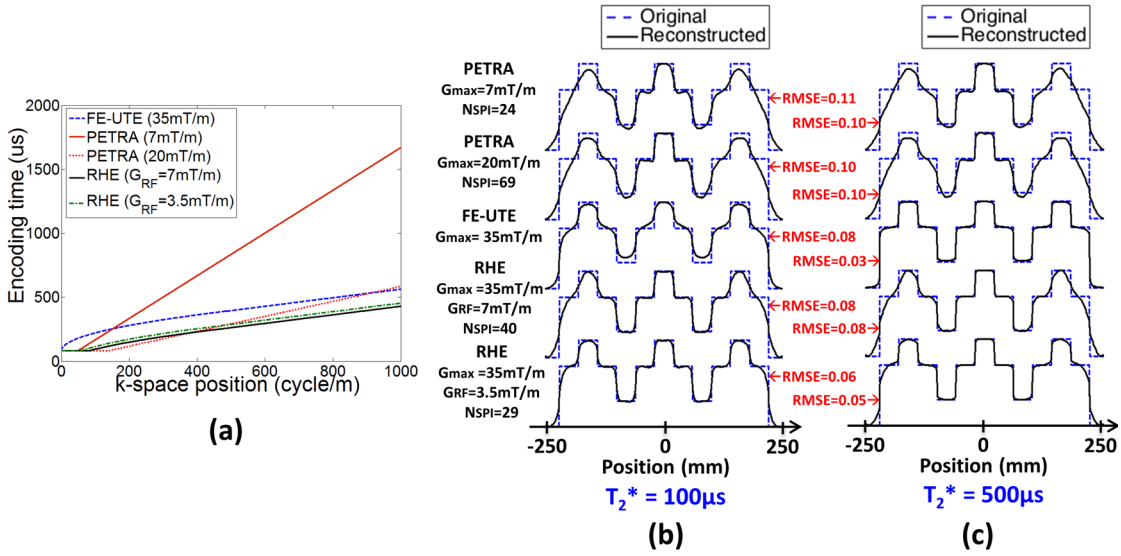

Figure 7. 5. Simulation of (a) per-excitation encoding time and simulated 1D imaging with (b) T_2*=100μs and (c) T_2*=500μs. N_{SPI} was set to 24, 69, 29, and 40 respectively for PETRA with G_{max}=7mTm^{-1}, PETRA with G_{max}=20mTm^{-1}, RHE with G_{RF}=3.5mTm^{-1}, and RHE with G_{RF}=7mTm^{-1}. Note that RHE provides the shortest per-excitation encoding time and the best image reconstruction for short T_2* imaging over a wider field-of-view than PETRA and FE-UTE.

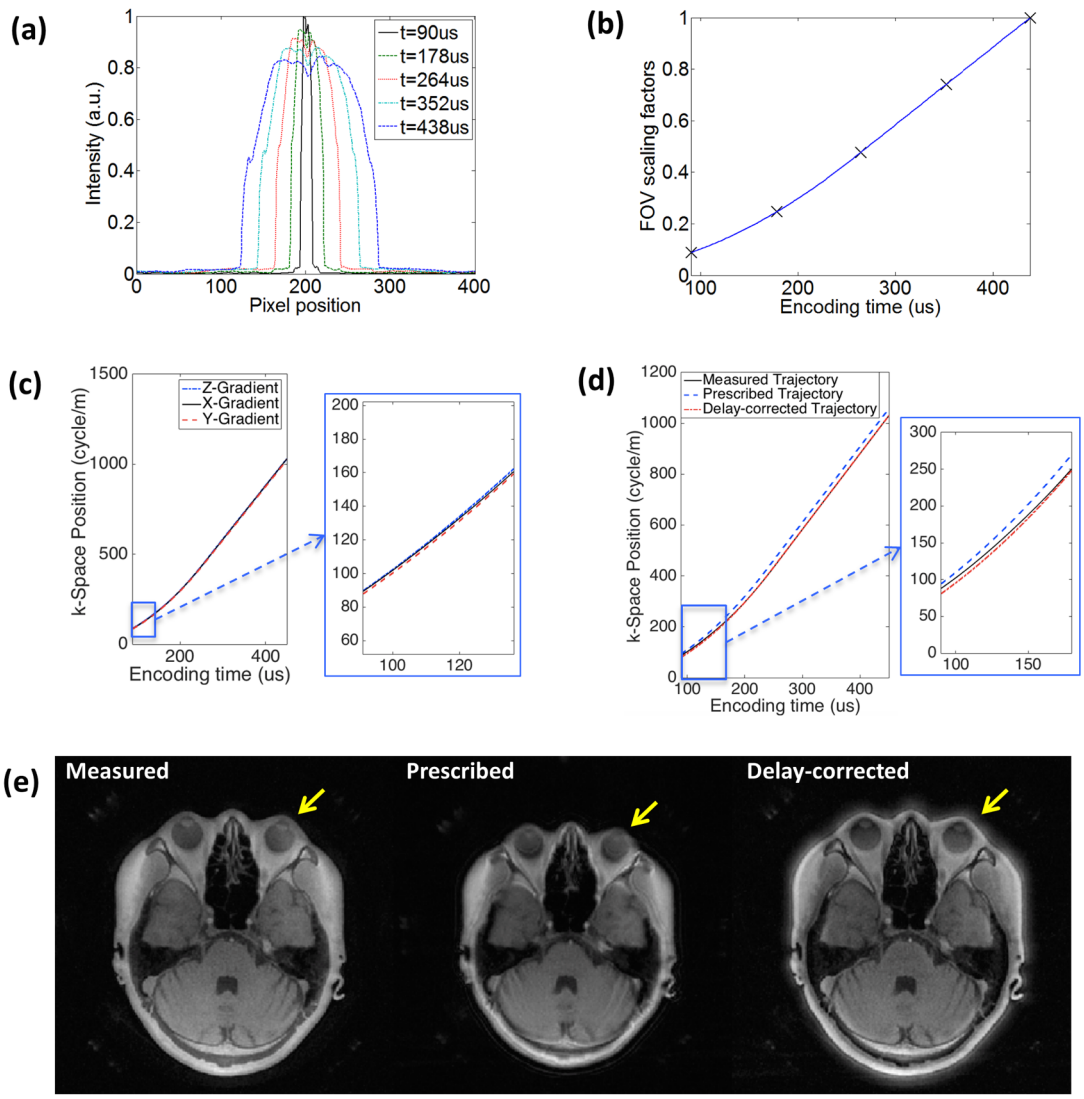

Figure 7. 6. Gradient calibration. (a) 5 1D images from calibration data in the x-direction exhibiting a zoom-in effect from SPI, (b) the corresponding scaling factors computed from (a), (c) the measured k-space trajectory in each gradient axis, (d) comparison with prescribed or delay-corrected trajectory, and (e) the resultant images. Note that reconstruction with the prescribed trajectory (middle) results in substantial error in the image (ringing) and an incorrect FOV. The delay-corrected trajectory (right), while having the correct FOV, has blurring and ringing compared to the image reconstructed with the measured trajectory (left).

When T_2* is extremely short (100μs), RHE with G_{RF}=3.5mTm^{-1} provides the most accurate reconstruction (RMSE=0.06) owing to its optimized encoding time and controlled slice selectivity. PETRA images show good fidelity at the center of the FOV, but exhibit loss of detail

toward the edges due to the unwanted slice selectivity imposed by high encoding gradients applied during RF excitation. Note that PETRA with G_{max} = 20mTm^{-1} provides good reconstruction at the center of the FOV owing to the large N_{SPI}(=69) where encoding time is constant (=TE), resulting in less intra-readout T_2* decay. However, a larger N_{SPI} significantly increases the total image acquisition time and is not clinically feasible. FE-UTE shows uniformly reasonable results over the entire FOV as expected. When T_2* is moderately short (=500μs), FE-UTE shows the overall best reconstruction (RMSE=0.03), while RHE with G_{RF}=3.5mTm^{-1} shows a comparably accurate reconstruction (RMSE=0.05).

7.3.2 Gradient calibration

Figure 7.6 (a) shows 1D projection single point images from the x-axis of a calibration dataset reconstructed at native FOVs exhibiting the zoom-in effect (decreasing FOV with increasing phase encoding time delay). Figure 7.6 (b) shows the FOV scaling factors found between images in x-direction where 'x' shows 5 FOV scaling factors corresponding to the 5 images in Figure 7.6 (a). Figure 7.6 (c) shows the calibrated trajectory along 3 gradient orientations. Note that the estimated trajectories are different between gradient axes. Figure 7.6 (d) shows the measured trajectory, the prescribed trajectory, and delay-corrected trajectory obtained in the physical z-gradient direction. The delay-corrected trajectory was obtained by matching the linear part of the prescribed k-space trajectory with the measured trajectory. The two superimposed curves for measured trajectory and the delay-corrected trajectory show little difference in the ramping portion of the encoding gradient. As seen in the images reconstructed with the three different k-space trajectories in Figure 7.6 (e), small errors result in significant and obvious reconstruction error as shown in the region yellow arrow indicates, which shows

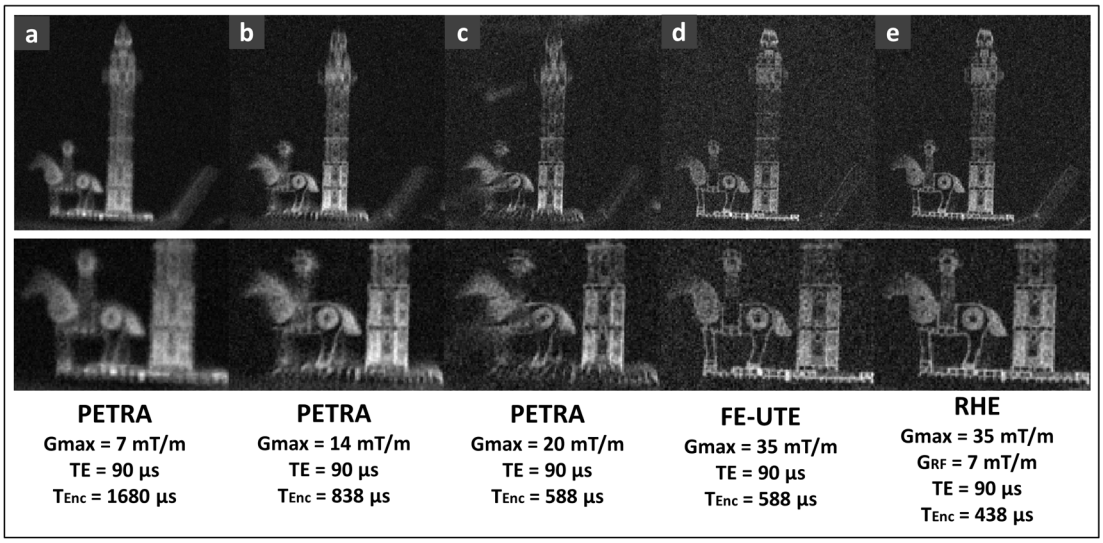

Figure 7. 7. Phantom experiment. PETRA with (a) G_{max}=7mTm^{-1}, (b) G_{max}=14mTm^{-1}, (c) G_{max}=20mTm^{-1}, (d) FE-UTE with G_{max}=35mTm^{-1}, and (e) RHE with G_{RF}=7mTm^{-1} and G_{max}=35mTm^{-1}. RHE allows the shortest per-excitation encoding time, yielding the best image quality.

misalignment between low and high frequency component in image due to the erroneous gradient calibration.

In our computational environment, the proposed calibration took approximately 2 sec to process one image, which requires 2 (sec/image) x 230 (images) / 12 (# of parallel computation) = 38 sec for single echo imaging and 2 (sec/image) x 1,630 (image) / 12 (# of parallel computation) = 272 sec for multi-echo imaging.

7.3.3 Phantom experiment

Figure 7.7 shows the results of the phantom experiment. Note that in the reconstructed images, RHE (Figure 7.7 (e)) preserves the high frequency details of the phantom much better than PETRA's (Figure 7.7 (a),(b),(c)) and FE-UTE (Figure 7.7 (d)), owing to the faster encoding that imposes less impact of T_2* decay.

PETRA with G_{max} = 7 mTm^{-1} (Figure 7.7 (a)) exhibits severe blurriness across the image, due to the long encoding time. PETRA with G_{max} = 14 mTm^{-1} (Figure 7.7 (b)) shows a more detailed depiction of the object, but it exhibits blurriness along radial direction at edge of FOV, which is due to unwanted slice selectivity. PETRA with G_{max} = 20 mTm^{-1} (Figure 7.7 (c)) shows the best spatial resolution in center of FOV and the worst slice selectivity artifact in corners of FOV due to the large gradient applied during RF excitation. FE-UTE (Figure 7.7 (d)) shows a

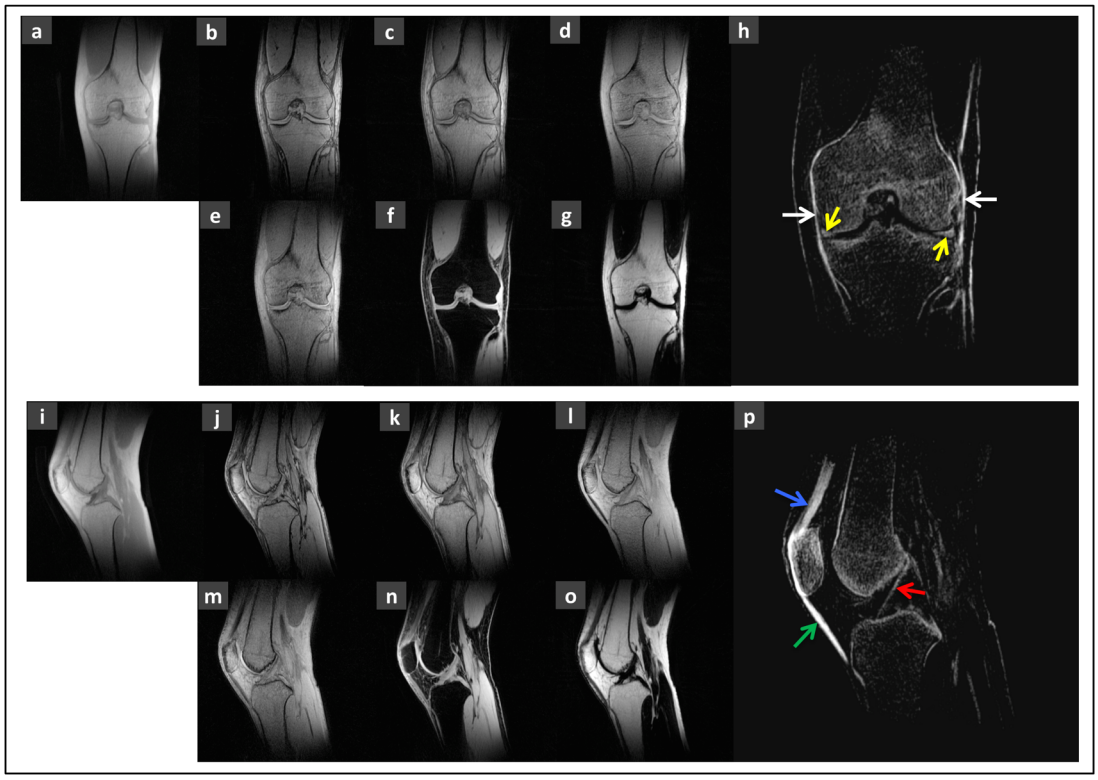

Figure 7. 8. In vivo knee experiment. Coronal slice of RHE images at TE of (a) 90µs, (b) 1502µs, (c) 1550µs, (d) 2900µs, (e) 2950µs, (f) water image, (g) fat image, (h) short T_2* image, sagittal slice of RHE images at TE of (i) 90µs, (j) 1502µs, (k) 1550µs, (l) 2900µs, (m) 2950µs, (n) water image, (o) fat image, and (p) short T_2* image. To separate water and fat image IDEAL was applied using 5 images at TE= 90µs, 1502µs, 1550µs, 2900µs, and 2950µs after image reconstruction. Short T_2* image was obtained by subtracting water and fat images from the RHE image at TE=90µs. Short T_2* tissues are clearly visible (white arrow: medial collateral ligament and lateral collateral ligament, yellow arrow: medial meniscus, blue arrow: quadriceps femoris tendon, green arrow: patellar ligament, red arrow: anterior cruciate).

detailed description of object with no slice selectivity artifact. RHE (Figure 7.7 (e)) shows higher detail and less noise (measured SNR=10.3) than FE-UTE (measured SNR=8.7) owing to the shorter per-excitation encoding time and the central k-space encoded by SPI (with TE equal to 90μs).

7.3.4 In vivo - knee imaging

Figure 7.8 shows coronal or sagittal slices of knee images at 5 different TEs obtained using RHE with multi echo imaging capability (Figure 7.8 (a),(b),(c),(d),(e),(i),(j),(k),(l),(m)), water images (Figure 7.8 (f),(n)) and fat images (Figure 7.8 (g),(o)) obtained using IDEAL, and the resultant short T_2* images (Figure 7.8 (h),(p)). Note that in short T_2* images, tissues such as bone, tendon, and ligament are visible with positive contrast. In the coronal plane short T_2* image (Figure 7.8 (h)) the medial collateral ligament and lateral collateral ligament (white arrow) and the medial meniscus (yellow arrow) are visible. In the sagittal plane short T_2* image (Figure 7.8 (p)), the quadriceps femoris tendon (blue arrow), patellar ligament (green arrow), and anterior cruciate ligament (red arrow) are seen clearly.

7.3.5 In vivo - brain imaging

Figure 7.9 shows brain images obtained by PETRA, FE-UTE, and RHE with two different RF pulse lengths and readout gradients (only for PETRA). The left 4x5 image matrix shows 2D slices selected from the reconstructed 3D images, and the right 4x5 image matrix shows the corresponding zoomed-in images. Figure 7.9 (a) to Figure 7.9 (j) show images at a mid-sagittal plane, while Figure 7.9 (k) to Figure 7.9 (t) show images at an axial plane. Figure 7.9 (a),(b),(c),(k),(l),(m) and Figure 7.9 (f),(g),(h),(p),(q),(r) show PETRA images obtained with 8μs and 24μs respectively. In PETRA with a short RF pulse (8μs), slice selectivity is suppressed owing to its broad excitation bandwidth, but SNR is reduced due to the smaller attainable flip

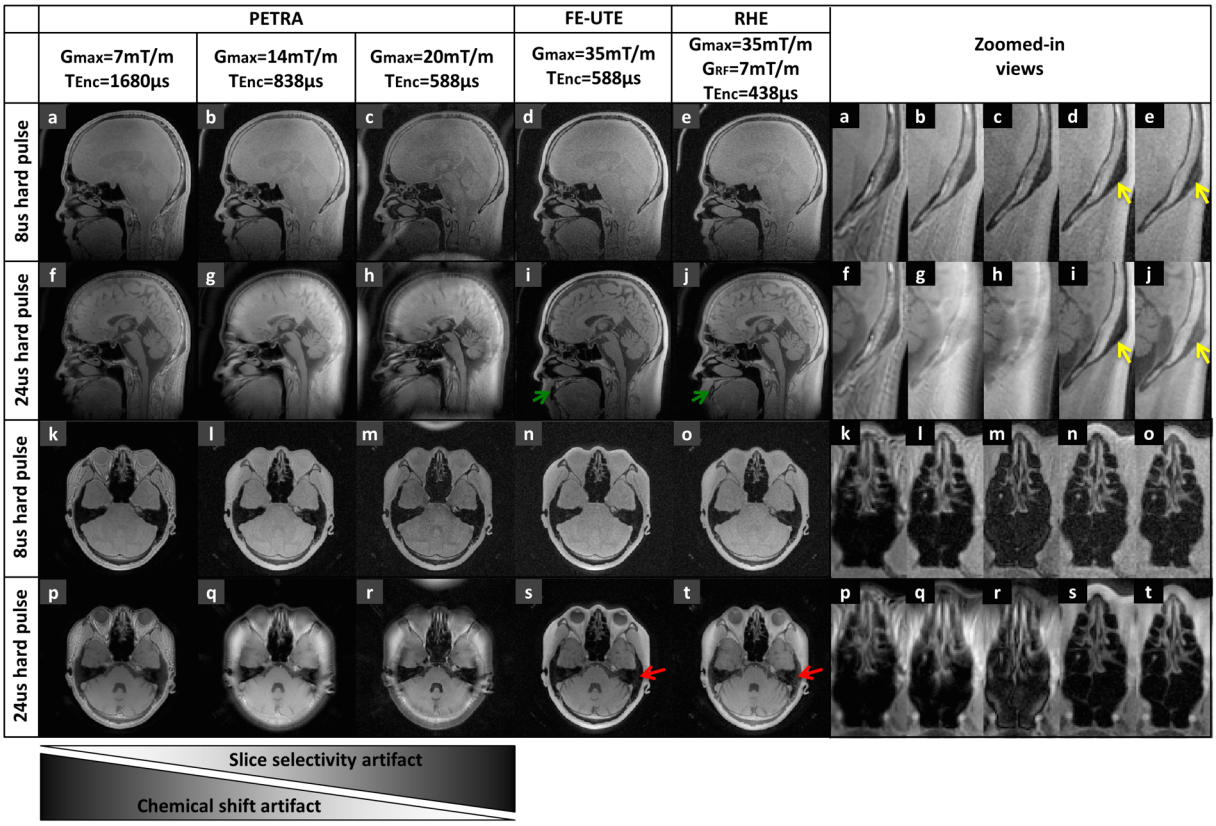

Figure 7. 9. In vivo brain experiment. Mid-sagittal plane image obtained by PETRA with 8µs RF pulse with (a) G_{max}=7mTm^{-1}, (b) G_{max}=14mTm^{-1}, (c) G_{max}=20mTm^{-1}, (d) UTE with 8µs RF pulse and G_{max}=35mTm^{-1}, (e) RHE with 8µs RF pulse, G_{RF}=7mTm^{-1}, and G_{max}=35mTm^{-1}, PETRA with 24µs RF pulse with (f) G_{max}=7mTm^{-1}, (g) G_{max}=14mTm^{-1}, (h) G_{max}=20mTm^{-1}, (i) UTE with 24µs RF pulse and G_{max}=35mTm^{-1}, (j) RHE with 24µs RF pulse, G_{RF}=7mTm^{-1}, and G_{max}=35mTm^{-1}, axial plane image obtained by PETRA with 8µs RF pulse with (k) G_{max}=7mTm^{-1}, (l) G_{max}=14mTm^{-1}, (m) G_{max}=20mTm^{-1}, (n) UTE with 8µs RF pulse and G_{max}=35mTm^{-1}, (o) RHE with 8µs RF pulse, G_{RF}=7mTm^{-1}, and G_{max}=35mTm^{-1}, PETRA with 24µs RF pulse with (p) G_{max}=7mTm^{-1}, (q) G_{max}=14mTm^{-1}, (r) G_{max}=20mTm^{-1}, (s) UTE with 24µs RF pulse and G_{max}=35mTm^{-1}, (t) RHE with 24µs RF pulse, G_{RF}=7mTm^{-1}, and G_{max}=35mTm^{-1}, and its corresponding zoomed-in images on the right. Note that in PETRA's slice selectivity increases and chemical shift artifact decreases as strength of readout gradient increases. By using a short RF pulse, the slice selectivity artifact can be alleviated, but SNR and T1 contrast are inevitably reduced due to the smaller attainable flip angle. Both FE-UTE and RHE shows better image quality with no chemical shift artifact and slice selectivity artifact, but RHE shows more signal intensity from compact bone structures than FE-UTE.

angle. Note that with an 8µs RF pulse, images are more proton density weighted, while with a longer RF pulse (24µs) increased T_1 weighting can be achieved. With the 24µs RF pulse, the

slice selectivity artifact is more noticeable in PETRA, substantially deteriorating with higher G_{max} (Figure 7.9 (g),(h),(q),(r)), while the chemical shift artifact is aggravated as encoding time decreases with lower G_{max} (Figure 7.9 (a),(f),(k),(p)).

Compared with PETRA, both FE-UTE (Figure 7.9 (d),(i),(n),(s)) and RHE (Figure 7.9 (e),(j),(o),(t)) show much better image quality with higher spatial resolution and no or minimal slice selectivity artifact respectively. However, as shown in the zoomed-in sagittal images of FE-UTE in Figure 7.9 (d),(i) and RHE in Figure 7.9 (e),(j), RHE exhibits higher signal intensity than FE-UTE in occipital bone indicated by the yellow arrow. In addition, RHE shows higher signal in a tooth as indicated by the green arrow in Figure 7.9 (i),(j). In axial images both RHE and FE-UTE show detailed views of the tissues in the sinuses as shown in zoomed-in images of Figure 7.9 (s),(t). Note that the red arrow indicates in Figure 7.9 (s),(t) RHE shows higher signal intensity than FE-UTE in the region where the meninges are visible.

Overall, among the UTE imaging schemes presented here, RHE shows the highest spatial resolution, best short T_2* contrast, no apparent chemical shift artifact owing to the shortest per-excitation encoding time, and well-controlled slice selectivity with a 8μs or 24μs RF pulse.

7.4 Discussion

In this chapter, we proposed a new scheme, termed RHE, for time-optimal per-excitation encoding in UTE imaging. While the TE in UTE imaging is conventionally reported as the beginning of the readout, reductions in encoding duration improve the spatial resolution for short T_2^* species[138] and reduce chemical shift artifacts. Moreover, the ability to control G_{RF} and the resultant slice selectivity allows greater flexibility regardless of the desired FOV for UTE imaging. While a high G_{RF} is desired to shorten encoding time, there exists an upper limit of G_{RF}

to avoid objectionable slice selectivity artifacts. Increasing the bandwidth of the RF pulse (e.g., using a shorter RF pulse) increases the attainable G_{RF} for good quality image; however, shorter RF pulses also limit the maximally attainable flip angle and thus can reduce SNR and/or desired T_1 image contrast.

The use of higher amplitude encoding gradient to attain faster encoding inevitably requires a larger SPI encoded region (N_{SPI}) for hybrid encoding techniques such as PETRA or RHE. As seen in Figure 7.5, increased N_{SPI} improves short T_2* imaging, with the caveat of substantially increasing total scan time. Reduction of N_{SPI} can harm spatial resolution for species where the T_2* is short relative to the per-excitation encoding duration (e.g., Figure 7.5-b, FE-UTE vs. RHE [N_{SPI}=29 or 40] with similar encoding durations). Therefore, it may be beneficial to prescribe RHE with a reasonably large N_{SPI} to balance between the beneficial qualities of a bigger SPI region and total imaging time. Note that the contribution of SPI encoding to spatial resolution may be more significant in the 1D simulation than 2D or 3D since 1D radial acquisition is more susceptible to T_2* decay than 2D or 3D radial acquisiton[138].

Due to a shorter encoding time, the sampling density along a radial spoke in the frequency encoded region is reduced in RHE compared to PETRA/ZTE, which penalizes the SNR for long T_2* components. However, in spite of the SNR advantage that slow encoding allows, longer encoding results in overall degradation in image quality (loss of spatial detail for short T_2* components and chemical shift artifacts). Thus, the reduced readout duration for RHE is important for improving image quality for UTE imaging. Indeed, there is no other encoding strategy to reach the extent of k-space in a more time-efficient manner than RHE when B_1 limitations prohibit the desired flip angle and field of view. If additional SNR is necessary, traditional techniques such as increased averaging or optimal coil configuration would apply.

Additional improvements in RHE image quality and functionality are possible. For example, post processing strategies proposed to correct slice selectivity in ZTE and PETRA[34,115,133] can be employed to alleviate blurriness artifacts. Moreover, hybrid encoding schemes with an oversampled SPI encoded region may allow reconstruction of images at multiple TEs in early encoding times, which can be used to estimate short T_2* parameters with a single experiment (e.g., using k-space extrapolation methods as recently proposed in single point electron paramagnetic resonance imaging[10]). The additional scanning time imposed by oversampling SPI encoded region can be reduced by using variable density sampling pattern and appropriate reconstruction method such as compressed sensing using k-space domain data[72,75] or model-based compressed sensing using k-space domain data and FID data (parameter domain) simultaneously[12,78].

Recently, there has been significant interest in developing sequences with extremely low acoustic noise levels[134,139–141]. Using RHE, the acoustic noise will be higher; however, the encoding duration will always be lower compared to B_1 limited PETRA/ZTE encoding strategies. Thus, quiet scanning may be incompatible with high quality imaging of short T_2* species. For RHE, lower noise scanning could be achieved at the cost of reduced encoding performance.

Gradient calibration is essential to avoid distortion and reconstruction errors in resultant images. In this study, we implemented a new gradient calibration method based on 1D SPI. Unlike other techniques, the method is not dependent upon 2D slice selection[99] or external hardware[97], and the identical pulse sequence can be used with very minimal modifications (only different encodings need to be obtained). The scanning time required for calibration is also very short (less than 5 seconds for the datasets herein), allowing robust estimation of k-space trajectory on a per-scan basis. This technique is also likely to be useful to measure the k-space

trajectory of other pulse sequences in MRI, and is only limited by the number of encoding single-point steps. This paper describes preliminary use of this new calibration technique, and further development is planned in future studies.

7.5 Conclusion

In summary, we have proposed a new encoding technique that allows flexible and time-optimal encoding for short T_2* species. In addition, we developed a new image-based calibration technique using single-point encoding to measure the k-space trajectory for improved image reconstruction.

Chapter 8. Rapid Dual Echo Ramped Hybrid Encoding-based Attenuation Correction

8.1 Introduction

Simultaneous PET/MR system has been recently developed to complement each individual imaging modality and obtain molecular-specific contrast with PET along with the rich anatomical information with MRI: for example, glucose metabolism (FDG in PET), anatomical information (T1W/T2W/PDW imaging in MRI), and tissue micro-structure (DWI in MRI). Moreover, functional imaging schemes such as functional MRI or cardiac/flow imaging in MRI recently have been studied in PET/MR system to benefit from the information from MRI as orthogonal biomarker for more accurate diagnosis. In spite of the promises and benefits in the simultaneous PET/MR imaging, it still remains challenging to obtain a reliable photon attenuation correction map necessary for accurate PET quantitation since proton is only imaged in MRI.

Many MR-based attenuation correction (MRAC) such as atlas registration-based or image segmentation-based method have been proposed to overcome the limitation. Atlas registration-based method is indirect estimation of CT contrast using patient database and fiducial MR images of the targeted subject [142–146]. The atlas registration method does not take the uniqueness of individual subject such as damage or deformation (e.g., hole or fracture in bone), and hence it can mislead the estimation of attenuation map. Image segmentation-based method allows more direct and precise estimation of CT contrast based on MR images with specialized imaging schemes or parameters (e.g., images acquired at different TEs to obtain fat and water separated images) [147–154]. However, it is still difficult to directly image bone due to MRI's

fundamental limitations in imaging short T2* species which has high photon attenuation relative to soft tissues.

It has been recently reported in literature that ultrashort echo time (UTE) or zero echo time (ZTE) imaging can be successfully used for MRAC owing to its capability to resolve objects with short T2* decay (i.e., bone)[114,155–158]. Unfortunately, UTE/ZTE techniques are not typically rapid (e.g., several minutes of acquisition time, particularly for multi-echo approaches), and are thus likely to impede PET/MR workflow (especially for whole body PET/MR where only 3-5 minutes may be available for MRI at each bed position).

In this study, we propose a new framework for MRAC based on dual echo ramped hybrid encoding (RHE) [13], where UTE and out-of-phase echo images with high spatial resolution ($1mm^3$) are obtained within a short acquisition time (35sec) in a single scan. The original RHE is modified as follows. First, a SLR half pulse with zero iso-delay is utilized to select a slab in S-I direction and hence reduce streaking and aliasing artifact due to undersampling radial spokes for fast imaging. Moreover, oversampled single point imaging (SPI) encoding is applied to allow reconstruction of multiple UTE images, which is used for more accurate air segmentation based on principal component analysis (PCA). With the multiple UTE images and an out-of-phase image, four species segmentation is performed to obtain bone, air, water, and fat component, where fat and water are estimated using a UTE image and out-of-phase image by 2-point Dixon method[159]. The segmented images are used to compose a pseudo CT image and the resultant attenuation map. In phantom experiments, the proposed imaging scheme was evaluated. In vivo experiment, an estimated pseudo CT map and the resultant PET image were compared with results obtained with actual CT image.

8.2 Methods

8.2.1 Data acquisition and image reconstruction

Figure 8.1(a) shows the pulse sequence diagram (PSD) of dual echo UTE imaging, which utilizes RHE to minimize per-excitation encoding time and alleviate blurriness of signal in short T2* object (bone in UTE-based MRAC). In RHE, frequency encoding is performed in center-out direction with fastest and largest encoding gradient turned on before RF coil deadtime (solid line in Figure 8.1(a)) to rapidly encode k-space (blue lines in Figure 8.1(b)). Cartesian SPI (dotted lines in Figure 8.1(a)) is used to encode central k-space missing in frequency encoding during RF

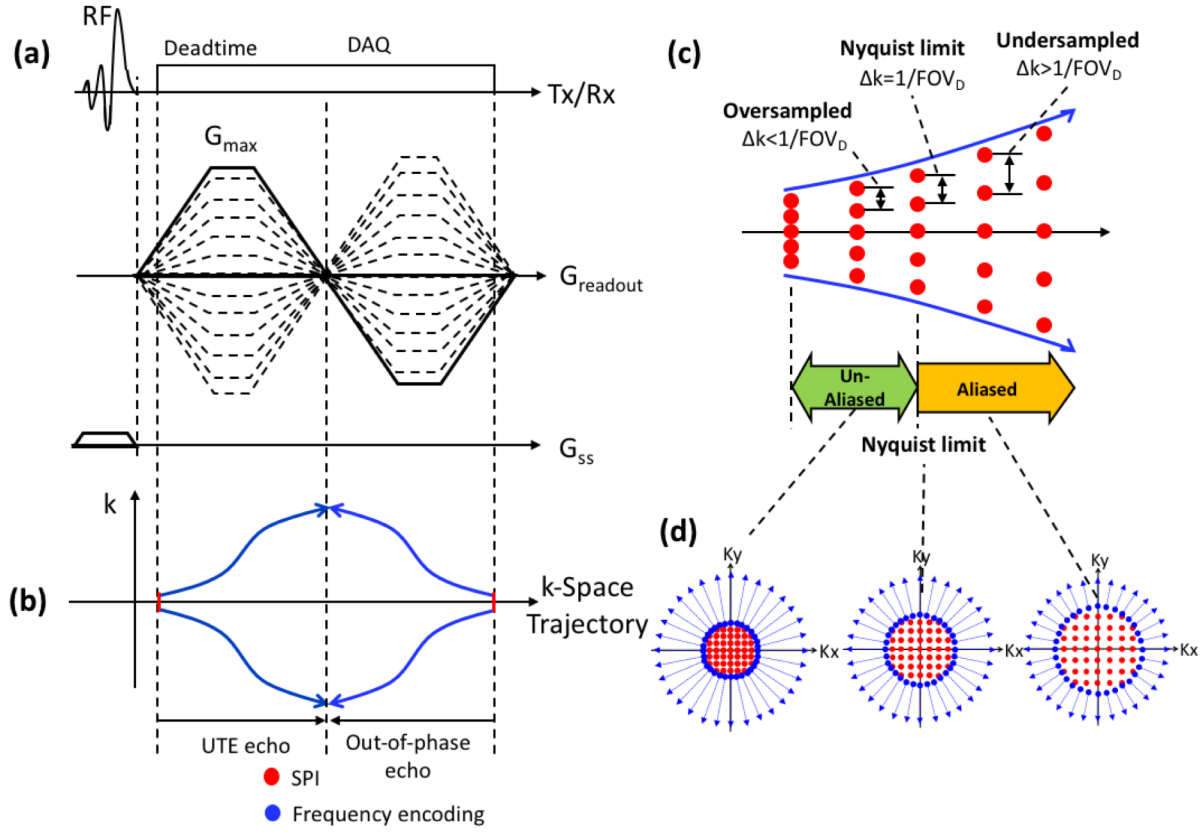

Figure 8. 1. Dual echo RHE imaging. (a) Pulse sequence diagram, (b) k-space trajectory, (c) oversampled SPIs in UTE, and (d) 2D examples of k-space trajectory in UTEs. Note that flying echo is utilized to acquire out-of-phase image around TE=1.1ms at 3T. By oversampling SPI multiple UTE images are obtained without aliasing artifact.

coil deadtime (red lines in Figure 8.1-b). In the proposed dual echo UTE acquisition, two symmetric encoding gradients are applied with opposite polarity, where UTE encoding is immediately followed by encoding of out-of-phase echo (TE = ~1.1ms at 3T), which enables fat and water separation based on 2-point Dixon reconstruction. Note that data acquired during flying-back to center of k-space are used to reconstruct out-of-phase image to reduce scan time. To attain proton density weightig, small flip angle is applied ($<2^{o}$).

Although RHE allows highly time-efficient encoding by acquiring k-space data while ramping up and down the encoding gradients, strong eddy current effect generated by rapidly changing gradients may result in distortion of gradients that deviates k-space trajectory from nominal trajectory, resulting in imaging artifacts such as blurring, ringing, scaling, and phase error. Therefore, it is crucial to consider the gradient distortion caused by eddy current when calculating k-space trajectory for artifact-free image reconstruction. In this study, dynamic SPI-based gradient measurement technique was used to estimate actual k-space trajectory[25].

In the proposed dual echo UTE acquisition, the original RHE in the literature is further modified to incorporate a SLR half pulse with zero iso-delay to enable slab selection in S-I direction to alleviate radial streaking and aliasing artifact in reconstructed image, which is desired in the proposed fast imaging scheme performed with undersampled radial spokes and strong readout gradient with high maximum amplitude, Gmax. Moreover, oversampled SPI was applied to allow reconstruction of multiple UTE images. Figure 8.1(c) delineates time-spreading k-space sampling position in dynamic SPI (SPIs consecutively encoded over TEs). If SPI is oversampled at the first TE after RF coil deadtime, multiple un-aliased SPI data can be acquired at its following TEs until the k-space data gets to Nyquist limit ($\Delta k=1/FOV_D$, where FOV_D is a desired FOV). Figure 8.1(d) shows a 2D example of the acquisition of multiple k-spaces using

the oversampled, dynamic SPI. The multiple UTE images are utilized in two ways. First, the UTE images are averaged to yield one image with higher SNR, which is used for initial segmentation of bone and air. Second, pixelwise time course (temporal data) of the UTE images is used to realized more reliable segmentation of air, which will be explained in the following sections.

8.2.2 Bias correction

MR image is often biased by several factors such as B1 inhomogeneity resulting in uneven excitation of spins or discrepant coil sensitivity for signal reception between channels. This spatial bias can be modeled as a bias map multiplied to the ideal as following equation.

$$M'_{xy}(x,y,z) = s(x,y,z)M_{xy}(x,y,z) \tag{8.1}$$

,where M'_{xy} is a biased transverse magnetization, M_{xy} is unbiased ideal transverse magnetization, and $s(x,y,z)$ is a bias map.

In this study a pixelwise bias correction method was implemented ahead of segmentation, where DC bias for each pixel is estimated in the inversed (negative) log of magnitude of image, $\mathrm{I'_{InvLog}}$, as shown in equation 8.2, which can be directly converted to bias correction map in image domain.

$$\mathrm{I'_{InvLog}} = -\ln\left(\left|M'_{xy}(x,y,z)\right|\right) = -\ln\left(s(x,y,z)\right) - \ln\left(\left|M_{xy}(x,y,z)\right|\right) = DC + \mathrm{I_{InvLog}} \tag{8.2}$$

, where $\mathrm{I_{InvLog}}$ is unbiased inversed log image, and DC is an estimated bias in inversed log domain. Once a bias image, DC, is estimated, it can be directly converted to the bias correction map, 1/s(x,y,z) by taking exponential.

Figure 8.2 delineates the proposed method for bias estimation. First, a targeted image (Figure 8.2(a)) is converted to the inversed log image (Figure 8.2(b)). Then, a 3D ROI is used to select neighboring pixels in an inversed log image (Figure 8.2(c)). Within the ROI, pixels containing soft tissue is first roughly selected based on the histogram (Figure 8.2(d)) of all pixels to exclude air (Figure 8.2(e)), and then the median of the selected pixels are determined as DC (Figure 8.2(f)). The estimated bias correction map is converted to the image domain (Figure 8.2(g)) and then applied to the targeted image (Figure 8.2(h)). Since in this intensity based bias correction a more proton density weighted image with less soft-tissue contrast is more desired, a UTE image is used to estimate the bias correction map in the UTE image itself and other gradient echo images.

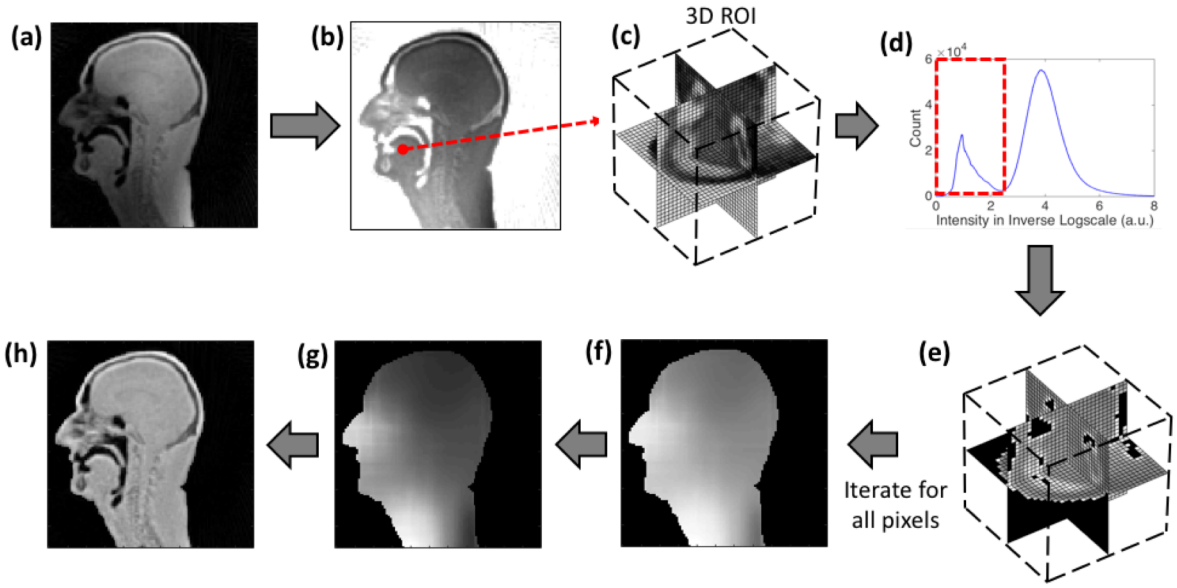

Figure 8. 2. Bias correction. (a) Targeted UTE image, (b) Inversed log image, (c) 3D ROI, (d) soft tissue selection based on histogram, (e) soft tissue pixels, (f) estimated bias map in inversed log domain, (g) estimated bias map in intensity domain, and (h) bias corrected UTE image. Intensity-based DC-bias correction is performed with 3D ROI, where the ROI includes pixels surrounding a target pixel. A median of intensity of soft tissues is determined as DC bias.

8.2.3 Modeling tissue distributions

In proton density weighted UTE image, it is expected that pixel intensity for air (noise) is darkest, that of soft tissue is brightest, and bone shows intermediate intensity. Thresholds to initially segment air, bone, and soft tissue are determined based on histogram of magnitude of an averaged UTE image with bias correction as explained above. The distribution of air (noise) is first approximated to Gaussian distribution as following equation, which is valid assumption when SNR is high (larger than 2) [160].

$$f(x) = \frac{k}{2\pi\sigma} \exp\left[-\frac{(x-\mu)^2}{2\sigma^2}\right] \tag{8.3}$$

, where k is a scaling factor to compensate for scale difference between the probability density function and histogram, x is intensity of pixel, and σ and μ are respectively standard deviation and mean. The distribution of soft tissue is difficult to model as a single Gaussian curve since it is composed of different types of tissue with different contrasts depending on the imaging scheme and subject. For example, in this study a proton density weighted image is obtained where white matter exhibits slightly darker intensity than gray matter in brain. Moreover, imperfect bias-correction or image reconstruction can also deviate the distribution from Gaussian. Therefore, a non-Gaussian distribution was used to fit the histogram for soft tissue. Gaussian, logistic, and hyperbolic distribution respectively with excess kurtosis=0, 1.2, and 2 were tested on the data acquired in the proposed method to empirically choose the best model, and logistic distribution was selected as best model, using the following equation.

$$f(x) = \frac{ke^{-\frac{x-\mu}{s}}}{s\left(1+e^{-\frac{x-\mu}{s}}\right)^2} \tag{8.4}$$

, where k is a scaling factor to compensate for scale difference between the probability density function and histogram, x is intensity of pixel, μ is mean, and variance can be calculated as $\frac{s^2\pi^2}{3}$. Bone distribution is indirectly estimated by subtracting the total histogram by the estimated air and soft tissue distribution. Figure 8.3(a) shows an example of total histogram in object, which is a mixture of air, bone, and soft tissue. Figure 8.3(b) and (c) illustrates estimation of air/soft tissue distributions, and the resultant bone distribution, respectively.

8.2.4 Threshold setup

Parameters of the estimated Gaussian distribution is used to determine a threshold for air

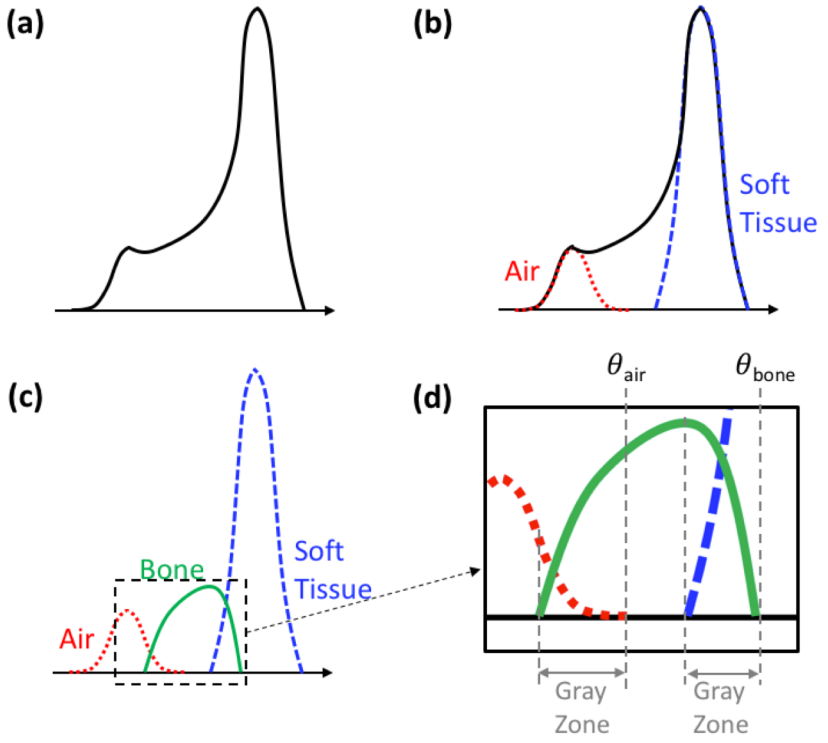

Figure 8. 3. Modeling tissue distribution. (a) Total histogram, (b) estimation of air and soft tissue distributions. (c) estimation of bone distribution, and (d) thresholds set up. Bone distribution is indirectly obtained using the estimated air and soft tissue distributions.

detection, θ_{air}, as following equation.

$$\theta_{air} = \mu_{air} + 6\sigma_{air} \tag{8.5}$$

,where μ_{air} and σ_{air} are estimated mean and standard deviation of the estimated air distribution, respectively. Note that θ_{air} is loosely set to embrace the gray zone between air and bone, which will be resolved in the following air detection using multiple UTE images based on PCA.

The threshold for bone detection, θ_{bone}, is set to the intensity at right zero-crossing point of the estimated bone distribution as shown in Figure 8.3(d). The gray zone between bone and soft tissue will be resolved in refinement step using edge information explained in the later section.

8.2.5 Air detection

Pixels with intensity less than θ_{air} are initially segmented as air pixels. Then, pixelwise temporal data in multiple UTE images are utilized to refine air from the gray zone between air and bone where air and bone pixels exhibit similar pixel intensity. Note the temporal data does not contain physically meaningful information (i.e., T2* or M_0) due to the narrow range of TE (<30μs) that is highly susceptible to local noise. In this study, PCA-based data analysis is performed to analyze and parameterize the temporal data and thereby find correlation that can be used for refinement of the air map. First, pixels with intensity less than μ_{air} is classified to a trust air set, which contains air pixels detected with high possibility. Let's denote 3D pixel coordinates for the pixels in the trust set as 3D vectors, $X_1, X_2, \dots, X_R$, where R is cardinality of the trust set. Then, a training matrix is composed as following.

$$\mathrm{A} = \begin{bmatrix} I(X_1, t_1) & \cdots & I(X_1, t_T) \\ \vdots & \ddots & \vdots \\ I(X_R, t_1) & \cdots & I(X_R, t_T) \end{bmatrix} \tag{8.6}$$

, where I(x,t) denotes pixels intensity at pixel coordinate x and TE=t, and t_1, t_2, .., and t_T denote TEs of T UTE images. The matrix A is eigenvalue decomposed, and the eigenvectors with two largest eigenvalues, V_1 and V_2, are used to compress pixelwise temporal data. Temporal data at the initially segmented air pixel is projected onto each eigenvector to obtain two parameters, c1 and c2, corresponding to two eigenvectors, V_1 and V_2. Then, the estimated parameters are used to determine whether a targeted pixel is air or not. In the experiments, correlation was shown between c1 and air tissue, and between c2 and air/tissue interface. Based on the empirical observation, c1 map and c2 map are separately thresholded and combined to make an air refinement map. The air refinement map is processed with morphologic image processing methods (closing and dilation operation), and then initially segmented air map is refined by multiplying the obtained air refinement map.

8.2.6 Bone detection

In initial segmentation of bone, pixels with intensity smaller than θ_{bone} are classified as bone, excluding the pixels classified as air in the preceding air detection and refinement stage. After initial segmentation of bone, mis-classified bone pixels in the gray zone between bone and soft tissue are removed using edge information of a UTE image. First, an edge image is obtained using Canny edge detection, where 2D edge detection is performed in three slice direction and combined by logical summation. A refinement map for bone detection is obtained by applying dilation process with a spherical structure element with radius=4, in the assumption that bone resides near strong edges. Then, the initial bone segmentation is refined by multiplying the obtained refinement map.

8.2.7 Generation of pseudo CT map

Pseudo CT map is generated using the detected bone map, air map, and fat/water separated images. First, a CT map for soft tissue is generated based water fraction as follows.

$$CT_{softTissue} = \frac{I_{water}}{I_{water}+I_{fat}} \left(HU_{water} - HU_{fat}\right) + HU_{fat} \tag{8.7}$$

, where I_{water} and I_{fat} are water and fat separated images, and HU_{water} and HU_{fat} are Hounsfield unit in CT for water and fat, respectively. Then, CT map for bone is generated using the detected bone map.

$$CT_{bone} = BW_{bone}\, HU_{bone} \tag{8.8}$$

, where BW_{bone} is a binary map of the detected bone, and HU_{bone} is Hounsfield unit of bone at the desired body part. CT map for air is obtained as following.

$$CT_{air} = BW_{air} HU_{air} \tag{8.9}$$

, where BW_{air} is a binary map of the detected air, and HU_{air} is Hounsfield unit of air in CT. Finally, a pseudo CT map is generated using the three CT maps for soft tissue, bone, and air as following equation.

$$CT_{MRAC} = (1 - BW_{bone} - BW_{air})\, CT_{softTissue} + CT_{bone} + CT_{air.} \tag{8.10}$$

8.2.8 Experimental setup

To evaluate the proposed method, phantom and in vivo experiments were performed using a 40-channel HNU coil in a 3T PET/MR system (GE Healthcare, Waukesha, WI, USA). Imaging parameters are as follows: Gmax=33mT/m, slewrate=118mT/m/ms, FOV=300mm^3, voxel size=1mm^3, TR=4.2ms TE=52/54/56/58/60/62/64/66/68/70/72/74/76/78/1172μs (note that

multiple UTE images are obtained at every 2μs), scantime=35sec, sampling bandwidth=250Hz, FA=1°, # of radial spokes=7442, and # of SPI encoding=925.

In phantom experiment, data acquisition and image reconstruction for the proposed MRAC were tested with two different subjects: GE provided water phantoms and a custom-made MRAC phantom. In the experiment with water phantom, four phantoms were placed on MR table as shown in Figure 8.4(a) to mimic human subject in size and test how streaking artifacts are exhibited with different slab selection. Four different cases were tested: no slab selection (using non-selective 8μs hard pulse), slab selection (using 628μs SLR-half pulse) with slab size of 460mm, 346mm, and 269mm. For the experiment with UW-MRAC phantom, a container

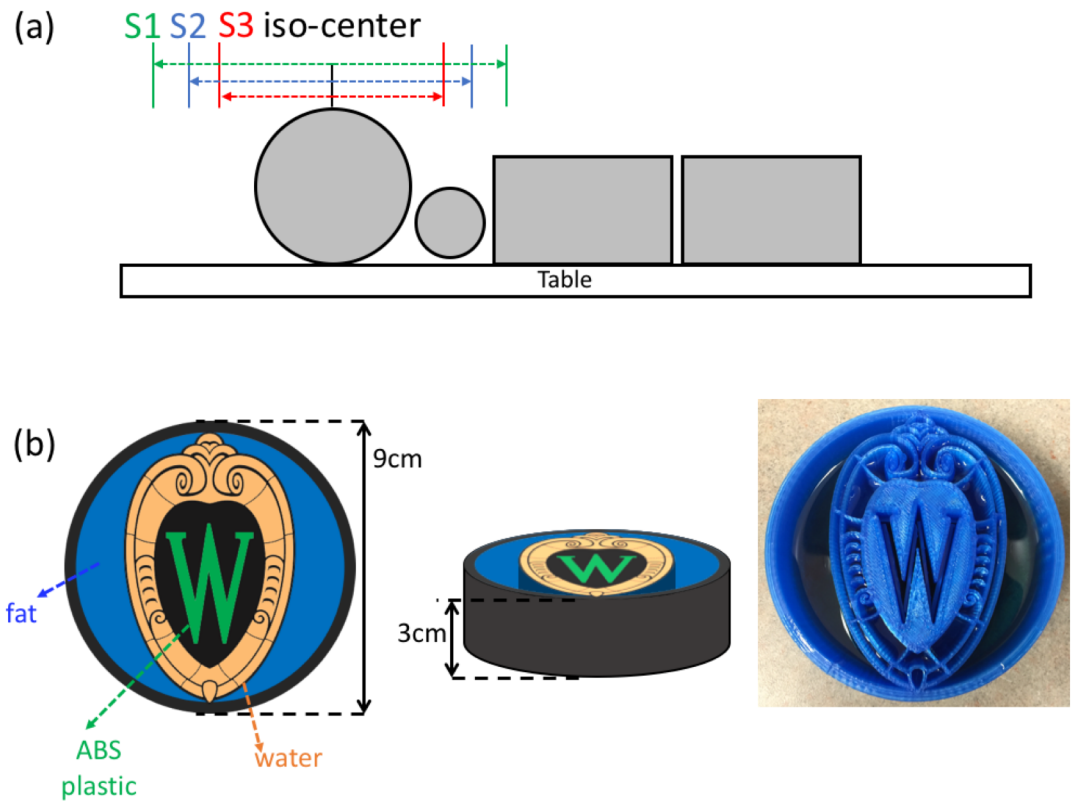

Figure 8. 4. Phantom experiments. (a) Water phantoms, and (b) a custom-made UW-MRAC phantom.

made of PLA-plastic was manufactured by using a 2D crest of University of Wisconsin as illustrated in Figure 8.4(b). The 3D object was made by a 3D printer. Fat, water, and ABS plastic were filled in the container as shown in Figure 8.4(b). In vivo experiment, brain imaging was performed with a healthy volunteer in compliance with IRB.

In image reconstruction, a convolution gridding was applied with kernel size=5, oversampling ratio=2. After image reconstruction, fat and water separated images were obtained based on a 2-point Dixon reconstruction using the GE Healthcare Orchestra SDK. In bias correction, a 3D ROI = 31x31x31 was used.

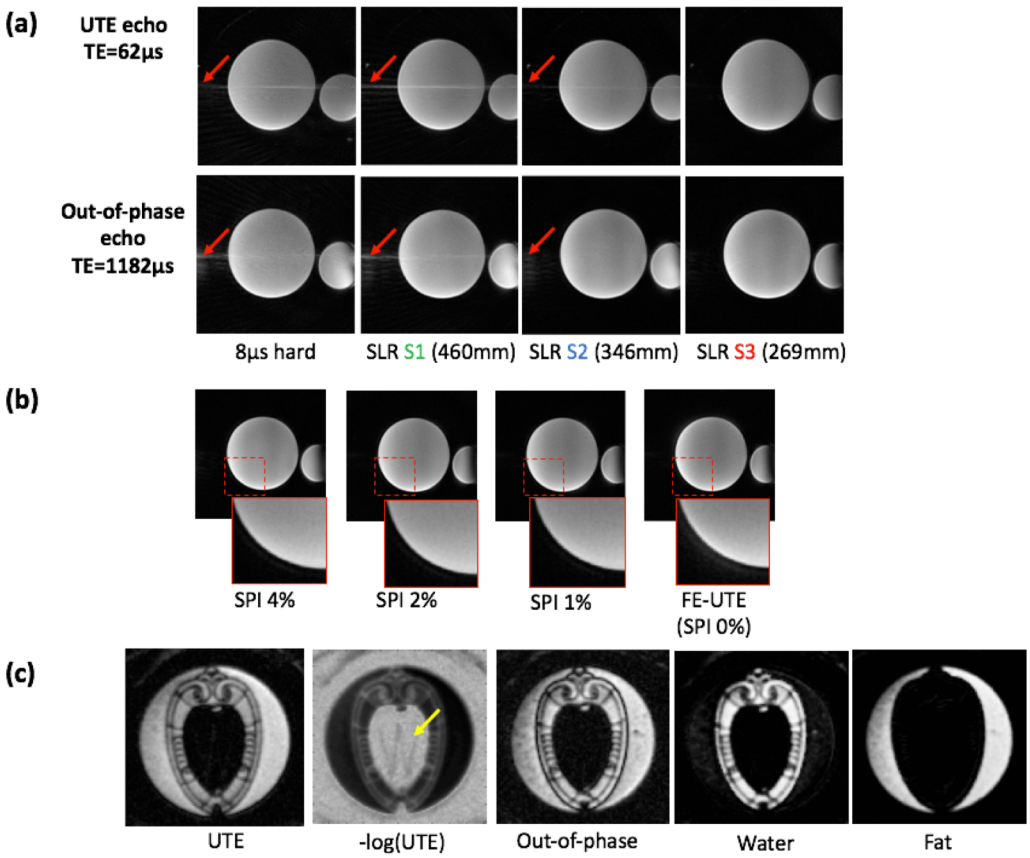

Figure 8. 5. Results of phantom experiments. (a) UTE and out-of-phase images with different slab selection, (b) out-of-phase image reconstructed with different size of SPI, (c) results with UW-MRAC phantom. Three different slab size were tested (S1=460mm, S2=346mm, S3=269mm) in (a), where smallest slab size (S3) showed best image without aliasing/streaking artifact in S-I direction.

8.3 Results

8.3.1 Phantom experiment

Figure 8.5(a) shows that aliasing/streaking artifact in the S-I direction is suppressed by utilizing slab selection. The image using 8μs hard pulse or larger slab selection exhibits stronger streaking artifact due to the strong readout gradients utilized and the undersampled number of radial spokes necessary for fast imaging. Therefore, it is appropriate to use a selective SLR half pulse with small slab matched the S-I coverage of the PET detector (~25cm). Figure 8.5(b)

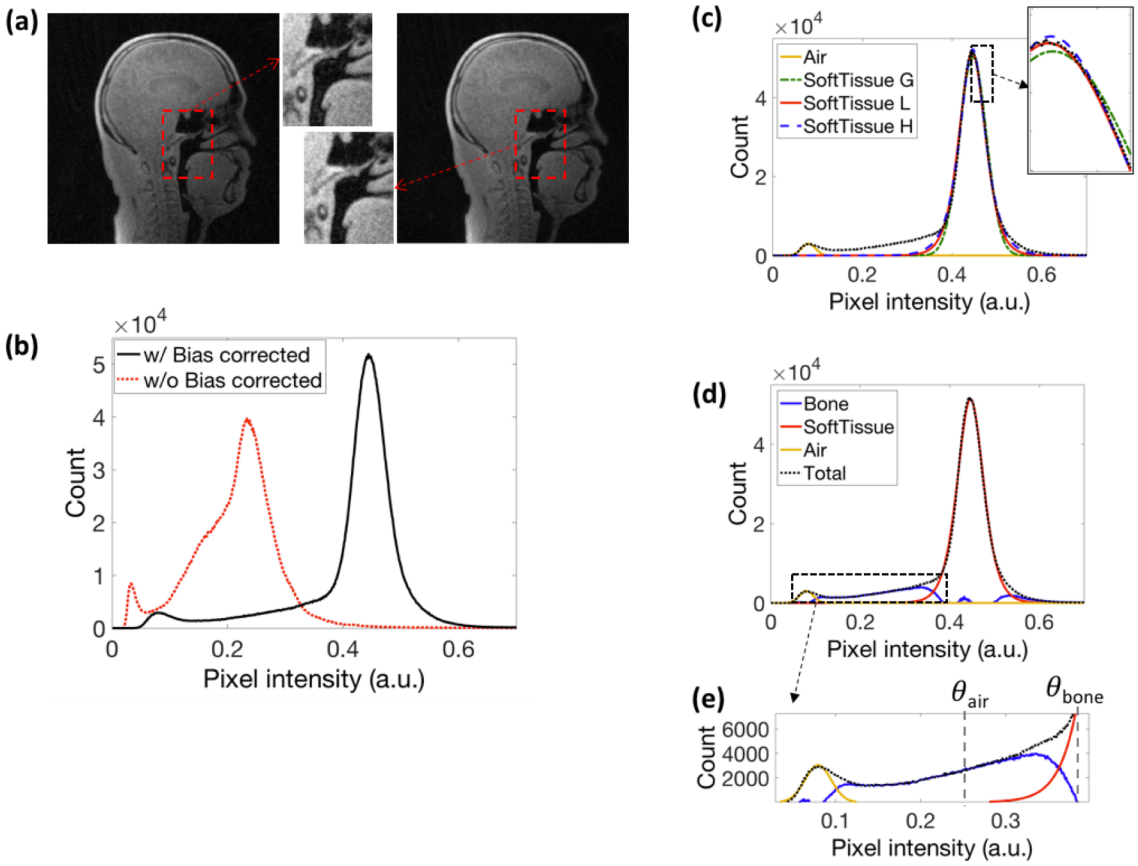

Figure 8. 6. A UTE image and histogram. (a) A UTE image vs. averaged UTE image, (b) histogram w/o and w/ bias correction, (c) distribution models for soft tissue, (d) estimation of bone distribution, and (e) threshold setup. Note that in (a) SNR in air region is noticeably improved. In (c) SoftTissue G, L H denotes fitted curve with Gaussian, logistic, and hyperbolic distribution.

shows the efficacy of hybrid encoding in reducing the ringing artifact in the image acquired during the flying-back echo (out-of-phase image), owing to SPI encoded central k-space that is more robust to error in k-space trajectory than frequency encoding based UTE (FE-UTE).

Figure 8.5(c) shows the results with UW-MRAC phantom, where a UTE image at TE=52μs, an out-of-phase image at TE=1172μs, and the resultant water and fat image are shown. Note that in the UTE image, signal in short T2* component, ABS plastic (T2* = ~500μs), is visible (indicated by yellow arrow in inversed log image), which is distinct from air region in background, implying that the proposed method is capable of resolving bone required in MRAC. Moreover, water and fat were successfully separated by 2-point Dixon reconstruction using the given UTE image and out-of-phase image.

8.3.2 In vivo - bias correction and histogram

Figure 8.6(a) shows a UTE image at TE = 52μs and an averaged UTE image using 14 different TEs obtained in imaging with a healthy volunteer. SNR was calculated using two region approach where a ROI for signal was set inside brain and a ROI for noise was set outside object. The calculated SNR was 34.8 and 37.2 respectively for the UTE image without and with averaging, where the averaged image showed slightly higher SNR. The effect of increased SNR is shown in the zoomed-in images in Figure 8.6(a), which shows that air segmentation can benefit from averaging UTE images. Figure 8.6(b) shows histograms of the averaged UTE image without and with application of bias correction, normalized by its maximum intensity. As seen, bias correction stretches the distribution of tissue intensity, which makes gray zone smaller, and makes it easier to fit the distribution with a simpler model such as Gaussian distribution.

In Figure 8.6(c), a black dotted line shows total histogram from the bias corrected UTE image. Air distribution was fitted using Gaussian model, and the soft tissue distribution was fitted with three different probability models with different kurtosis: Gaussian, Logistic, and Hyperbolic. Logistic model showed the best fit for the soft tissue region in the histogram as shown in the zoomed-in view, and hence it was used to fit the soft tissue distribution. Figure 8.6(d) shows the estimated bone distribution, which was obtained by subtracting the total histogram by the estimated air and soft tissue distribution. Figure 8.6(e) shows the zoomed-in

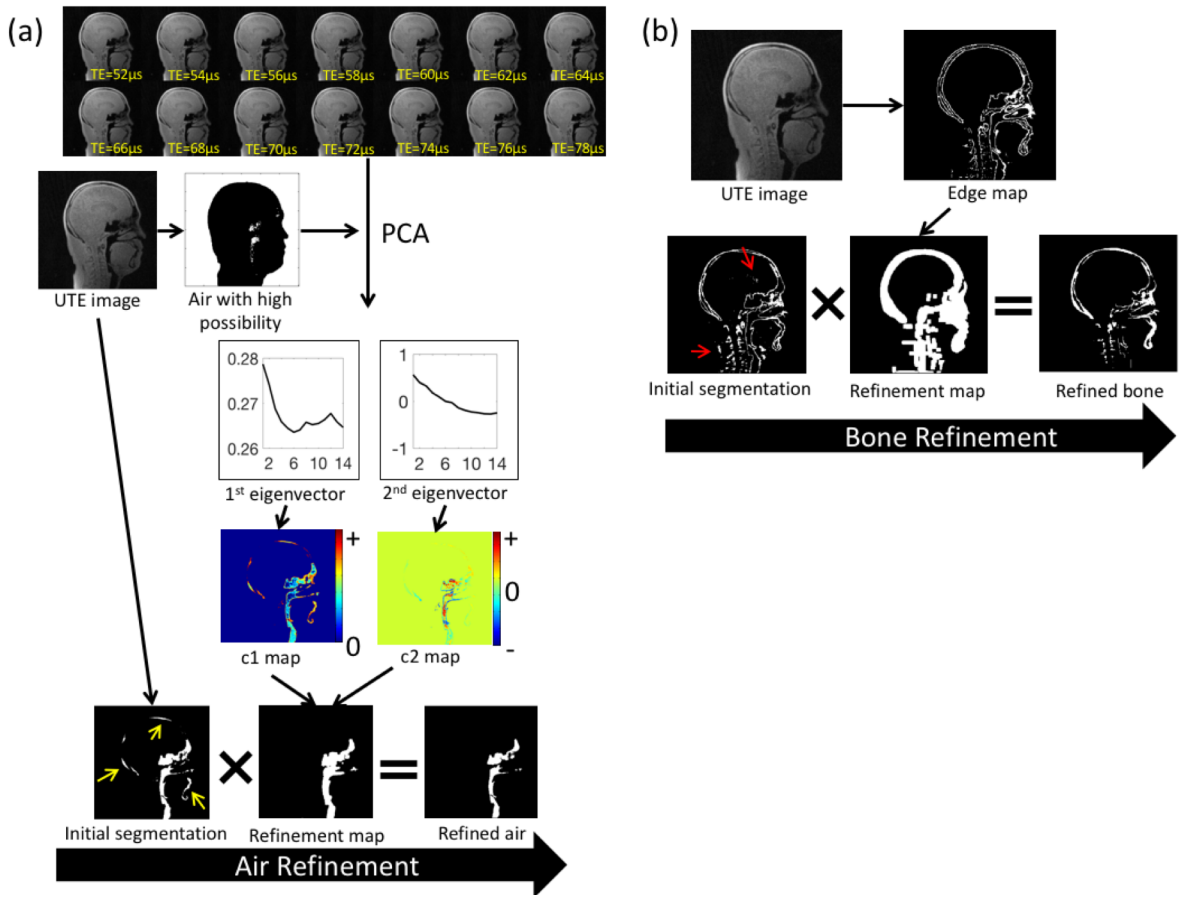

Figure 8. 7. Air/bone detection. (a) Air refinement, and (b) bone refinement. In air refinement, PCA is used to parameterize 14 UTE images, where c1 map exhibiting DC component shows strong correlation. In bone refinement canny edge detection is used to obtain a refinement map.

view around air and bone distribution and thresholds set for initial segmentation of air and bone. θ_{air} was set to 0.262, and θ_{bone} was set to 0.386.

8.3.3 In vivo – Air/bone detection

Figure 8.7(a) shows the initial segmentation and refinement of air based on PCA. The two eigenvalues were 3.85 x 10^{16} and 1.34 x 10^{14}. Note that c1 map shows strong correlation with air pixel where low c1 value tends to indicate air, while c2 map shows relatively weaker correlation where high absolute c2 value tends to indicate air or air/soft tissue interface, and c2 value near zero tends to indicate bone. Based on the observation, pixels with c1 below 70% of maximum value of c1's in the trust air set (obtained by projecting temporal data in trust set to V_1) were included in a refinement map. In addition, pixels with c2 above 70% of maximum or below 70% of minimum value of c2's in the trust air set were included the refinement map. Then, the refinement map was applied with closing and dilation operation to yield a final refinement map with noise removed as shown in Figure 8.7(a). With the refinement process, falsely detected air in vicinity of occipital bone and jaw bone as indicated by yellow arrows were removed. Figure 8.7(b) shows the initial segmentation and refinement of bone. An edge map obtained by canny edge detection was dilated to yield refinement map. In the refined bone map, falsely detected bone in soft tissue indicated by red arrows were clearly removed.

8.3.4 In vivo - Pseudo CT

Figure 8.8 shows six 2D slices in a UTE image obtained by averaging 14 UTE images without and with application of bias correction (Figure 8.8-(a),(b)), an out-of-phase echo image at TE=1172μs (Figure 8.8-(c)), a water and fat image (Figure 8.8-(d),(e)), a segmented air and bone (Figure 8.8-(f),(g)) and the resultant pseudo CT image (Figure 8.8-(h)).

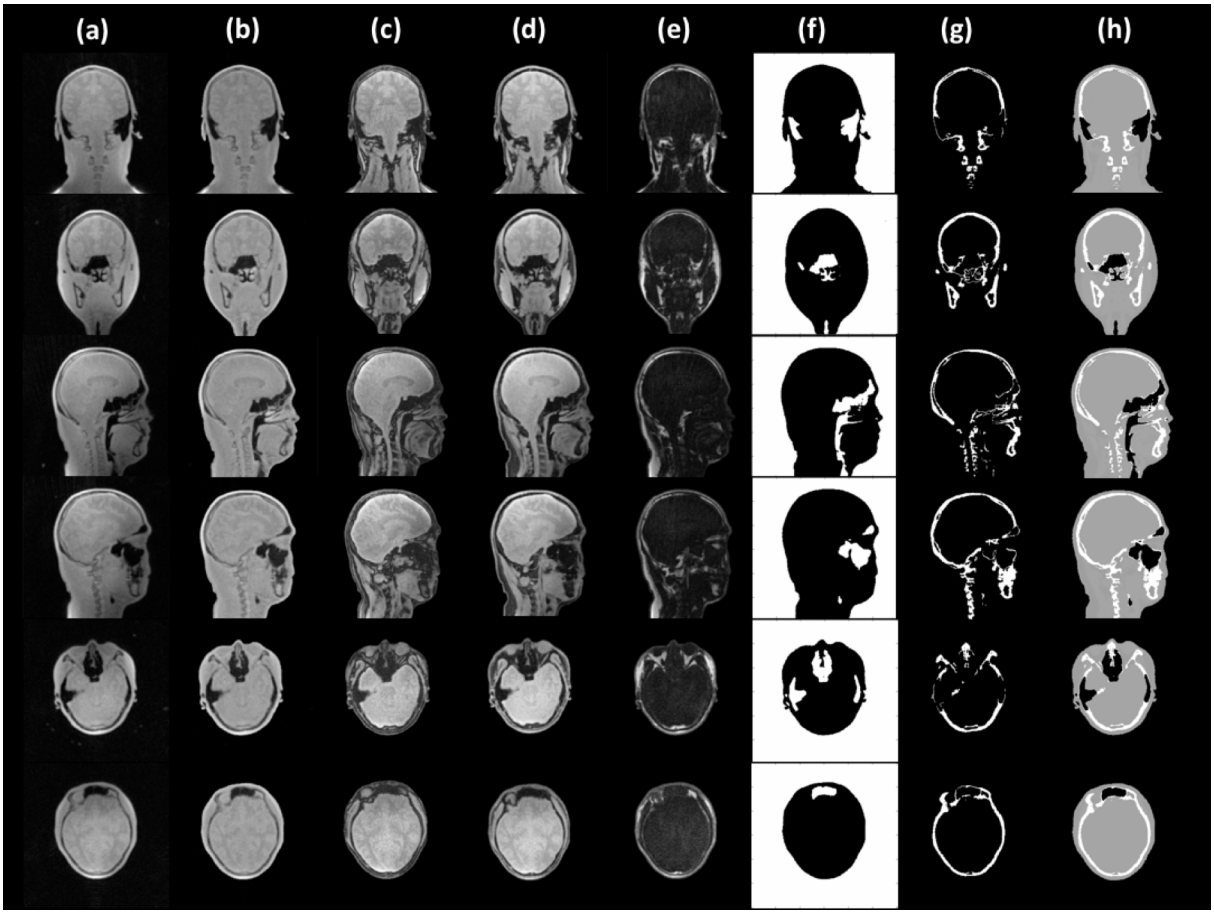

Figure 8. 8. Pseudo CT image. Six 2D slices of (a) a UTE image without bias correction, (b) a UTE image with bias correction, (c) an out-of-echo image, (d) a water image, (e) a fat image, (f) a segmented air, (g) a segmented bone, and (h) a composed CT image.

8.4 Discussion

In this study, we proposed a new framework for UTE based MRAC that allows high resolution imaging (1mm spatial resolution) of UTE and out-of-phase images with clinically feasible scan time (35sec), utilizing RHE. We have shown the feasibility in head imaging herein, but it will be more beneficial to use this framework for simultaneous whole body PET/MR imaging where several MRAC imaging should be performed for each stations. For example, imaging with 4 different stations will require total 2min 20sec scan time with the proposed

MRAC, which is still considered as feasible scan time compared to 11min 32sec total scan time required in ZTE based MRAC with lower spatial resolution (1.35mm spatial resolution)[114]. Moreover, the proposed method does not require additional fat/water imaging (Dixon or IDEAL) owing to the dual echo acquisition where in-phase (UTE) and out-of-phase images are obtained.

There are two possible ways to reduce total scan time: reduction in the length of a TR and the number of TRs. To reduce the length of TR, we have designed the dual echo UTE pulse sequence base on RHE, where UTE echo and its following out-of-phase echo (around 1.1ms) are acquired in one TR, which reduces the length of pulse sequence by 60 % than the radial 2 point Dixon acquisition in conventional way that acquires two echoes at around 1.1ms and 2.2ms in 3T, not utilizing UTE as in-phase echo. To further reduce the length of sequence, a flying-back echo was acquired, which is 33% reduction in length of pulse sequence compared with the case of using conventional center-out echo. Moreover, the design of rapid pulse sequence benefits from RHE with fast slewrate and high Gmax, which minimizes readout duration. To reduce the number of TR, radial spokes were undersampled. To alleviate streaking/aliasing artifact that can be cause by undersampled radial spokes and fast readout (high readout bandwidth), slab selection was applied using a SLR-half pulse with zero iso-delay, and we have shown the efficacy.

The proposed MRAC utilizes RHE, where SPI is used to encode central k-space. Since SPI encoding is more robust to error in k-space trajectory, we were able to reconstruct image with the data acquired during flying-in with alleviated imaging artifacts. Moreover, slightly oversampling SPI encoding enabled dynamic SPI in which consecutive SPI images are acquired [10,25] to acquire multiple UTE images between TE=52μs and 78μs, which was used to increase SNR in a UTE image. In addition, the pixelwise temporal data in the multiple UTE images was used in PCA-based air refinement to resolve pixels in gray zone between air and bone. PCA is

one of many possible approaches to parameterize the temporal data (e.g., polynomial fitting), but we have shown that the estimated parameters are correlated with air pixel. More efficient method to utilize the temporal data will be explored in future works. Moreover, parallel imaging[161] or compressed sensing[12] can be used to accelerate SPI encoding or increase sampling density of SPI encoding to secure more UTE images.

8.5 Conclusions

In this study we have proposed a rapid RHE-based MRAC method that benefits from RHE and optimized 2-point Dixon encoding. The utilization of a slice selective 3D RHE acquisition improves image quality, while still allowing fast image acquisition. While is also possible to accelerate MRAC by reducing voxel size, the partial volume complicates image-based segmentation techniques. Imaging with a flying-back echo is usually considered to be technically demanding in radial sampling and is not routinely performed. However, with the use of the RHE acquisition (hybrid encoding of central k-space) and robust gradient waveform measurement, it was possible to acquire an out-of-echo in good imaging quality. Such acquisitions are expected to be highly useful for MRAC acquisitions to improve quantitative accuracy in PET/MR.

Chapter 9. Highly Efficient Bi-Component T2* Mapping of the Knee using Ultra-short Echo Ramped Hybrid Encoding

9.1 Introduction

Quantitative imaging based on T1/T2/T2* parameter has been explored in muscular-skeletal (MSK) MRI as a clinically meaningful tool to characterize lesion in tendon, meniscus, and cartilage. In reality, a voxel in MRI can contain multiple component due to the limited spatial resolution, causing partial volume effect. Therefore, single component fitting can lead wrong result in clinic. The use of bi-component imaging and reconstruction methods can improve the specificity of T2* analysis of musculoskeletal tissues with multiple water components.

With recent development of high performance gradient system, ultrashort echo time (UTE) imaging has become feasible, allowing more robust multi-component T2* estimation by acquiring images in earlier TEs. In literature UTE-based bi-component T2* mapping techniques have been used to evaluate cartilage, tendon, meniscus, ligament, and cortical bone[162–165]. However, long acquisition times (15~20min) to obtain multiple images (typically more than 16) required for bi-component fitting, limited anatomic coverage, and image artifacts associated with current techniques have reduced the feasibility of bi-component T2* analysis in clinical studies.

In this study, we explore the feasibility of a rapid UTE imaging method based on ramped hybrid encoding (RHE) to provide reliable bi-component T2* analysis of the human knee joint at 3T. In the proposed method, total 17 images are acquired in a single scan, where a UTE echo is followed by 16 gradient echoes. To compensate for eddy current effects, the k-Space trajectory was measured using a dynamic SPI-based gradient measurement technique[25], which is essential

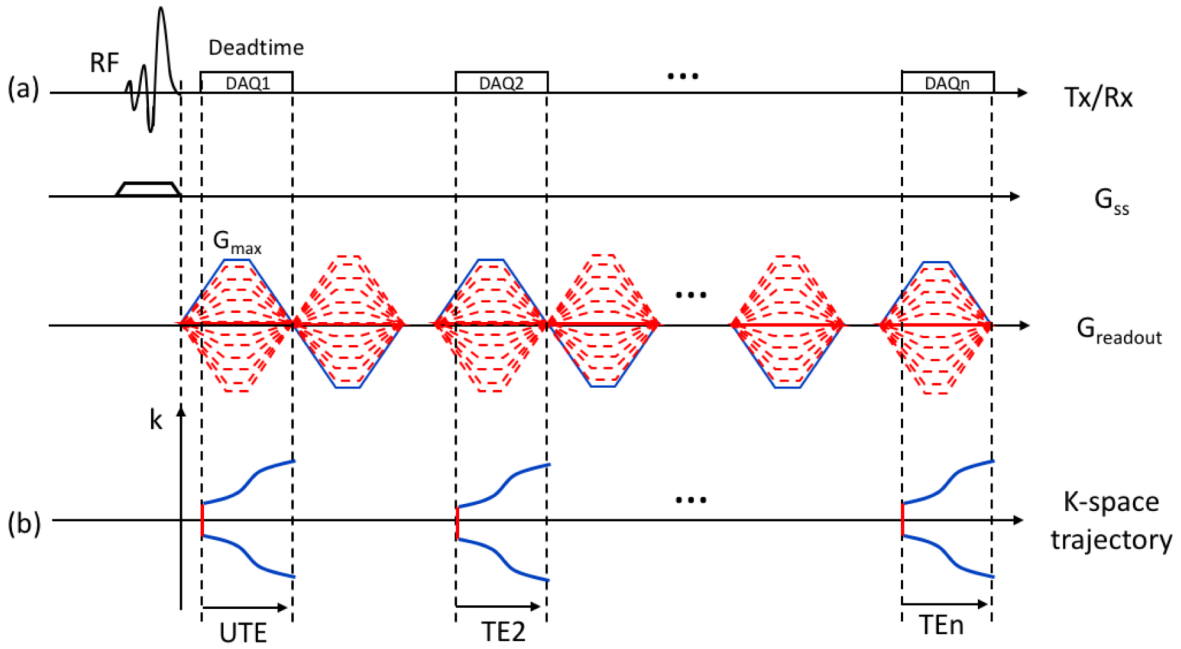

Figure 9. 1. Multi-echo ramped hybrid encoding (RHE). (a) Pulse sequence diagram, and (b) k-space trajectory. Note that images at later TEs are also hybrid encoded to benefit from the SPI encoding.

in non-Cartesian gradient echo imaging with a long echo train, where errors in k-space trajectory are accumulated over readout, causing severe imaging artifact if reconstructed with nominal k-space trajectory. To demonstrate feasibility, a knee of a healthy volunteer was imaged with the proposed RHE-based method with small or full coverage for knee, and bi-component fitting was performed in cartilage, tendon, and ligaments.

9.2 Methods

9.2.1 Multi-echo RHE

In the proposed imaging scheme, multi-echo RHE is utilized to acquire a UTE image followed by multiple gradient-echoes in a single scan as shown in Figure 9.1(a). In RHE, gradients are turned on before the RF coil deadtime and ramped up to maximum gradient, Gmax, to minimize readout duration and alleviate blurriness in short T2* tissues in a UTE image. After

UTE acquisition, a flying-back gradient echo train is applied to acquire 16 non-UTE images. A SLR half-pulse with zero iso-delay was used to enable slab selectivity.

k-Space is encoded with a center-out radial trajectory, acquiring multiple half-echoes. As in conventional hybrid encoding methods, the central region of k-space is acquired by Cartesian SPI (red lines in Figure 9.1(b)), and outer k-space is acquired by radial frequency encoding (blue lines in Figure 9.1(b)). Note that non-UTE images are also reconstructed based on the hybrid encoding scheme where central k-space region is covered by Cartesian SPI data although there is no missing radial frequency encoded data in the very k-space region, to benefit from the

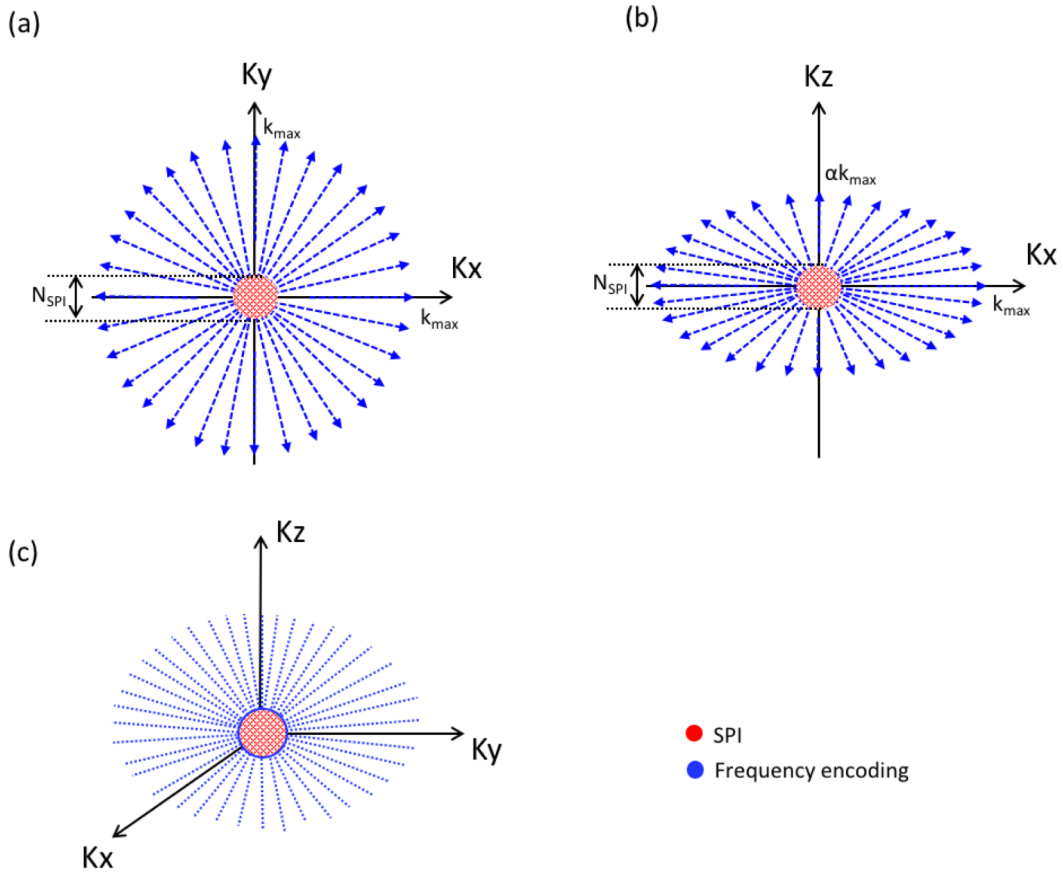

Figure 9. 2. Sampling trajectory. 2D k-space example of (a) x-y plane, and (b) x-z plane, and (c) 3D example. Note that k-space coverage in the z-axis was reduced to efficiently match the reduced spatial resolution in the slice direction.

robustness of SPI to magnetic susceptibility and error in estimation of k-space trajectory[166]. Saturation pulses was applied every TR before the RHE acquisition to suppress signal from fat.

9.2.2 *Sampling trajectory*

Figure 9.2(a) delineates a 2D example of the sampling trajectory in the logical x-y plane. Central k-space is encoded at a constant TE by SPI with a diameter, N_{SPI} (phase encoding steps in one axis), where one data point in the SPI region is encoded within each TR. Frequency encoding acquires outer k-space data up to k_{max} where the desired in-plane spatial resolution is achieved. Note that the size of the SPI region is somewhat exaggerated in illustrations in Figure 9.2. Figure 9.2(b) shows 2D example of sampling trajectory in logical x-z plane. The frequency encoding in logical z-direction is derated by a factor of α depending on the desired slice thickness (sptial rsolution in z-axis). In this study, to achieve 0.6x0.6x5mm resolution, Cartesian SPI was encoded using 15 phase encoding steps in one axis (N_{SPI}=15), where a 3D spherical region in central k-space is covered as shown in Figure 9.2(c). 9180 radial spokes were used for frequency encoding to cover k-space with an ellipsoidal shape with reduced coverage in the logical z-axis (physical L-R direction) with α=0.5 as shown in Figure 9.2(c).

9.2.3 k-Space trajectory measurement

The originally proposed dynamic SPI-based gradient measurement technique is prone to be biased by the effects of B0 inhomogeneity when the readout duration is long (~30ms in this study), which causes images wrong FOV in the later echoes. Therefore, the original SPI-based calibration method needs to be further modified. In the original method, 1D dynamic SPI is acquired for each physical gradient axis with optional pre-dephasing gradient to enhance the accuracy of trajectory estimation close to the center of k-space as shown in Figure 9.3(a). One

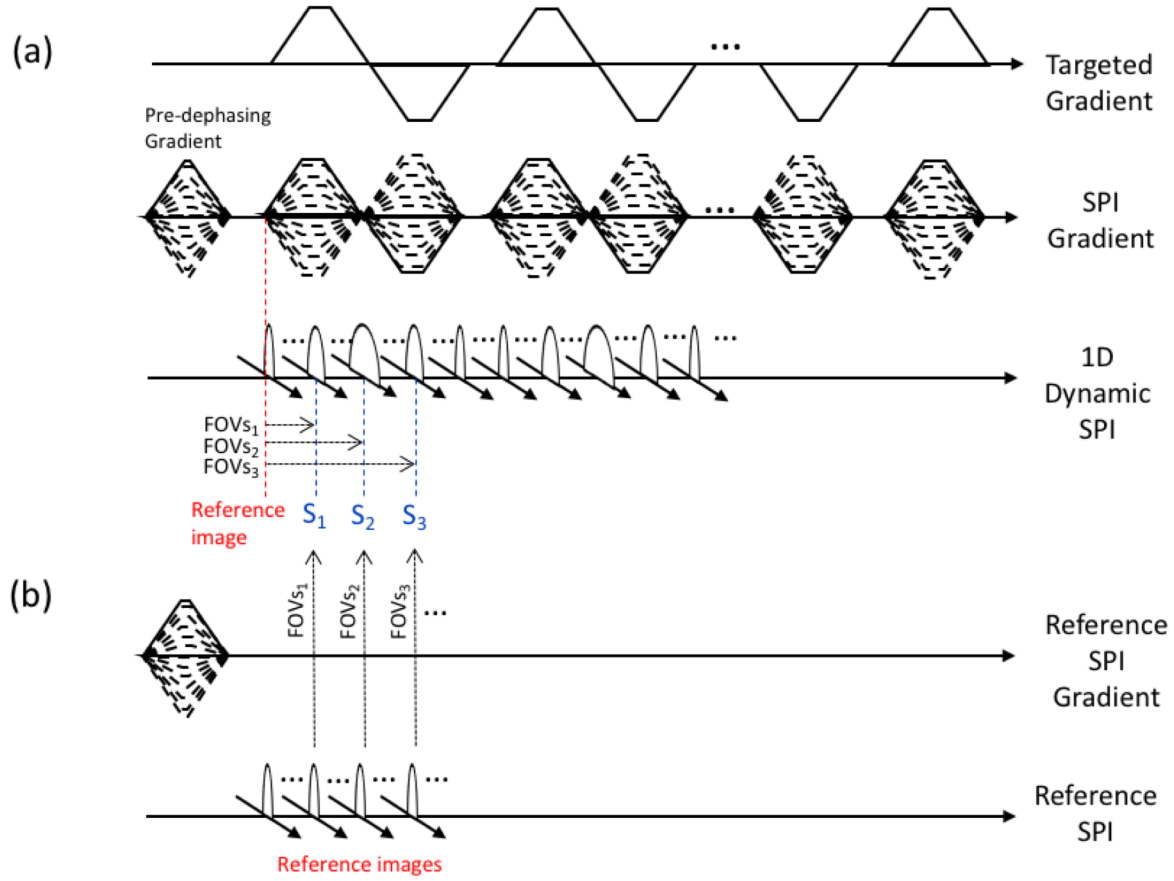

Figure 9. 3. Dynamic SPI based k-space trajectory measurement. (a) Original method, and (b) Improved method.

reference image (indicated by the red dotted line in Figure 9.3(a)) is selected and FOV scaling factors are estimated between the reference image and targeted SPI images (S_1, S_2, S_3, … indicated by blue dotted lines in Figure 9.3(a)). In the improved k-space trajectory measurement method, another SPI data is acquired with SPI gradients turned off except a pre-dephasing gradient, and FOV scaling factors are estimated between reference SPI images and the corresponding targeted SPI images as shown in Figure 9.3(b). The estimated FOV scaling factors (FOV_1, FOV_2, … in Figure 9.2) are converted to k-space trajectory. Note that the measurement of k-space trajectory needs to be performed only once for a imaging protocol on a given MRI scanner, and does not need to be repeated for in vivo imaging experiments[106].

9.2.4 Experimental Setup

Multi-echo RHE was performed on the left knee of one healthy volunteer using a 3T scanner (MR750, GE Healthcare, Waukesha, WI) and 8-channel T/R extremity coil under approval from our institutions IRB. Imaging parameters are as follows: Gmax=50mT/m, slewrate=200mT/m/ms, readout duration=600µs, spatial resolution=0.6x0.6x3mm^3, FOV=18x18x3cm^3 or 15x15x15cm^3, TR=33ms, TE=[0.08 2.0 3.9 5.8 7.7 9.6 11.5 13.4 15.3 17.1 19.0 20.9 22.8 24.7 26.6 28.5 30.4ms], and 7min35sec minute scan time. Note that two imaging experiments using RHE were performed on the same subject with different FOVs: 3cm at patella tendon and 15cm for fully covered imaging. Trajectory measurement was performed for 3 physical gradient axis using a body coil with the following imaging parameters: N_{SPI}=1201,

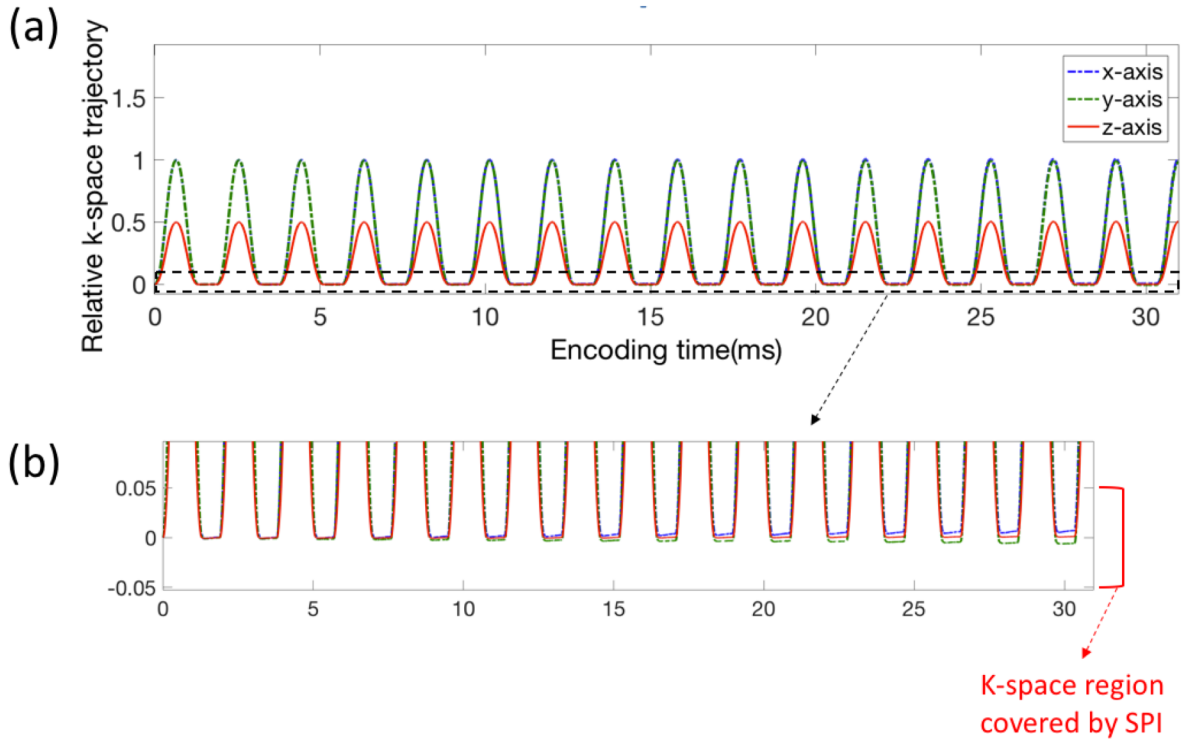

Figure 9. 4. Measured k-space trajectory. (a) Trajectory of UTE and 16-echoes, and (b) zoomed-in view close to center of k-space. Note that the later echoes deviate from center of k-space, which can be covered by SPI in the proposed hybrid encoding.

TR=40ms, and total scan time=4min48sec including reference scan.

For comparison, a 3D-Cones UTE acquisition with total 16 echoes including UTE was performed on the knee of the same subject[167], where 4 separated scans were performed with acquisition of 4 echoes in each scan. Images with spatial resolution=0.67x0.67x3mm^3 and 10 slices through the patellar tendon were acquired with total 13min scan time (cumulative time for the four separate scans).

9.2.5 Image reconstruction and data analysis

Images were reconstructed using convolution gridding with oversampling rate=1.5 and kernel width=3 pixel, using the k-space trajectory measured by dynamic SPI-based gradient measurement as explained above. Iterative convolution-based density compensation was performed and applied to gridding. For data fitting, mono-component and bi-component exponential signal models implementing a non-linear least square fitting method under the assumption of a Rician-distributed noise[160] were used to characterize the water components in musculoskeletal tissues.

9.3 Results

9.3.1 Trajectory Measurement

Figure 9.4(a) shows the measured k-space trajectory of total 17 echoes in 3 gradient axis. Note that this plot shows relative k-space trajectories where 1.0 corresponds to k_{max}, k-space position for desired in-plane resolution, which was 0.6mm resolution in the experiments. As shown in the zoomed-in views of Figure 9.4(b), k-space trajectories deviate from the center of k-space over TE, especially in the x and y-axis, where 2x stronger gradient (G_{max} and slewrate) are applied to achieve high resolution in plane, which implies an accumulation of errors in k-space

trajectory over subsequent echoes. Therefore, if images are reconstructed with only frequency encoded data, some data in the central region of k-space can be missed, resulting in imaging artifacts and errors in data fitting. In the reconstruction strategy of the proposed method where later echo images are also hybrid encoded, SPI encoding covers this missing data in the central region of k-space in later echoes. In our experiments, approximately 5% of central k-space region was covered by SPI, which is larger than the deviation of k-space trajectory in frequency encoding at the last echoes as shown in Figure 9.4(b).

9.3.2 In Vivo Experiment

Figure 9.5(a) shows sagittal images through the knee at 17 echoes acquired using RHE

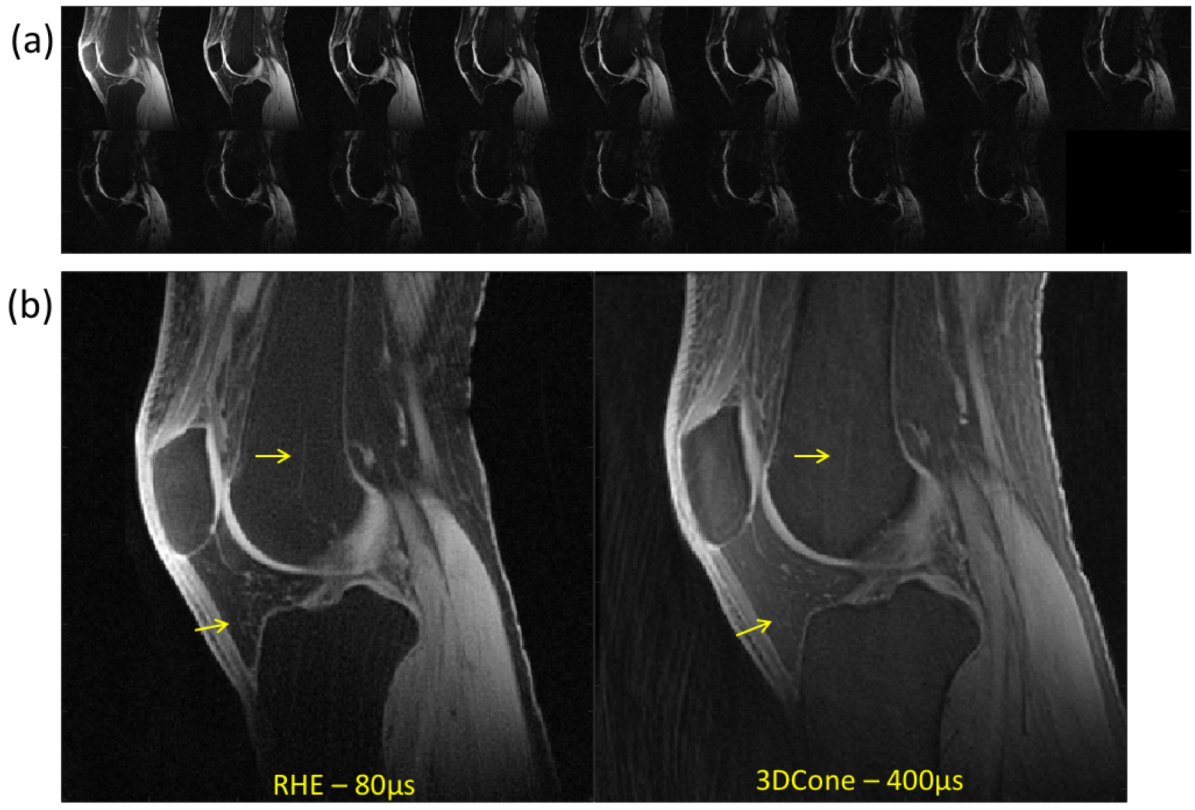

Figure 9. 5. Reconstructed images. (a) RHE images acquired at 17 TEs, and (b) RHE image vs. 3D-Cones. Note that RHE shows better resolution, less artifact, and sharper tissue boundaries owing to the shorter readout duration in RHE (600µs) compared to 3D-Cones (1.2ms).

with small FOV in z-axis (3cm). There was a monotonic decay of the signal for all tissues with much stronger decay occurring prior to 2ms for patellar tendon. Figure 9.5(b) compares the UTE echo image acquired by RHE and 3D-Cones, where RHE shows better resolution, less artifact, and sharper tissue boundaries as indicated by yellow arrows owing to the shorter readout duration in RHE (600μs) compared to 3D-Cones (1.2ms).

Figure 9.6 and 9.7 shows quantitative results obtained from RHE with large FOV in z-axis (15cm) that fully-covers knee. As shown in Figure 9.6, RHE provides similar parameter estimations of the patellar tendon with good fitting quality similar to 3D-Cones in short T2* fraction (f_s), short T2* ($T2^*_S$), and long T2*($T2^*_L$). Figure 9.7 shows bi-component T2* maps of ligament, meniscus, and tendon of the knee acquired using RHE which provide similar parameter estimations as previously published techniques[163,164].

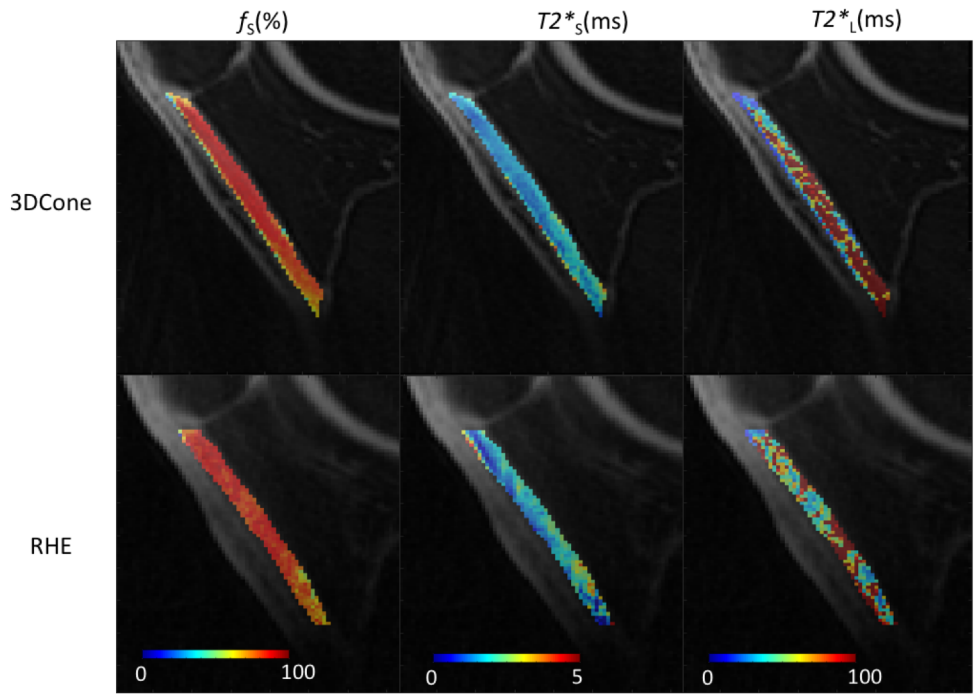

Figure 9. 6. Bi-component T2* map in patellar tendon. RHE provides similar parameter estimations of the patellar tendon with fitting quality similar to 3D-Cones.

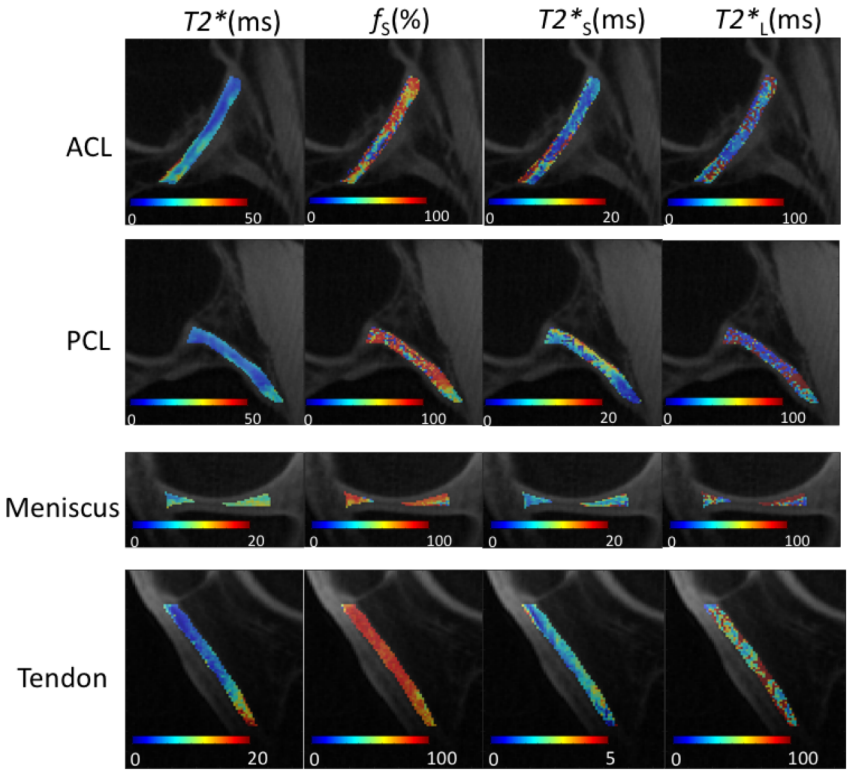

Figure 9. 7. ACL/PCL/Meniscus/Tendon. The estimated T2*s were similar as previously published techniques.

9.4 Discussion and Conclusion

This study has demonstrated the feasibility of a single acquisition multi-echo RHE imaging method to provide bi-component UTE T2* analysis of ligament, meniscus, and tendon within the human knee joint at 3T. The current 7min 35sec scan time of RHE could be further reduced by optimizing fat saturation, which takes 23% of the total imaging time. In contrast to other acquisition techniques, the later echoes in multi-echo RHE are more robust to B0 inhomogeneity, magnetic susceptibility artifact, and eddy current induced trajectory distortions due to the

benefits of SPI. Moreover, we have shown that the center of k-space that can be missed in conventional pure frequency encoding based methods in a long radial gradient echo train that is always sampled by SPI in the proposed hybrid encoding scheme.

With a single scan strategy, all echoes needed to perform bi-component signal fitting are acquired at a similar time making the method less sensitive to model fitting errors due to patient motion artifact. Furthermore, total scan time was less than 60% of the 3D Cones sequences without the use of parallel imaging or optimization of fat saturation pulses. The multi-echo RHE sequence can provide rapid bi-component T2* analysis of ligament, meniscus, and tendon. Further technical development is necessary to allow the acquisition of later echoes using the RHE method to perform bi-component T2* analysis of cartilage.

Chapter 10. Summary and Future Works

10.1 Summary

In this dissertation, novel uses of SPI were explored. In Chapter 4, k-space extrapolation method using dynamic SPI was described, which enables accurate T2* estimation and oxygen mapping in EPRI with a single data acquisition that allows at least 3X acceleration. In Chapter 5, an accelerated dynamic SPI based EPR-oximetry utilizing PCA-based compressed sensing was presented, where a new random sampling pattern and bilateral k-space extrapolation were also proposed. In Chapter 6, a novel method for gradient measurement based on 1D dynamic SPI were described, which were applied in studies presented in Chapter 7, 8, and 9, showing its efficacy in non-Cartesian imaging. In Chapter 7, an improved hybrid encoding scheme, ramped hybrid encoding (RHE), was proposed, which alleviates slice-selectivity artifact and minimizes per-excitation encoding time to reduce short T2* blurriness effect. In Chapter 8 and 9, two applications of RHE were described. In Chapter 8, a new MRAC method based on dual echo RHE was proposed, where a UTE image and an out-of-phase image are acquired in a single scan to enable 4-species segmentation (water, fat, bone, and air). In Chapter 9, an application of multi-echo RHE on human knee imaging was presented, where an improved SPI-based gradient measurement technique adapted to a long gradient echo train was also proposed.

Throughout the chapters enumerated above, the efficacy of SPI was explored in EPRI and MRI. In the current EPR system where a constant encoding gradient is used due to extremely short T2* decay of spin probe (<600μs) and slow gradient system, SPI is one of few choices available for encoding. Due to long RF coil deadtime, SPI is only one method that can directly measure FID without refocusing RF pulse, which is also beneficial in terms of SNR. Moreover,

SPI-based method is more robust to T2* blurriness effect over radial frequency encoding-based method[168] where signal rapidly decays in long readout causing loss of high spatial frequency in image (or k-space). With development of k-space extrapolation, we showed a feasibility of dynamic SPI encoding in EPR-oxymetry, which is highly time efficient, where a myriad of images is acquired in a single scan. In the studies in MRI, it was shown that SPI played important role in qualitative and quantitative imaging in hybrid encoding.

10.2 Future works

In this dissertation, dynamic SPI was explored in EPRI, and SPI for hybrid encoding was mostly explored in MRI, which implies there still exist undiscovered topics for SPI in EPRI and MRI: dynamic SPI in MRI and hybrid encoding in EPRI.

In Chapter 8, a feasibility of dynamic SPI in hybrid encoding was briefly shown, where oversampled SPI encoding was utilized to secure multiple UTE images for more accurate air segmentation. In future works, the dynamic SPI in hybrid encoding for improved quantitative imaging will be explored in MRI. k-Space extrapolation for quantitative imaging will be also explored in MRI.

I have recently performed a feasibility study on hybrid encoding in EPRI, which showed that hybrid encoding is also effective in EPRI to enhance spatial-temporal resolution. The key idea was same as oversampling SPI. In vivo experiment will be performed with this topic after optimizing imaging parameters and reconstruction methods.

Dynamic SPI-based gradient measurement technique will be further explored. First, the very technique will be also tested in EPR imaging to enable use of non-constant gradients (e.g., sine wave). Second, measurement of higher order gradient terms will be explored using 2D or

3D SPI to resolve spatial variation of gradient deviated from a linear gradient model. Third, an advanced method for GIRF measurement will be explored, using a frequency-sweeping gradient (chirp pulse) instead of gradient blips used in the previous study, which will allow higher spectral resolution in the estimated GIRF.

Appendix 1. List of Conference Abstracts and Publications

Peer-reviewed conference abstracts

(*: ISMRM Merit Award Magna Cum Laude, **: ISMRM Merit Award Summa Cum Laude)

__Hyungseok Jang__, Curtis N. Wiens, and Alan B. McMillan. (2016). Simultaneous measurement of short and long T2 components using hybrid encoding, In Proceedings of the ISMRM 24th Annual Meeting, Singapore.

Hyungseok Jang, and Alan B. McMillan. (2016). Single point based techniques for rapid and robust gradient measurement, In Proceedings of the ISMRM 24th Annual Meeting. Singapore.

Hyungseok Jang, Hyung Jun Im, Arman Rahmim, Steve Y. Cho, and Alan McMillan. (2016). On the Feasibility of Quantitative Dynamic Whole Body PET/MR Imaging, In Proceedings of the ISMRM 24th Annual Meeting, Singapore.

Hyungseok Jang, and Alan B. McMillan. (2016). Rapid Multi-echo Ultrashort Time Echo Imaging for MR-based Attenuation Correction in PET/MR, In Proceedings of the ISMRM 24th Annual Meeting, Singapore.

****Hyungseok Jang**, Curtis N. Wiens, and Alan B McMillan. (2015). Ramped Hybrid Encoding for Improved Ultrashort TE Imaging, In Proceedings of the ISMRM 23rd Annual Meeting, Toronto, Canada.

****Hyungseok Jang**, Chandramouli Gadisetti, Devasahayam Nallathamby, Murali C Krishna, and Alan B. McMillan. (2015). Hybrid Encoding for Quantitative Electron Paramagnetic Resonance Imaging, In Proceedings of the ISMRM 23rd Annual Meeting, Toronto, Canada.

****Curtis N. Wiens, Nathan S. Artz, **Hyungseok Jang**, Alan B. McMillan, and Scott B. Reeder. (2015). Externally Calibrated Parallel Imaging in the Presence of Metallic Implants, In Proceedings of the ISMRM 23rd Annual Meeting. Toronto, Canada.

James L. Patrick, Perry J. Pickhardt, **Hyungseok Jang**, Scott B. Perlman, Alan B. McMillan. (2015). Lesion Detection and Workflow Optimization in Whole Body Diffusion MR Imaging Using Trimodality PET/CT+MR in the Oncology Setting, In Proceedings of the ISMRM 23rd Annual Meeting. Toronto, Canada.

__Hyungseok Jang__, Sankaran Subramanian, Nallathamby Devasahayam, Shingo Matsumoto, Keita Saito, Murali C. Krishna, and Alan B. McMillan. (2014). Measurement of T2 and T2 in Spin Echo Single Point EPR Imaging Using a Single Acquisition Method, In Proceedings of the ISMRM 22nd Annual Meeting. Milan, Italy.

*__Hyungseok Jang__, Sankaran Subramanian, Nallathamby Devasahayam, Shingo Matsumoto, Keita Saito, Jiachen Zhuo, Murali C. Krishna, and Alan B. McMillan. (2014). Accelerated Quantitative Single Point EPR Imaging Using Model-based Compressed Sensing, In Proceedings of the ISMRM 22nd Annual Meeting. Milan, Italy.

Hyungseok Jang, Sankaran Subramanian, Nallathamby Devashayam, Murali C. Krishna, and Alan B. McMillan. (2013). A method to improve temporal resolution in EPR imaging of tissue oxygenation Purpose, In Proceedings of the ISMRM 21st Annual Meeting. Utah, USA.

Alan B. McMillan, **Hyungseok Jang**, Sankaran Subramanian, and Murali C. Krishna. (2013). Optimal Partial Fourier Reconstructions in Electron Paramagnetic Resonance Imaging, In Proceedings of the ISMRM 21st Annual Meeting. Utah, USA.

Publications

Hyungseok Jang, and Alan B. McMillan. A rapid and robust gradient measurement technique using dynamic single-point imaging. Magnetic Resonance in Medicine. 2016;0(2016).

Curtis N. Wiens, Nathan S. Artz, **Hyungseok Jang**, Alan B. McMillan, and Scott B. Reeder. Externally calibrated parallel imaging for 3D multispectral imaging near metallic implants using broadband ultrashort echo time imaging. Magnetic Resonance in Medicine. 2016;0(February):1–7.

Hyungseok Jang, Curtis N. Wiens, and Alan B. McMillan. Ramped hybrid encoding for improved ultrashort echo time imaging. Magnetic Resonance in Medicine. 2016;76(3):814–825.

Hyungseok Jang, Shingo Matsumoto, Nallathamby Devasahayam, Sankaran Subramanian, Jiachen Zhuo, Murali C. Krishna, and Alan B. McMillan. Accelerated 4D quantitative single point EPR imaging using model-based reconstruction. Magnetic Resonance in Medicine. 2015;73(4):1692–1701.

Hyungseok Jang, Sankaran Subramanian, Nallathamby Devasahayam, Keita Saito, Shingo Matsumoto, Murali C. Krishna, and Alan B. McMillan. Single Acquisition Quantitative Single-Point Electron Paramagnetic Resonance Imaging. Magnetic Resonance in Medicine. 2013;70(4):1173–1181.

Bibliography

1. Subramanian S, Krishna MC. Dancing With the Electrons: Time-Domain and Cw in Vivo Epr Imaging. Magnetic resonance insights. 2008;2(301):43–74.

2. Subramanian S, Devasahayam N, McMillan A, Matsumoto S, Munasinghe JP, Saito K, Mitchell JB, Chandramouli GVR, Krishna MC. Reporting of quantitative oxygen mapping in EPR imaging. Journal of magnetic resonance (San Diego, Calif. : 1997). 2012;214(1):244–51.

3. Tyler DJ, Robson MD, Henkelman RM, Young IR, Bydder GM. Magnetic resonance imaging with ultrashort TE (UTE) PULSE sequences: technical considerations. Journal of magnetic resonance imaging : JMRI. 2007;25(2):279–89.

4. Madio DP, Lowe IJ. Ultra-fast imaging using low flip angles and fids. Magnetic Resonance in Medicine. 1995;34(4):525–529.

5. Emid S, Creyghton JHN. High resolution NMR imaging in solids. Physica B+C. 1985;128(1):81–83.

6. Subramanian S, Devasahayam N, Murugesan R, Yamada K, Cook J, Taube A, Mitchell JB, Lohman J a B, Krishna MC. Single-point (constant-time) imaging in radiofrequency Fourier transform electron paramagnetic resonance. Magnetic resonance in medicine : official journal of the Society of Magnetic Resonance in Medicine / Society of Magnetic Resonance in Medicine. 2002;48(2):370–9.

7. Matsumoto K, Subramanian S, Devasahayam N, Aravalluvan T, Murugesan R, Cook J a, Mitchell JB, Krishna MC. Electron paramagnetic resonance imaging of tumor hypoxia: enhanced spatial and temporal resolution for in vivo pO2 determination. Magnetic resonance in medicine : official journal of the Society of Magnetic Resonance in Medicine / Society of Magnetic Resonance in Medicine. 2006;55(5):1157–63.

8. Grodzki DM, Jakob PM, Heismann B. Ultrashort echo time imaging using pointwise encoding time reduction with radial acquisition (PETRA). Magnetic resonance in medicine : official journal of the Society of Magnetic Resonance in Medicine / Society of Magnetic Resonance in Medicine. 2012;67(2):510–8.

9. Halse M, Rioux J, Romanzetti S, Kaffanke J, MacMillan B, Mastikhin I, Shah NJ, Aubanel E, Balcom BJ. Centric scan SPRITE magnetic resonance imaging: optimization of SNR, resolution, and relaxation time mapping. Journal of magnetic resonance (San Diego, Calif. : 1997). 2004;169(1):102–17.

10. Jang H, Subramanian S, Devasahayam N, Saito K, Matsumoto S, Krishna MC, McMillan AB. Single Acquisition Quantitative Single-Point Electron Paramagnetic Resonance Imaging. Magnetic Resonance in Medicine. 2013;70(4):1173–1181.

11. Huang C, Graff CG, Clarkson EW, Bilgin A, Altbach MI. T2 mapping From highly undersampled data by reconstruction of principal component coefficient maps using compressed sensing. Magnetic Resonance in Medicine. 2011;0:n/a-n/a.

12. Jang H, Matsumoto S, Devasahayam N, Subramanian S, Zhuo J, Krishna MC, McMillan AB. Accelerated 4D quantitative single point EPR imaging using model-based reconstruction. Magnetic Resonance in Medicine. 2015;73(4):1692–1701.

13. Jang H, Wiens CN, McMillan AB. Ramped hybrid encoding for improved ultrashort echo time imaging. Magnetic Resonance in Medicine. 2016;76(3):814–825.

14. Ohliger M a., Sodickson DK. An introduction to coil array design for parallel MRI. NMR in Biomedicine. 2006;19(3):300–315.

15. Roemer PB, Edelstein WA, Hayes CE. The NMR phased array. 1989;16(2):192–225.

16. Zhu Y, Hardy CJ, Sodickson DK, Giaquinto RO, Dumoulin CL, Kenwood G, Niendorf T, Lejay H, McKenzie C a., Ohliger M a., et al. Highly parallel volumetric imaging with a 32-element RF coil array. Magnetic Resonance in Medicine. 2004;52(4):869–877.

17. Fujita H. New horizons in MR technology: RF coil designs and trends. Magnetic resonance in medical sciences : MRMS : an official journal of Japan Society of Magnetic Resonance in Medicine. 2007;6(1):29–42.

18. Hoult DI. The NMR receiver: A description and analysis of design. Progress in Nuclear Magnetic Resonance Spectroscopy. 1978;12(1):41–77.

19. Ono M, Ito K, Kawamura N, Hsieh KC, Hirata H, Tsuchihashi N, Kamada H. A surface-coil-type resonator for in vivo ESR measurements. Journal of magnetic resonance. Series B. 1994;104(2):180–182.

20. Hirata H, Ono M. A flexible surface-coil-type resonator using triaxial cable. Review of Scientific Instruments. 1997;68(9):3595.

21. Suits BH, Wilken DE. Improving magnetic field gradient coils for NMR imaging. Journal of Physics E: Scientific Instruments. 2000;22(8):565–573.

22. Rinard G, Quine R, Eaton G. Magnet and gradient coil system for low field EPR imaging. Concepts in Magnetic Resonance. 2002.

23. Song J, Liu QH. An efficient MR image reconstruction method for arbitrary K-space trajectories without density compensation. Conference proceedings : ... Annual International Conference of the IEEE Engineering in Medicine and Biology Society. IEEE Engineering in Medicine and Biology Society. Conference. 2006;1(1):3767–70.

24. Rasche V, Proksa R, Sinkus R, Börnert P, Eggers H. Resampling of data between arbitrary grids using convolution interpolation. IEEE transactions on medical imaging. 1999;18(5):385–92.

25. Jang H, McMillan AB. A rapid and robust gradient measurement technique using dynamic single-point imaging. Magnetic Resonance in Medicine. 2016;0(2016).

26. Subramanian S, Matsumoto K-I, Mitchell JB, Krishna MC. Radio frequency continuous-wave and time-domain EPR imaging and Overhauser-enhanced magnetic resonance imaging of

small animals: instrumental developments and comparison of relative merits for functional imaging. NMR in biomedicine. 2004;17(5):263–94.

27. Balcom BJ, Macgregor RP, Beyea SD, Green DP, Armstrong RL, Bremner TW. Single-Point Ramped Imaging with T1 Enhancement (SPRITE). Journal of Magnetic Resonance, Series A. 1996;123(1):131–134.

28. Xiao D, Balcom BJ. Hybrid-SPRITE MRI. Journal of magnetic resonance (San Diego, Calif. : 1997). 2013;235:6–14.

29. Han H, MacGregor RP, Balcom BJ. Pure phase encode magnetic field gradient monitor. Journal of Magnetic Resonance. 2009;201(2):212–217.

30. Halse M, Goodyear DJ, MacMillan B, Szomolanyi P, Matheson D, Balcom BJ. Centric scan SPRITE magnetic resonance imaging. Journal of magnetic resonance (San Diego, Calif. : 1997). 2003;165(2):219–29.

31. Kaffanke JB, Romanzetti S, Dierkes T, Leach MO, Balcom BJ, Jon Shah N. Multi-Frame SPRITE: A method for resolution enhancement of multiple-point SPRITE data. Journal of magnetic resonance (San Diego, Calif. : 1997). 2013;230C:111–116.

32. Beyea SD, Balcom BJ, Prado PJ, Cross a R, Kennedy CB, Armstrong RL, Bremner TW. Relaxation time mapping of short T*2 nuclei with single-point imaging (SPI) methods. Journal of magnetic resonance (San Diego, Calif. : 1997). 1998;135(1):156–164.

33. Marica F, Goora FG, Balcom BJ. FID-SPI Pulse Sequence for Quantitative MRI of Fluids in Porous Media. Journal of Magnetic Resonance. 2014;(December 2013).

34. Grodzki DM, Jakob PM, Heismann B. Correcting slice selectivity in hard pulse sequences. Journal of magnetic resonance (San Diego, Calif. : 1997). 2012;214(1):61–7.

35. Balcom BJ, Bogdan M, Armstrong RL. Single-Point Imaging of Gradient Rise, Stabilization, and Decay. Journal of Magnetic Resonance, Series A. 1996;118(1):122–125.

36. Goodyear DJ, Shea M, Beyea SD, Shah NJ, Balcom BJ. Single point measurements of magnetic field gradient waveform. Journal of Magnetic Resonance. 2003;163(1):1–7.

37. Halpern HJ, Yu C, Peric M, Barth E, Grdina DJ, Teicher B a. Oxymetry deep in tissues with low-frequency electron paramagnetic resonance. Proceedings of the National Academy of Sciences of the United States of America. 1994;91(26):13047–51.

38. Krishna MC, Devasahayam N, Cook J a, Subramanian S, Kuppusamy P, Mitchell JB. Electron paramagnetic resonance for small animal imaging applications. ILAR journal / National Research Council, Institute of Laboratory Animal Resources. 2001;42(3):209–18.

39. Vaupel P HL. Tumor hypoxia: causative factors, compensatory mechanisms, and cellular response. Oncologist. 2004;9(5):4–9. 2004;9(suppl 5):4–9.

40. Brown JM. Evidence for acutely hypoxic cells in mouse tumours, and a possible mechanism of reoxygenation. The British journal of radiology. 1979;52(620):650–6.

41. Ahmad R KP. Theory, instrumentation, and applications of electron paramagnetic resonance oximetry. 2011;110(5):3212–3236.

42. Kaffanke J, Dierkes T, Romanzetti S, Halse M, Rioux J, Leach MO, Balcom B, Shah NJ. Application of the chirp z-transform to MRI data. Journal of magnetic resonance (San Diego, Calif. : 1997). 2006;178(1):121–8.

43. Bao Y, Maudsley A a. Improved reconstruction for MR spectroscopic imaging. IEEE transactions on medical imaging. 2007;26(5):686–95.

44. Haupt CI, Schuff N, Weiner MW, Maudsley a a. Removal of lipid artifacts in 1H spectroscopic imaging by data extrapolation. Magnetic resonance in medicine : official journal of the Society of Magnetic Resonance in Medicine / Society of Magnetic Resonance in Medicine. 1996;35(5):678–87.

45. Beatty PJ, Nishimura DG, Pauly JM. Rapid gridding reconstruction with a minimal oversampling ratio. IEEE transactions on medical imaging. 2005;24(6):799–808.

46. Pipe JG. Reconstructing MR images from undersampled data: data-weighting considerations. Magnetic resonance in medicine : official journal of the Society of Magnetic Resonance in Medicine / Society of Magnetic Resonance in Medicine. 2000;43(6):867–75.

47. Amartur S, Haacke EM. Modified iterative model based on data extrapolation method to reduce Gibbs ringing. Journal of magnetic resonance imaging : JMRI. 1991;1(3):307–17.

48. Amartur S, Liang ZP, Boada F, Haacke EM. Phase-constrained data extrapolation method for reduction of truncation artifacts. Journal of magnetic resonance imaging : JMRI. 1(6):721–4.

49. Block KT, Uecker M, Frahm J. Suppression of MRI truncation artifacts using total variation constrained data extrapolation. International journal of biomedical imaging. 2008;2008:184123.

50. Constable RT, Henkelman RM. Data extrapolation for truncation artifact removal. Magnetic resonance in medicine : official journal of the Society of Magnetic Resonance in Medicine / Society of Magnetic Resonance in Medicine. 1991;17(1):108–18.

51. Luo J, Wang S, Li W, Zhu Y. Removal of truncation artefacts in magnetic resonance images by recovering missing spectral data. Journal of magnetic resonance (San Diego, Calif. : 1997). 2012;224:82–93.

52. Archibald R, Gelb A. A method to reduce the Gibbs ringing artifact in MRI scans while keeping tissue boundary integrity. IEEE transactions on medical imaging. 2002;21(4):305–19.

53. Devasahayam N, Subramanian S, Murugesan R, Hyodo F, Matsumoto K-I, Mitchell JB, Krishna MC. Strategies for improved temporal and spectral resolution in in vivo oximetric imaging using time-domain EPR. Magnetic resonance in medicine : official journal of the Society of Magnetic Resonance in Medicine / Society of Magnetic Resonance in Medicine. 2007;57(4):776–83.

54. Jones R a, Haraldseth O, Müller TB, Rinck P a, Oksendal a N. K-space substitution: a novel dynamic imaging technique. Magnetic resonance in medicine : official journal of the Society of

Magnetic Resonance in Medicine / Society of Magnetic Resonance in Medicine. 1993;29(6):830–4.

55. Van Vaals JJ, Brummer ME, Thomas Dixon W, Tuithof HH, Engels H, Nelson RC, Gerety BM, Chezmar JL, Den Boer JA. "Keyhole" method for accelerating imaging of contrast agent uptake. Journal of Magnetic Resonance Imaging. 1993;3(4):671–675.

56. Korosec FR, Frayne R, Grist TM, Mistretta CA. Time-resolved contrast-enhanced 3D MR angiography. Magnetic Resonance in Medicine. 1996;36(3):345–351.

57. Matsumoto S, Hyodo F, Subramanian S, Devasahayam N, Munasinghe J, Hyodo E, Gadisetti C, Cook JA, Mitchell JB, Krishna MC. Low-field paramagnetic resonance imaging of tumor oxygenation and glycolytic activity in mice. The Journal of clinical investigation. 2008;118(5):1965–73.

58. Yasui H, Matsumoto S, Devasahayam N, Munasinghe JP, Choudhuri R, Saito K, Subramanian S, Mitchell JB, Krishna MC. Low-field magnetic resonance imaging to visualize chronic and cycling hypoxia in tumor-bearing mice. Cancer research. 2010;70(16):6427–36.

59. Chaplin DJ, Olive PL, Durand RE. Intermittent blood flow in a murine tumor: radiobiological effects. Cancer research. 1987;47(2):597–601.

60. Kimura H, Braun RD, Ong ET, Hsu R, Secomb TW, Papahadjopoulos D, Hong K, Dewhirst MW. Fluctuations in red cell flux in tumor microvessels can lead to transient hypoxia and reoxygenation in tumor parenchyma. Cancer research. 1996;56(23):5522–8.

61. Cárdenas-Navia LI, Mace D, Richardson R a, Wilson DF, Shan S, Dewhirst MW. The pervasive presence of fluctuating oxygenation in tumors. Cancer research. 2008;68(14):5812–9.

62. Dewhirst MW, Cao Y, Moeller B. Cycling hypoxia and free radicals regulate angiogenesis and radiotherapy response. Nature reviews. Cancer. 2008;8(6):425–37.

63. Dewhirst MW. Relationships between cycling hypoxia, HIF-1, angiogenesis and oxidative stress. Radiation research. 2009;172(6):653–65.

64. Hoek TL V., Becker LB, Shao Z-H, Li C-Q, Schumacker PT. Preconditioning in Cardiomyocytes Protects by Attenuating Oxidant Stress at Reperfusion. Circulation Research. 2000;86(5):541–548.

65. Vaupel P, Schlenger K, Knoop C, Höckel M. Oxygenation of human tumors: evaluation of tissue oxygen distribution in breast cancers by computerized O2 tension measurements. Cancer research. 1991:3316–3322.

66. Rosenman J. Incorporating Functional Imaging Information Into Radiation Treatment. Seminars in radiation oncology. 2001;11(1):83–92.

67. Hutchinson M, Raff U. Fast MRI data acquisition using multiple detectors. Magnetic resonance in medicine : official journal of the Society of Magnetic Resonance in Medicine / Society of Magnetic Resonance in Medicine. 1988;6(1):87–91.

68. Sodickson DK, Manning WJ. Simultaneous acquisition of spatial harmonics (SMASH): fast imaging with radiofrequency coil arrays. Magnetic resonance in medicine : official journal of the Society of Magnetic Resonance in Medicine / Society of Magnetic Resonance in Medicine. 1997;38(4):591–603.

69. Pruessmann KP, Weiger M, Scheidegger MB, Boesiger P. SENSE: sensitivity encoding for fast MRI. Magnetic resonance in medicine : official journal of the Society of Magnetic Resonance in Medicine / Society of Magnetic Resonance in Medicine. 1999;42(5):952–62.

70. McGibney G, Smith MR, Nichols ST, Crawley A. Quantitative evaluation of several partial Fourier reconstruction algorithms used in MRI. Magnetic resonance in medicine : official journal of the Society of Magnetic Resonance in Medicine / Society of Magnetic Resonance in Medicine. 1993;30(1):51–9.

71. Subramanian S, Chandramouli GVR, McMillan A, Gullapalli RP, Devasahayam N, Mitchell JB, Matsumoto S, Krishna MC. Evaluation of partial k-space strategies to speed up time-domain EPR imaging. Magnetic resonance in medicine : official journal of the Society of Magnetic Resonance in Medicine / Society of Magnetic Resonance in Medicine. 2013;70(3):745–753.

72. Lustig M, Donoho D. Compressed Sensing MRI. Signal Processing Magazine. 2008;(March 2008):72–82.

73. Donoho DL. Compressed sensing. IEEE Transactions on Information Theory. 2006;52(4):1289–1306.

74. Candes EJ, Tao T. Near-Optimal Signal Recovery From Random Projections: Universal Encoding Strategies? IEEE Transactions on Information Theory. 2006;52(12):5406–5425.

75. Lustig M, Donoho D, Pauly JM. Sparse MRI: The application of compressed sensing for rapid MR imaging. Magnetic resonance in medicine : official journal of the Society of Magnetic Resonance in Medicine / Society of Magnetic Resonance in Medicine. 2007;58(6):1182–95.

76. Gamper U, Boesiger P, Kozerke S. Compressed sensing in dynamic MRI. Magnetic resonance in medicine : official journal of the Society of Magnetic Resonance in Medicine / Society of Magnetic Resonance in Medicine. 2008;59(2):365–73.

77. Jung H, Sung K, Nayak KS, Kim EY, Ye JC. k-t FOCUSS: a general compressed sensing framework for high resolution dynamic MRI. Magnetic resonance in medicine : official journal of the Society of Magnetic Resonance in Medicine / Society of Magnetic Resonance in Medicine. 2009;61(1):103–16.

78. Huang C, Graff CG, Clarkson EW, Bilgin A, Altbach MI. T2 mapping from highly undersampled data by reconstruction of principal component coefficient maps using compressed sensing. Magnetic resonance in medicine : official journal of the Society of Magnetic Resonance in Medicine / Society of Magnetic Resonance in Medicine. 2012;67(5):1355–66.

79. Velikina J V, Alexander AL, Samsonov A. Accelerating MR parameter mapping using sparsity-promoting regularization in parametric dimension. Magnetic resonance in medicine : official journal of the Society of Magnetic Resonance in Medicine / Society of Magnetic

Resonance in Medicine. 2012;0:1–11.

80. Aharon M, Elad M, Bruckstein A. K-SVD: An Algorithm for Designing Overcomplete Dictionaries for Sparse Representation. IEEE Transactions on Signal Processing. 2006;54(11):4311–4322.

81. Doneva M, Börnert P, Eggers H, Stehning C, Sénégas J, Mertins A. Compressed sensing reconstruction for magnetic resonance parameter mapping. Magnetic resonance in medicine : official journal of the Society of Magnetic Resonance in Medicine / Society of Magnetic Resonance in Medicine. 2010;64(4):1114–20.

82. Gonzalez R, Woods R. Sharpening Spatial Filters. In: Digital Image Processing. 2nd ed. Upper Saddle River, New Jersey: Prentice-Hall, Inc.; 2002. p. 75–146.

83. Pipe JG, Menon P. Sampling density compensation in MRI: rationale and an iterative numerical solution. Magnetic resonance in medicine : official journal of the Society of Magnetic Resonance in Medicine / Society of Magnetic Resonance in Medicine. 1999;41(1):179–86.

84. Rudin L, Osher S, Fatemi E. Nonlinear total variation based noise removal algorithms. Physica D: Nonlinear Phenomena. 1992;60:259–268.

85. Enomoto A, Hirata H, Matsumoto S, Saito K, Subramanian S, Krishna MC, Devasahayam N. Four-channel surface coil array for 300-MHz pulsed EPR imaging: Proof-of-concept experiments. Magnetic Resonance in Medicine. 2014;71(2):853–858.

86. Tan H, Meyer CH. Estimation of k-space trajectories in spiral MRI. Magnetic Resonance in Medicine. 2009;61(6):1396–1404.

87. Boesch CH. in Superconducting Magnets : Optimization of Corrections and Quantitative Characterization of Magnet / Gradient Systems. 1991;284:268–284.

88. Jehenson P, Westphal M, Schuff N. Analytical method for the compensation of eddy-current effects induced by pulsed magnetic field gradients in NMR systems. Journal of Magnetic Resonance (1969). 1990;90(2):264–278.

89. Ahn CB, Cho ZH. Analysis of the eddy-current induced artifacts and the temporal compensation in nuclear magnetic resonance imaging. IEEE transactions on medical imaging. 1991;10(1):47–52.

90. Wysong RE, Madio DP, Lowe IJ. A novel eddy current compensation scheme for pulsed gradient systems. Magnetic resonance in medicine : official journal of the Society of Magnetic Resonance in Medicine / Society of Magnetic Resonance in Medicine. 1994;31(5):572–575.

91. Wu Y, Chronik B a, Bowen C, Mechefske CK, Rutt BK. Gradient-induced acoustic and magnetic field fluctuations in a 4T whole- body MR imager. Magn Reson Med. 2000;44(4):532–6.

92. Foerster BU, Tomasi D, Caparelli EC. Magnetic field shift due to mechanical vibration in functional magnetic resonance imaging. Magnetic Resonance in Medicine. 2005;54(5):1261–1267.

93. Du YP, Zhou XJ, Bernstein M a. Correction of concomitant magnetic field-induced image artifacts in nonaxial echo-planar imaging. Magnetic Resonance in Medicine. 2002;48(3):509–515.

94. Zhou XJ, Du YP, Bernstein M a., Reynolds HG, Maier JK, Polzin J a. Concomitant magnetic-field-induced artifacts in axial echo planar imaging. Magnetic Resonance in Medicine. 1998;39(4):596–605.

95. Hammer BE. Magnetic field mapping with an array of nuclear magnetic resonance probes. Review of Scientific Instruments. 1996;67(6):2378.

96. De Zanche N, Barmet C, Nordmeyer-Massner J a., Pruessmann KP. NMR Probes for measuring magnetic fields and field dynamics in MR systems. Magnetic Resonance in Medicine. 2008;60(1):176–186.

97. Barmet C, De Zanche N, Pruessmann KP. Spatiotemporal magnetic field monitoring for MR. Magnetic Resonance in Medicine. 2008;60(1):187–197.

98. Barmet C, Wilm B, Pavan M, Pruessmann K. A third-order field camera with microsecond resolution for MR system diagnostics. Proc Intl Soc Mag Reson Med. 2009;4185(1988):780.

99. Duyn JH, Yang Y, Frank J a, van der Veen JW. Simple correction method for k-space trajectory deviations in MRI. Journal of magnetic resonance (San Diego, Calif. : 1997). 1998;132(1):150–153.

100. Papadakis NG, Martin KM, Pickard JD, Hall LD, Carpenter T a, Huang CL. Gradient preemphasis calibration in diffusion-weighted echo-planar imaging. Magnetic resonance in medicine : official journal of the Society of Magnetic Resonance in Medicine / Society of Magnetic Resonance in Medicine. 2000;44(4):616–624.

101. Johnson KM, Fain SB, Schiebler ML, Nagle S. Optimized 3D ultrashort echo time pulmonary MRI. Magnetic Resonance in Medicine. 2013;70(5):1241–1250.

102. Schneider JT, Haas M, Ruhm W, Hennig J, Ullmann P. Robust spatially selective excitation using radiofrequency pulses adapted to the effective spatially encoding magnetic fields. Magnetic Resonance in Medicine. 2011;65(2):409–421.

103. Gach HM, Lowe IJ, Madio DP, Caprihan a, Altobelli S a, Kuethe DO, Fukushima E. A programmable pre-emphasis system. Magnetic resonance in medicine : official journal of the Society of Magnetic Resonance in Medicine / Society of Magnetic Resonance in Medicine. 1998;40(3):427–431.

104. Brodsky EK, Samsonov A a., Block WF. Characterizing and correcting gradient errors in non-Cartesian imaging: Are gradient errors Linear Time-Invariant (LTI)? Magnetic Resonance in Medicine. 2009;62(6):1466–1476.

105. Vannesjo SJ, Haeberlin M, Kasper L, Pavan M, Wilm BJ, Barmet C, Pruessmann KP. Gradient system characterization by impulse response measurements with a dynamic field camera. Magnetic resonance in medicine : official journal of the Society of Magnetic Resonance in Medicine / Society of Magnetic Resonance in Medicine. 2013;69(2):583–93.

106. Vannesjo SJ, Haeberlin M, Kasper L, Pavan M, Wilm BJ, Barmet C, Pruessmann KP. Image reconstruction using the gradient impulse response for trajectory prediction. Magnetic resonance in medicine : official journal of the Society of Magnetic Resonance in Medicine / Society of Magnetic Resonance in Medicine. 2013;69(2):583–93.

107. Addy NO, Wu HH, Nishimura DG. Simple method for MR gradient system characterization and k-space trajectory estimation. Magnetic Resonance in Medicine. 2012;68(1):120–129.

108. Johnson KO, Pipe JG. Convolution kernel design and efficient algorithm for sampling density correction. Magnetic resonance in medicine : official journal of the Society of Magnetic Resonance in Medicine / Society of Magnetic Resonance in Medicine. 2009;61(2):439–47.

109. Brent R. Algorithms for minimization without derivatives. Englewood Cliffs, New Jersey: Prentice-Hall; 1974.

110. Reeder SB, Pineda AR, Wen Z, Shimakawa A, Yu H, Brittain JH, Gold GE, Beaulieu CH, Pelc NJ. Iterative decomposition of water and fat with echo asymmetry and least-squares estimation (IDEAL): application with fast spin-echo imaging. Magnetic resonance in medicine : official journal of the Society of Magnetic Resonance in Medicine / Society of Magnetic Resonance in Medicine. 2005;54(3):636–44.

111. Goora FG, Balcom BJ. Accuracy of the Magnetic Field Gradient Waveform Monitor (MFGM) Technique and Consequent Accuracy of Pre-Equalized Gradient Waveforms. (506):1–14.

112. Weiger M, Pruessmann KP, Bracher A-K, Köhler S, Lehmann V, Wolfram U, Hennel F, Rasche V. High-resolution ZTE imaging of human teeth. NMR in biomedicine. 2012;25(10):1144–51.

113. Weiger M, Brunner DO, Dietrich BE, Müller CF, Pruessmann KP. ZTE imaging in humans. Magnetic resonance in medicine : official journal of the Society of Magnetic Resonance in Medicine / Society of Magnetic Resonance in Medicine. 2013;70(2):328–32.

114. Wiesinger F, Sacolick LI, Menini A, Kaushik SS, Ahn S, Veit-haibach P, Delso G, Shanbhag DD. Zero TE MR Bone Imaging in the Head. Magnetic Resonance in Medicine. 2015;0(October 2014):n/a-n/a.

115. Schieban K, Weiger M, Hennel F, Boss A, Pruessmann KP. ZTE imaging with enhanced flip angle using modulated excitation. Magnetic resonance in medicine : official journal of the Society of Magnetic Resonance in Medicine / Society of Magnetic Resonance in Medicine. 2014;0:1–10.

116. Yu H, Shimakawa A, McKenzie CA, Lu W, Reeder SB, Hinks RS, Brittain JH. Phase and amplitude correction for multi-echo water-fat separation with bipolar acquisitions. Journal of Magnetic Resonance Imaging. 2010;31(5):1264–1271.

117. Soliman AS, Wiens CN, Wade TP, McKenzie C a. Fat quantification using an interleaved bipolar acquisition. Magnetic Resonance in Medicine. 2015;0:n/a-n/a.

118. Lu W, Yu H, Shimakawa A, Alley M, Reeder SB, Hargreaves B a. Water-fat separation

with bipolar multiecho sequences. Magnetic resonance in medicine : official journal of the Society of Magnetic Resonance in Medicine / Society of Magnetic Resonance in Medicine. 2008;60(1):198–209.

119. Bernstein M a., Zhou XJ, Polzin J a., King KF, Ganin A, Pelc NJ, Glover GH. Concomitant gradient terms in phase contrast MR: Analysis and correction. Magnetic Resonance in Medicine. 1998;39(2):300–308.

120. King KF, Ganin A, Zhou XJ, Bernstein M a. Concomitant gradient field effects in spiral scans. Magnetic Resonance in Medicine. 1999;41(1):103–112.

121. Cheng JY, Santos JM, Pauly JM. Fast concomitant gradient field and field inhomogeneity correction for spiral cardiac imaging. Magnetic Resonance in Medicine. 2011;66(2):390–401.

122. Vannesjo SJ, Dietrich BE, Pavan M, Brunner DO, Wilm BJ, Barmet C, Pruessmann KP. Field camera measurements of gradient and shim impulse responses using frequency sweeps. Magnetic Resonance in Medicine. 2014;72(2):570–583.

123. Wurnig MC, Calcagni M, Kenkel D, Vich M, Weiger M, Andreisek G, Wehrli FW, Boss A. Characterization of trabecular bone density with ultra-short echo-time MRI at 1.5, 3.0 and 7.0 T--comparison with micro-computed tomography. NMR in biomedicine. 2014;27(10):1159–66.

124. Robson MD, Bydder GM. Clinical ultrashort echo time imaging of bone and other connective tissues. NMR in biomedicine. 2006;19(7):765–80.

125. Weiger M, Stampanoni M, Pruessmann KP. Direct depiction of bone microstructure using MRI with zero echo time. Bone. 2013;54(1):44–7.

126. Waldman a, Rees JH, Brock CS, Robson MD, Gatehouse PD, Bydder GM. MRI of the brain with ultra-short echo-time pulse sequences. Neuroradiology. 2003;45(12):887–92.

127. Du J, Ma G, Li S, Carl M, Szeverenyi NM, VandenBerg S, Corey-Bloom J, Bydder GM. Ultrashort echo time (UTE) magnetic resonance imaging of the short T2 components in white matter of the brain using a clinical 3T scanner. NeuroImage. 2014;87:32–41.

128. Kuethe DO, Caprihan A, Fukushima E, Waggoner RA. Imaging lungs using inert fluorinated gases. Magnetic Resonance in Medicine. 1998;39(1):85–88.

129. Gibiino F, Sacolick L, Menini A, Landini L, Wiesinger F. Free-breathing, zero-TE MR lung imaging. Magnetic Resonance Materials in Physics, Biology and Medicine. 2014.

130. Hövener J-B, Zwick S, Leupold J, Eisenbeiβ A-K, Scheifele C, Schellenberger F, Hennig J, Elverfeldt D V, Ludwig U. Dental MRI: imaging of soft and solid components without ionizing radiation. Journal of magnetic resonance imaging : JMRI. 2012;36(4):841–6.

131. Hafner S. Fast imaging in liquids and solids with the Back-projection Low Angle ShoT (BLAST) technique. Magnetic Resonance Imaging. 1994;12(7):1047–1051.

132. Wu Y, Ackerman JL, Chesler D a., Graham L, Wang Y, Glimcher MJ. Density of organic matrix of native mineralized bone measured by water- and fat-suppressed proton projection MRI.

Magnetic Resonance in Medicine. 2003;50(1):59–68.

133. Li C, Magland JF, Seifert AC, Wehrli FW. Correction of excitation profile in zero echo time (ZTE) imaging using quadratic phase-modulated RF pulse excitation and iterative reconstruction. IEEE Transactions on Medical Imaging. 2014;33(4):961–969.

134. Idiyatullin D, Corum C, Park J-Y, Garwood M. Fast and quiet MRI using a swept radiofrequency. Journal of magnetic resonance (San Diego, Calif. : 1997). 2006;181(2):342–9.

135. Idiyatullin D, Corum C a., Garwood M. Multi-Band-SWIFT. Journal of Magnetic Resonance. 2014;(November).

136. Zhang J, Idiyatullin D, Corum C a., Kobayashi N, Garwood M. Gradient-modulated SWIFT. Magnetic Resonance in Medicine. 2015;0(November 2014):n/a-n/a.

137. Halse M, Goodyear DJ, MacMillan B, Szomolanyi P, Matheson D, Balcom BJ. Centric scan SPRITE magnetic resonance imaging. Journal of magnetic resonance (San Diego, Calif. : 1997). 2003;165(2):219–229.

138. Rahmer J, Börnert P, Groen J, Bos C. Three-dimensional radial ultrashort echo-time imaging with T2 adapted sampling. Magnetic Resonance in Medicine. 2006;55(5):1075–1082.

139. Hennel F. Fast spin echo and fast gradient echo MRI with low acoustic noise. Journal of magnetic resonance imaging : JMRI. 2001;13(6):960–6.

140. Cho ZH, Chung ST, Chung JY, Park SH, Kim JS, Moon CH, Hong IK. A new silent magnetic resonance imaging using a rotating DC gradient. Magnetic Resonance in Medicine. 1998;39(2):317–321.

141. Hennel F, Girard F, Loenneker T. “Silent” MRI with soft gradient pulses. Magnetic resonance in medicine : official journal of the Society of Magnetic Resonance in Medicine / Society of Magnetic Resonance in Medicine. 1999;42(1):6–10.

142. Hofmann M, Steinke F, Scheel V, Charpiat G, Farquhar J, Aschoff P, Brady M, Scholkopf B, Pichler BJ. MRI-Based Attenuation Correction for PET/MRI: A Novel Approach Combining Pattern Recognition and Atlas Registration. Journal of Nuclear Medicine. 2008;49(11):1875–1883.

143. Wollenweber SD, Ambwani S, Delso G, Lonn AHR, Mullick R, Wiesinger F, Piti Z, Tari A, Novak G, Fidrich M. Evaluation of an atlas-based PET head attenuation correction using PET/CT & MR Patient Data. IEEE Transactions on Nuclear Science. 2013;60(5):3383–3390.

144. Schreibmann E, Nye J a, Schuster DM, Martin DR, Votaw J, Fox T. MR-based attenuation correction for hybrid PET-MR brain imaging systems using deformable image registration. Medical physics. 2010;37(5):2101–2109.

145. Hofmann M, Bezrukov I, Mantlik F, Aschoff P, Steinke F, Beyer T, Pichler BJ, Schölkopf B. MRI-based attenuation correction for whole-body PET/MRI: quantitative evaluation of segmentation- and atlas-based methods. Journal of nuclear medicine : official publication, Society of Nuclear Medicine. 2011;52(9):1392–9.

146. Malone IB, Ansorge RE, Williams GB, Nestor PJ, Carpenter TA, Fryer TD. Attenuation correction methods suitable for brain imaging with a PET/MRI scanner: a comparison of tissue atlas and template attenuation map approaches. Journal of nuclear medicine : official publication, Society of Nuclear Medicine. 2011;52(7):1142–9.

147. Zaidi H, Montandon M-L, Slosman DO. Magnetic resonance imaging-guided attenuation and scatter corrections in three-dimensional brain positron emission tomography. Medical physics. 2003;30(5):937–948.

148. Wagenknecht G, Kops ER, Tellmann L, Herzog H. Knowledge-based segmentation of attenuation-relevant regions of the head in T1-weighted MR images for attenuation correction in MR/PET systems. IEEE Nuclear Science Symposium Conference Record. 2009:3338–3343.

149. Wagenknecht G, Kops ER, Kaffanke J, Tellmann L, Mottaghy F, Piroth MD, Herzog H. CT-based evaluation of segmented head regions for attenuation correction in MR-PET systems. IEEE Nuclear Science Symposium Conference Record. 2010:2793–2797.

150. Wagenknecht G, Rota Kops E, Mantlik F, Fried E, Pilz T, Hautzel H, Tellmann L, Pichler BJ, Herzog H. Attenuation correction in MR-BrainPET with segmented T1-weighted MR images of the patient's head - A comparative study with CT. IEEE Nuclear Science Symposium Conference Record. 2012:2261–2266.

151. Kops ER, Wagenknecht G, Scheins J, Tellmann L, Herzog H. Attenuation correction in MR-PET scanners with segmented T1-weighted MR images. IEEE Nuclear Science Symposium Conference Record. 2009:2530–2533.

152. Hu Z, Ojha N, Renisch S, Schulz V, Torres I, Buhl A, Pal D, Muswick G, Penatzer J, Guo T, et al. MR-based attenuation correction for a whole-body sequential PET/MR system. IEEE Nuclear Science Symposium Conference Record. 2009:3508–3512.

153. Schulz V, Torres-Espallardo I, Renisch S, Hu Z, Ojha N, Börnert P, Perkuhn M, Niendorf T, Schäfer WM, Brockmann H, et al. Automatic, three-segment, MR-based attenuation correction for whole-body PET/MR data. European Journal of Nuclear Medicine and Molecular Imaging. 2011;38(1):138–152.

154. Akbarzadeh A, Ay MR, Ahmadian A, Riahi Alam N, Zaidi H. Impact of using different tissue classes on the accuracy of MR-based attenuation correction in PET-MRI. IEEE Nuclear Science Symposium Conference Record. 2012:2524–2530.

155. Keereman V, Fierens Y, Broux T, De Deene Y, Lonneux M, Vandenberghe S. MRI-based attenuation correction for PET/MRI using ultrashort echo time sequences. Journal of nuclear medicine : official publication, Society of Nuclear Medicine. 2010;51(5):812–818.

156. Berker Y, Franke J, Salomon a., Palmowski M, Donker HCW, Temur Y, Mottaghy FM, Kuhl C, Izquierdo-Garcia D, Fayad Z a., et al. MRI-Based Attenuation Correction for Hybrid PET/MRI Systems: A 4-Class Tissue Segmentation Technique Using a Combined Ultrashort-Echo-Time/Dixon MRI Sequence. Journal of Nuclear Medicine. 2012;53(5):796–804.

157. Juttukonda MR, Mersereau BG, Chen Y, Su Y, Rubin BG, Benzinger TLS, Lalush DS, An

H. MR-based attenuation correction for PET/MRI neurological studies with continuous-valued attenuation coefficients for bone through a conversion from R2* to CT-Hounsfield units. NeuroImage. 2015;112:160–168.

158. Santos Ribeiro A, Rota Kops E, Herzog H, Almeida P. Skull segmentation of UTE MR images by probabilistic neural network for attenuation correction in PET/MR. Nuclear Instruments and Methods in Physics Research Section A: Accelerators, Spectrometers, Detectors and Associated Equipment. 2013;702:114–116.

159. Coombs BD, Szumowski J, Coshow W. Two-point Dixon technique for water-fat signal decomposition with B0 inhomogeneity correction. Magnetic Resonance in Medicine. 1997;38(6):884–889.

160. Gudbjartsson H, Patz S. The rician distribution of noisy mri data. Magnetic Resonance in Medicine. 1995;34(6):910–914.

161. Griswold M a, Jakob PM, Heidemann RM, Nittka M, Jellus V, Wang J, Kiefer B, Haase A. Generalized autocalibrating partially parallel acquisitions (GRAPPA). Magnetic resonance in medicine : official journal of the Society of Magnetic Resonance in Medicine / Society of Magnetic Resonance in Medicine. 2002;47(6):1202–10.

162. Li S, Chang EY, Bae WC, Chung CB, Gao S, Bao S, Bydder GM, Hua Y, Du J. Ultrashort echo time bi-component analysis of cortical bone - A field dependence study. Magnetic Resonance in Medicine. 2014;71(3):1075–1081.

163. Juras V, Apprich S, Zbýň S, Zak L, Deligianni X, Szomolanyi P, Bieri O, Trattnig S. Quantitative MRI analysis of menisci using biexponential T2 * fitting with a variable echo time sequence. Magnetic Resonance in Medicine. 2013;1023(April):1015–1023.

164. Chang EY, Du J, Iwasaki K, Biswas R, Statum S, He Q, Bae WC, Chung CB. Single- and Bi-component T2 * Analysis of Tendon Before and During Tensile Loading , Using UTE Sequences. 2015;120:114–120.

165. Du J, Diaz E, Carl M, Bae W, Chung CB, Bydder GM. Ultrashort echo time imaging with bicomponent analysis. Magnetic Resonance in Medicine. 2012;67(3):645–649.

166. Wiens CN, Artz NS, Jang H, McMillan AB, Reeder SB. Externally calibrated parallel imaging for 3D multispectral imaging near metallic implants using broadband ultrashort echo time imaging. Magnetic Resonance in Medicine. 2016;0(February):1–7.

167. Gurney PT, Hargreaves BA, Nishimura DG. Design and analysis of a practical 3D cones trajectory. Magnetic Resonance in Medicine. 2006;55(3):575–582.

168. Epel B, Bowman MK, Mailer C, Halpern HJ. Absolute oxygen R1e imaging in vivo with pulse electron paramagnetic resonance. Magnetic Resonance in Medicine. 2014;72(2):362–368.